Asteroseismology with the Space Mission PLATO: Testing Modelling Requirements for Subgiant Stars

Miguel Tavares Clara
Mestrado de Astronomia e Astrofísica
Departamento de Física e Astronomia
2019

Orientador
Tiago L. Campante, Investigador (CAUP) e
Professor Auxiliar Convidado (FCUP)

Coorientador
Margarida S. Cunha, Investigadora (CAUP)

U.PORTO

FACULDADE DE CIÊNCIAS
UNIVERSIDADE DO PORTO

Todas as correções determinadas pelo júri, e só essas, foram efetuadas.

O Presidente do Júri,

Porto, _____/_____/_____

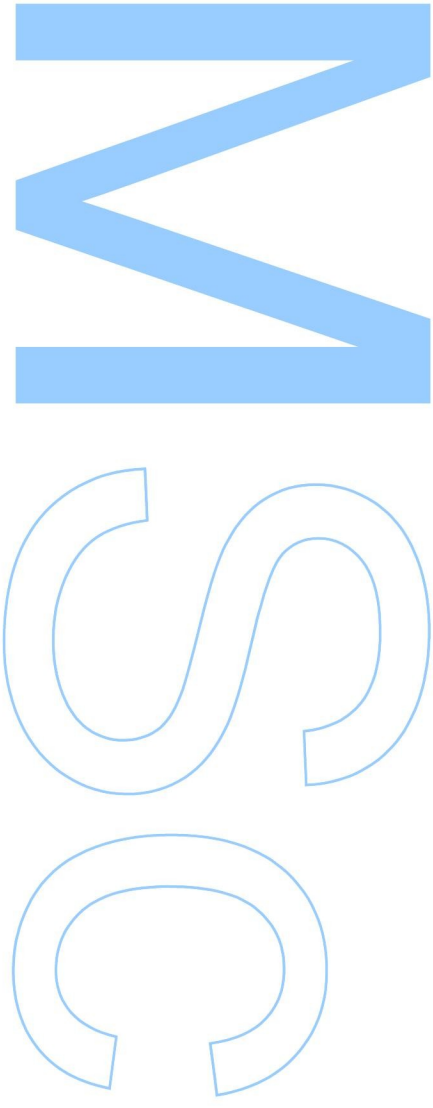

Universidade do Porto

Departamento de Física e Astronomia

Mestrado em Astronomia e Astrofísica

Asteroseismology with the Space Mission PLATO: Testing Modelling Requirements for Subgiant Stars

Miguel Tavares Clara

Supervisor: Tiago Campante

Co-supervisor: Margarida Cunha

Acknowledgments

First of all, I would like to thank both my supervisors Tiago Campante and Margarida Cunha, who guided me throughout this project with helpful arguments and discussions, for their patience, and for enlightening me even more in the area of stellar studies, especially asteroseismology. Secondly, thanks to Benard Nsamba for taking some time to help me understanding the codes we worked with, and participating in the discussions along with my supervisors. Also, a reference to Kuldeep Verma for the insightful discussion about the grid his team at the University of Aarhus built. At last but not least, a huge thanks to my family and friends who supported me during this project, especially to Nuno Moedas whose work in a similar theme and ideas helped me build this text.

Abstract

The increasing importance of asteroseismology over the last decade has improved our understanding in stellar physics, not only due to the development of new programming codes, but also due to the detailed observational data from space missions like CoRoT (by France/ESA), Kepler, TESS (both by NASA) or the upcoming PLATO (by ESA). Our goal was to test whether forward modelling based on a grid created by a team at the University of Aarhus, and on the radial modes alone, can successfully reproduce within the desired accuracies the true stellar parameters for 6 simulated stars. Further, we aimed to investigate to what extent can the density of the grid be reduced while still retrieving stellar parameters within the accuracy set by the PLATO science requirements. This study was performed the context of the PLATO mission. We took part in a *hares-and-hounds* exercise, where the *hares* were responsible for producing simulated data from theoretical stellar models for a set of 6 solar-type stars in the subgiant phase, and the *hounds* were responsible for modelling these simulated stars based on various optimization processes and the simulated data provided by the *hares*. In our case, we used the optimization code AIMS to explore the given stellar parameter space. We have verified that forward modelling is a good approach to interpret the oscillation spectra of solar-type stars, when they are on the subgiant phase, an evolutionary stage where the complex mixed modes start to appear. We have shown that fits based only on the purely acoustic $\ell = 0$ modes allow us to estimate the stellar parameters within the accuracy required by PLATO. Moreover, our results indicate that the original grid could be significantly reduced. We obtained our final grids 4 quarters of 500 evolutionary tracks each, considering, in each track, one-eighth of the original number of models uniformly distributed in time. For these subgrids, we obtained as a maximum deviations with respect to the true values: 7.24% (for mass), 2.56% (for radius), 2.77% (for density) and 25.03% (for stellar age). The new grids with a reduced number of models will allow the expansion of the parameter space (by introducing, e.g., mixing length and convective overshoot) that, in turn, will provide a better modelling and description of the studied stars.

Keywords: Astronomy & Astrophysics, Asteroseismology, AIMS optimization code, PLATO mission, Hares-and-hounds exercise, Forward modelling, Subgiant phase, Science requirements

Resumo

O recente desenvolvimento da asteroseismologia como uma importante área no estudo de estrelas deve-se não só ao desenvolvimento de novos programas úteis à sua exploração, assim como à informação obtida por missões espaciais como CoRoT (da France/ESA), Kepler, TESS (da NASA) e a esperada missão PLATO (da ESA). O objetivo deste trabalho é o de testar se a otimização de uma grelha de modelos estelares criada por uma equipa na Universidade de Aarhus, considerando apenas modos radiais, é capaz de reproduzir os parâmetros de 6 estrelas simuladas com as precisões desejadas. Além disso, também pretendemos investigar até que ponto a densidade da grelha de modelos pode ser reduzida e, ainda assim, recuperar os parâmetros das estrelas simuladas dentro dos limites de precisão requeridos. No contexto da preparação para a missão PLATO, nós participámos num exercício de *hares-and-hounds*, onde os *hares* são os responsáveis pela produção dos dados simulados, obtidos a partir dos modelos teóricos de 6 estrelas do tipo solar na fase de subgigantes, e os *hounds* correspondem aos vários processos de otimização (no nosso caso, o código AIMS) responsáveis pela modelação destas estrelas, com base nas restrições impostas pelos *hares*. Acabámos por verificar que este processo de otimização pode ser utilizado como uma boa aproximação para a interpretação do espetro de oscilação de estrelas do tipo solar em fase de subgigante, uma fase evolucionária onde os complexos modos mistos aparecem e complicam a análise de resultados. Verificamos que os ajustes feitos considerando apenas modos acústicos $\ell = 0$ permitem-nos estimar os parâmetros estelares com elevada precisão, assim como reduzir significativamente a densidade da grelha de modelos original. Cada uma das nossas 4 sub-grelhas finais é constituída por 500 modelos evolucionários, com um oitavo do número inicial de modelos distribuídos uniformemente ao longo do trilho. Para estas sub-grelhas obtivemos com o máximo desvio entre os parâmetros estimados e os verdadeiros foi de 7.24% (para a massa), 2.56% (para o raio), 2.77% (para a densidade) and 25.03% (para a idade estelar). Estas novas subgrelhas permitirão a expansão do espaço de parâmetros (ao permitir a introdução de novos parâmetros como, por exemplo, *mixing length parameter* e *convective overshoot*) que permitirão uma melhor descrição das estrelas em estudo.

Contents

List of Figures

List of Tables

Chapter 1

Introduction

Understanding stars is crucial for many fields in Astrophysics, since they are the main sources of chemical evolution in the Universe, the progenitors of objects and events of high astrophysical importance, such as supernovae, gamma ray bursts, planetary nebulae, and stellar black holes, and the main hosts of exoplanetary systems. Their physical, chemical and kinematic characteristics are able to preserve information about their birth environment and subsequent evolution until today, pertaining many relevant topics whose understanding has still many uncertainties.

Asteroseismology is a recent area in stellar astrophysics that involves using the oscillation frequencies of a star to measure its internal properties. A star is a gaseous sphere capable to oscillate in different modes when suitably excited. The frequencies of these oscillations depend on the sound speed, which in turn depends on density, temperature, gas motion and other properties of the stellar interior. The analysis of these frequencies yields important information about the chemical composition, stellar age, mixing terms, and internal rotation that cannot be obtained in any other way (Ref. [1, 2]).

In recent years, the combination of understanding stellar oscillations with the availability of a tremendous amount of exquisite space-based asteroseismic data allowed major progresses in the field, thanks to space missions like GAIA (ESA), CoRoT (Convection, Rotation and planetary Transits; France/ESA), and *Kepler* (NASA). These missions not only focus on the detection of new exoplanets, but also on the observation of stars for obtaining oscillation frequencies that help describing and cataloging them.

More recent missions are putting even more emphasis on asteroseismic observations of thousands of stars. The TESS (Transiting Exoplanet Survey Satellite; NASA) mission was launched in 2018 with the aim to find planets using the transit methods, but also to obtain new asteroseismic

data. Considering its excellent photometric precision, combined with its fine time sampling and long intervals observations, this nearly all-sky survey will enable significant developments in the asteroseismology of solar-type and red-giant stars (Ref. [3]).

Finally, the PLATO (PLAnetary Transits and Oscillation of stars) mission, foreseen to be launched in 2026, is a group of telescopes that aim to detect and characterize new exoplanets and measure stellar oscillations to study star's internal structure and how they evolve with time. It is expected to have advantages over the already successful Kepler mission, since it will observe brighter stars, and complement the study of stars with spectroscopic data from ground-based observatories (see Ref. [4, 5]).

Forward modelling techniques are among the preferred methods to simulate stars already observed or to be observed by the above mentioned missions, and estimate their global properties. The method considers an input model that defines the initial state of the system, assuming a given set of physics, and predicts its future state, at each moment over its evolution, so it can be compared with the actual observations. The best representation of the star is found following an optimization procedure that seeks to minimize the differences between model and observations, according to a criteria defined *a priori*.

There are two categories of forward modelling methods, namely the grid-based and the model-on-the-fly. In the grid-based method, the optimization code uses a pre-calculated grid to estimate the required observables to each one of the profiles of the grid. Then it compares the model observables with the observations, calculating a χ^2 value that classifies how good the model is, and compares it with the χ^2 of other models, only choosing the best ones. On a model on-the-fly approach, the models are, instead, generated inside the optimization code in a step wise fashion. A χ^2 value is assigned to each profile, which will determine whether to maintain or eliminate the model. This way, one ends up with a grid built only with the models that are more probable to provide useful information.

The main goal of this thesis is to contribute to the development of the PLATO pipeline, by carrying out a specific task within an ongoing exercise proposed by one of the PLATO's science management (PSM) working groups. The task, which will be described latter, is related to forward modelling. For that work, the first method will be preferred. Despite their size, the grids we use can be applied to different stars within an acceptable range of parameters. Although an on-the-fly approach is able to mitigate the size of a grid, calculating the goodness of fit of the models while generating them, the set of models generated in this way ends up being of little use when considering stars with different characteristics from the one being modelled, requiring a new set of

models to be generated each time. This makes this method computationally more expensive and, thus, less appropriate for a pipeline of an instrument observing a vast number of stars.

To compute the grid of stellar models, we will use the stellar evolution code MESA (Modules for Experiments in Stellar Astrophysics). The pulsation code GYRE will then be used to compute the theoretical oscillation frequencies for each model in the grid. Finally, for comparison between models and observations, we will use the optimization procedure AIMS (Asteroseismic Inference on a Massive Scale), a Python written code that calculates credible intervals and errors for stellar parameters in a Bayesian way. For that, it requires a set of constraints to limit the results of the optimization process, a list of seismic frequencies (with the associated radial orders and mode degrees), and some classical constraints like L, $T_{\rm eff}$ and $[Fe/H]$, that can be obtained from observations.

Thus, the first goal of this thesis was to understand how some important codes (like MESA, GYRE and AIMS) work, and their importance in the context of the determination of the stellar parameters. The basic concepts of stellar evolution and of the description of the MESA evolution code are the themes of Chapter 2. Chapter 3 focus on the theory behind stellar oscillations, and on the GYRE pulsation code that allows the determination of their properties (in particular, the frequencies). Chapter 4 focus on the topics of data statistics that are important to understand the methods behind the AIMS optimization code. Then, we will focus on the *hares-and-hounds* exercise that is being carried on in the context of the preparation for the ESA mission PLATO by teams from a number of different universities across the world. In this exercise, we will aim first to test whether forward modelling based on a pre-computed grid and on the radial modes alone is successful in reproducing, within the desired accuracies, the true stellar parameters for each of the hares (i.e., the simulated stars). Further, we will investigate to what extent can the density of the grid be reduced while still retrieving stellar parameters within the accuracy set by the PLATO science requirements. The description of the exercise, the methods used and a discussion of the results are presented in Chapter 5. Chapter 6 ends the thesis presenting the conclusions of our work.

Chapter 2

Stellar Evolution and Modelling

The ultimate fate of a star depends mostly of its initial mass, chemical composition and possible interactions with the surrounding medium, properties that are related to the time and place a star was born. With rare exceptions, most stars appear as a point source of radiation from which the observer can deduce a luminosity L and a surface temperature $T_{\rm eff}$. These are two of the observational properties that characterize a star over the time and are closely related, being usually illustrated through a two-dimensional plot named a Hertzsprung-Russel (HR) diagram. The latter depicts stellar evolution using the surface luminosity and the effective temperature throughout the star's lifetime. The HR diagram is of great practical and historical significance in astronomy since it provides a vital link between theoretical calculations of stellar evolution and observations.

A common solar-type star can go through various evolutionary phases: the pre-main sequence (PMS), the main sequence (MS), the subgiant phase (SG), the red giant branch (RGB), the horizontal branch and asymptotic giant branch phases (AGB) and its stellar remnants (post-AGB phase, planetary nebulae, white dwarf and black dwarf phases). Its evolution can take from some billions of years up to periods longer than the actual age of the Universe. Fig. 2.1 depicts the evolutionary path of the HR diagram for the case of the Sun.

The next sections are intended to give an overall description of the main stages of stellar evolution for the different types of stars in the Universe. Sections 2.1 to 2.3 will introduce the necessary considerations to understand stellar evolution in general. Then, we will focus on the evolutionary stages that are central for this thesis, namely the main sequence and the subgiant phases of solar-type stars.

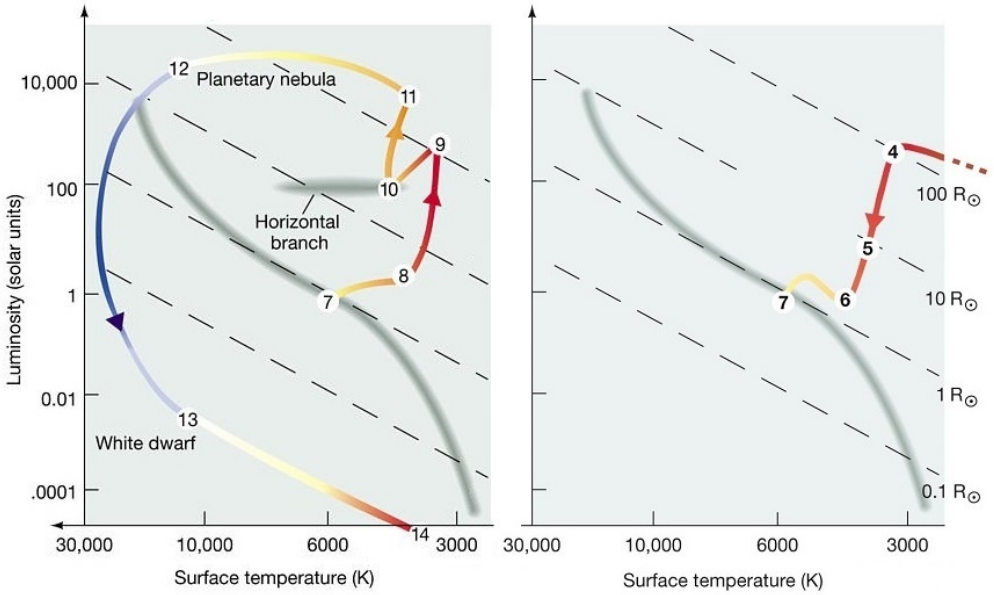

Figure 2.1: HR diagram depicting the evolution of a solar-type star. The pre-main sequence is depicted from points 1-7, the main-sequence and subgiant phases through points 7-8, the RGB branch in points 8-10, the horizontal branch and AGB phase in points 10-11, and the stellar remnants (post-AGB phase, planetary nebulae, white dwarf and black dwarf phases) through points 11-14 [adapted from *pages.uoregon.edu*].

2.1 Protostars and Pre-Main Sequence

Star formation begins when dense core regions of molecular clouds at very low temperatures (consisting of about 70% hydrogen, 28% helium and trace amounts of heavier elements) start accreting mass, losing the hydrostatic equilibrium between gravitational and pressure forces. This perturbation corresponds to a free-fall dynamical process that can be characterize through a dynamical timescale, ie the time it would take for a body to collapse under its own gravitational attraction if no other forces existed to oppose the collapse,

$$\tau_{\rm dyn} \simeq \sqrt{\frac{2R^3}{GM}} \simeq \sqrt{\frac{1}{G\rho}} \tag{2.1}$$

where ρ is the mean density of the star. As the gas collapses towards the center, the hydrostatic equilibrium is restored and a new low-mass protostar emerges, usually surrounded by an orbiting protoplanetary disk.

A star in this phase is fully convective, has a low temperature, a large radius and a high luminosity. As the collapse continues, an increasing amount of gas impacts the disk (due to angular momentum conservation), liberating energy due to the shocks on the stellar surface and on the surrounding disk. Unlike more evolved pre-main sequence stars, protostars are not detectable in optical wavelengths, not appearing on the HR diagram.

Once the accretion process is complete, the protostar collapses again until hydrostatic equilibrium is restored, thus giving birth to a pre-main sequence star. At this point, the star has acquired its total mass, but has not started the nuclear fusion of hydrogen yet. For that, it needs to further contract in order to increase its internal temperature, and allow the beginning of the hydrogen burning, moment that is defined as the Zero Age of the Main Sequence (ZAMS) (point 7 in Fig.2.1).

On the HR diagram, a pre-main sequence star starts by moving down alongside the Hayashi tracks (points 4-6 in Fig.2.1), with the star producing energy due to contraction, and transporting it through convective motions. If the internal variables change so a completely convective star gains a radiative interior before the star reaches the ZAMS (which usually happens for stars with $M > 0.5$ $M_\odot$), then the star will move horizontally to the left alongside the Henyey track (points 6-7 in Fig.2.1), until it finally halts at the main sequence.

However, more massive stars (with $M > 5$ $M_\odot$) do not present a pre-main sequence stage because their contraction as protostars is too fast. By the time they become visible, the hydrogen in their core is already fusing, placing the star already in the main sequence.

2.2 Main Sequence of Solar-Type Stars

2.2.1 Observational Properties

Upon reaching the main sequence, the temperature on the core turns on the energy generation process by burning hydrogen into helium which, in turn, increases the luminosity and the surface temperature as the star ages. This represents the primary nuclear burning stage of a star's lifetime.

During this time, most of the stars tend to stabilize alongside a characteristic curve in the HR diagram - the main sequence region defined in Fig. 2.2. The position and time spent in the main sequence is mainly controlled by the stellar mass, while, in comparison, the chemical composition and mixing processes play a secondary role[1]. As a whole, these parameters control the star's energy production and the heat transfer to the surface, that will be described in the following sections.

From the HR diagrams, it becomes clear the strong correlation between luminosity and effective temperature. In fact, if we treat a star as a black body, we can relate these parameters through the so called Stefan-Boltzmann law,

$$L = 4\pi R^2 \sigma T_{\text{eff}}^4 \tag{2.2}$$

[1] As important as it is to understand how these three parameters (stellar mass M, chemical composition X, Y, Z and mixing parameter α_{MLT}) influence the evolution of a star, they will be explored when modelling stellar evolution with the MESA code (see Section 2.4)

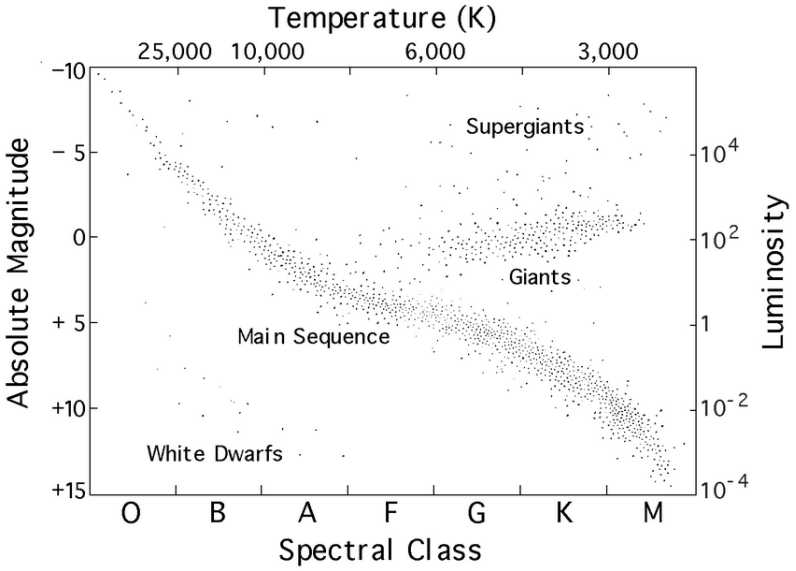

Figure 2.2: A schematic HR diagram providing a snapshot of the luminosity and surface temperature of stars at different stages of evolution. Most of the observed stars are grouped along a band called the main sequence - these are hydrogen burning stars like the Sun. As a star evolves, the contraction of the central core is accompanied by an expansion of its outer layers to form luminous stars with low surface temperature, e.g. red giants. The endpoint in the evolution of a star with a mass comparable to the Sun is a compact object supported by degenerate electrons, a white dwarf. The evolution of a more massive star can lead to the formation of a neutron star or a black hole (Ref. [7]).

where $\sigma = 5.6704 \times 10^{-5}\text{erg.cm}^{-2}\text{s}^{-1}\text{K}^{-4}$ is the Stefan-Boltzmann constant. From here, we can conclude that the radius grows from the bottom left region (dominated by white dwarfs) to the top right area (dominated by giants) of the HR diagram.

From homology relations, we can depict a group of relations for mass-luminosity and mass-radius (as shown in Fig. 2.3). The mass-luminosity relation for a star with a given mass and chemical composition can be deduced from its position in the main sequence, being of the order of

$$\left(\frac{L}{L_\odot}\right) \simeq \left(\frac{M}{M_\odot}\right)^\beta \tag{2.3}$$

with the value of β varying between 3.0 and 3.5, according to how efficiently energy transport is. This implies that stellar masses will tend to range from about 0.1 $M_\odot$ at the bottom right of the main-sequence (since smaller stars never get the central temperature necessary to start the fusion of hydrogen), to about 50 $M_\odot$ at the top left (as larger stars are easily disrupted by internal and gravitational forces).

Finally, the mass-radius relation is shown to be close to linear (in Fig. 2.3), reflecting a rough proportionality between these parameters and the star's inner temperature, since the relation is mostly dependent on the energy generation process.

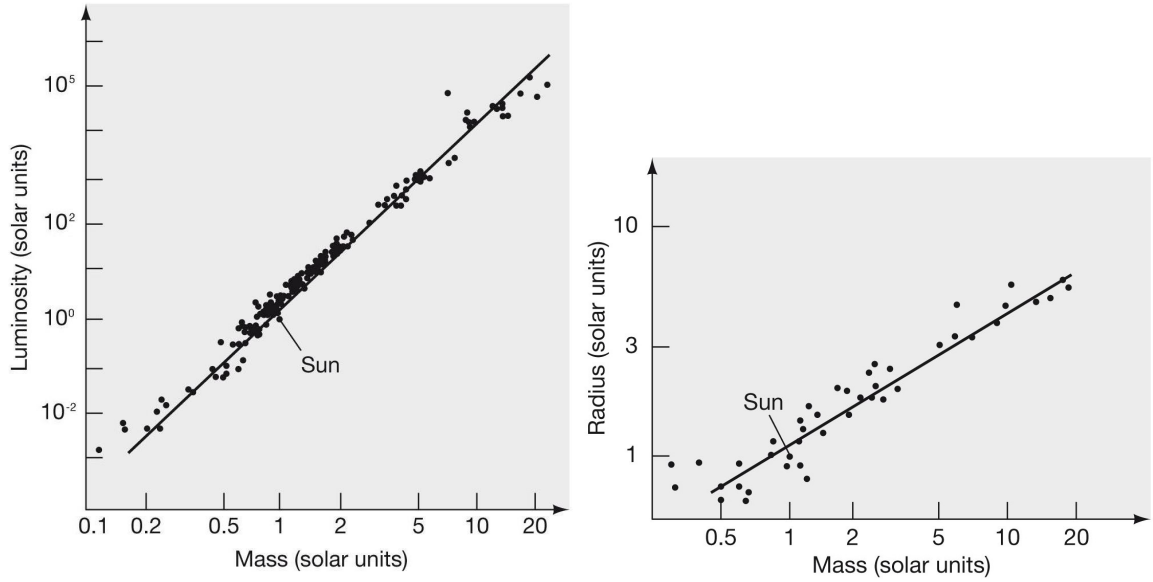

Figure 2.3: Mass-luminosity (on the left) and mass-radius (on the right) relations for stars in the main sequence [*pages.uoregon.edu*].

2.2.2 Stellar Structure

Most of the observed stars are currently in their long-lasting phase of evolution. Since appreciable changes during this stage are too slow to be observed, they can be described by the four basic differential equations of stellar structure that have dubbed the macrophysics in modern theory of stellar studies

$$\frac{\partial r}{\partial m} = \frac{1}{4\pi r^2 \rho} \tag{2.4}$$

$$\frac{\partial P}{\partial m} = -\frac{Gm}{4\pi r^2} \tag{2.5}$$

$$\frac{\partial L}{\partial m} = \epsilon - \epsilon_v + \epsilon_g \tag{2.6}$$

$$\frac{\partial T}{\partial m} = -\frac{GmT}{4\pi r^4 P}\nabla \quad \text{where} \quad \nabla = \left(\frac{\partial \ln T}{\partial \ln P}\right) \tag{2.7}$$

where r is the distance from the center of the star, and m is the mass contained in r, P is the pressure, T is the temperature, ρ is the density, and L_r is the luminosity at the corresponding position r. The ϵ terms correspond to various forms of energy rates.

These equations correspond to the mass conservation (Eq. 2.4), the hydrostatic equilibrium (Eq. 2.5), the energy conservation (Eq. 2.6) and the energy transport (Eq. 2.7) equations. Their solutions tend to evolve with time, as a consequence of the nuclear reactions taking place and the resulting changes in the chemical composition brought about by them. In order to comprehend these solutions, we should understand what happens in the central core of the star, as it will be next described.

2.2.3 Energy Generation

Main-sequence stars have a core region where energy is generated by nuclear fusion while keeping hydrostatic equilibrium. These stars can employ two types of hydrogen fusion processes (Fig.2.4): a proton-proton chain (pp chain) which directly fuses hydrogen together in a series of stages to produce helium, and a CNO cycle for stars in the upper main sequence with high nuclear temperatures, that uses carbon, nitrogen and oxygen isotopes as catalysts for the reactions, being both destroyed and produced during the cycle. Both processes take place simultaneously inside the star but with different efficiencies depending on the inner conditions.

p-p chain

pp I	pp II	pp III
$^{1}H + {}^{1}H \rightarrow {}^{2}D + e^{+} + \nu_e$	$^{3}He + {}^{4}He \rightarrow {}^{7}Be + \gamma$	$^{3}He + {}^{4}He \rightarrow {}^{7}Be + \gamma$
$^{2}D + {}^{1}H \rightarrow {}^{3}He + \gamma$	$^{7}Be + e^{-} \rightarrow {}^{7}Li + \nu_e$	$^{7}Be + {}^{1}H \rightarrow {}^{8}B + \gamma$
$^{3}He + {}^{3}He \rightarrow {}^{4}He + {}^{1}H + {}^{1}H$	$^{7}Li + {}^{1}H \rightarrow {}^{4}He + {}^{4}He$	$^{8}B \rightarrow {}^{8}Be + e^{+} + \nu_e$
		$^{8}Be \rightarrow {}^{4}He + {}^{4}He$

CNO cycle

CN cycle	NO cycle
$^{12}C + {}^{1}H \rightarrow {}^{13}N + \gamma$	$^{15}N + {}^{1}H \rightarrow {}^{16}O + \gamma$
$^{13}N \rightarrow {}^{13}C + e^{+} + \nu_e$	$^{16}O + {}^{1}H \rightarrow {}^{17}F + \gamma$
$^{13}C + {}^{1}H \rightarrow {}^{14}N + \gamma$	$^{17}F \rightarrow {}^{17}O + e^{+} + \nu_e$
$^{14}N + {}^{1}H \rightarrow {}^{15}O + \gamma$	$^{17}O + {}^{1}H \rightarrow {}^{14}N + {}^{4}He$
$^{15}O \rightarrow {}^{15}N + e^{+} + \nu_e$	
$^{15}N + {}^{1}H \rightarrow {}^{12}C + {}^{4}He$	

Figure 2.4: Reaction networks involved in the pp chain and the CNO cycle [Ref. [6]].

The nuclear energy generation rate of these channels, ϵ, has different temperature sensitivities, meaning that the conditions in the stellar interior will define the efficiency with each one of the reaction networks will operate. The pp chain has an average relation of $\epsilon_{pp} \propto T^4$ at $T \simeq 15 \times 10^6$ K, while the CNO cycle has a higher value of $\epsilon_{CNO} \propto T^{18}$ at $T \simeq 20 \times 10^6$ K. As an example, $T_c \simeq 15 \times 10^6$ K at the center of the Sun and more than 90% of the energy comes from the pp chain, while for stars with masses around 1.5 $M_\odot$ (with associated core temperatures of 18×10^6 K), both pp chain and CNO cycle become equally efficient, with each one generating half of the stellar luminosity. An important consequence of the temperature sensitivities is that, if the H-burning process is dominated by the CNO cycle, it will be confined towards the very central regions of the star, resulting in a larger energy flux arising from the innermost regions that favors the presence of a convective core.

For a star in equilibrium, we can estimate how long a star can shine based on its fuel consumption rate by calculating the nuclear timescale as

$$\tau_{\rm nuc} \simeq \frac{\text{total mass of fuel available}}{\text{rate of fuel consumption}} \times \text{fraction of star over which fuel is burned} \simeq \epsilon q \frac{Mc^2}{L} \quad (2.8)$$

where c is the speed of light, q is the fraction of the total stellar mass involved in the nuclear burning, and ϵ is the amount of mass that is converted into energy as a result of the nuclear reaction processes. Note that this equation only considers the hydrogen burning, with the real value of $\tau_{\rm nuc}$ being higher.

Thus, we can see that, although massive stars have more fuel to burn, they also radiate a proportionately greater amount of energy as required by the equation of state. This way, even with the most massive stars remaining on the main sequence for only a few million years, stars smaller than 0.5 $M_\odot$ may last for over a trillion years.

2.2.4 Heat Transfer Processes

Under normal circumstances, there is a steady flow of energy from the deep interior, where the nuclear reactions take place, to the outermost layers of the star, where energy is radiated into the interstellar medium. Depending on the thermodynamic properties of matter, the energy can be transported by radiative processes or convection motions.

Stellar radiative regions tend to be stable areas with little mix of the plasma. There, the matter is so dense that photons can only travel a short distance before being absorbed or scattered by other particles, gradually shifting to longer wavelengths as they do so. Because of this, photons can travel years in these regions before ascend to the surface. When essentially all energy is transported outwards by photons (as required by the condition of radiative equilibrium), the temperature gradient in Eq. 2.7 takes the form

$$\nabla_{\rm rad} = \left(\frac{\partial \log T}{\partial \log P}\right)_{\rm rad} = \frac{3}{16\pi acG}\frac{\kappa LP}{mT^4} \quad (2.9)$$

where κ is the mean opacity of the environment.

In a near isotropic environment, opacity corresponds to the ability of the environment to absorb and scatter radiation, being described as a dependency of the chemical composition and degree of ionization of the environment k_0, the temperature T, and the mean density ρ, through

$$k = k_0(X, Z)\rho^\alpha T^{-\beta}, \quad (2.10)$$

where α and β are constants that depend on the main process of photon absorption and scattering acting during the main sequence. For solar-type stars, the opacity is dominated by absorption

processes highly dependent on ρ and T. However, for more massive stars, with high temperatures and low densities, the opacity is dominated by electron scattering, and is shown to be mostly independent of ρ and T. Note that chemical composition, and Z in particular, have a large effect on κ, which provides the most important influence of composition on stellar structure.

In contrast, convective zones present intense plasma flows that form circular convection currents with hotter materials rising and cooler flows descending. These motions can be explained as a gas element that, by suffering a slightly temperature fluctuation (associated with a variation in density) rises inside the star. If the temperature gradient on the region is too steep (ie it rapidly changes with radius), or if the gas has a very high heat capacity (ie the temperature changes relatively slow as the gas expands), then the rising gas element will remain warm and less dense than its new surroundings. Thus, its buoyancy will allow it to continue to rise, forming a convective current.

This form of energy transport is much more efficient than radiation, since there is a limit to the flux that can be transported through a specific medium by radiation. The Schwarzschild criterion states that convection is activated once the radiative temperature gradient exceeds the adiabatic temperature gradient

$$\nabla_{\rm rad} < \nabla_{\rm ad} \tag{2.11}$$

where $\nabla_{\rm ad}$ is the temperature gradient introduced in Eq. 2.7 when the displacement of the bubble takes place adiabatically. The more complex Ledoux criterion states that a layer remains stable if

$$\nabla_{\rm rad} < \nabla_{\rm ad} + \frac{\varphi}{\delta}\nabla_\mu \tag{2.12}$$

where $\varphi = \left(\frac{\partial \ln\rho}{\partial \ln\mu}\right)_{P,T}$, $\delta = -\left(\frac{\partial \ln\rho}{\partial \ln T}\right)_{P,\mu}$ and $\nabla_\mu = \left(\frac{\partial \ln\mu}{\partial \ln P}\right)$, additionally taking into account the spatial variation of the mean molecular weight μ.[2]

In a radiative (dynamically stable) layer, a displaced element is pushed back by buoyancy forces, which imprints the necessary momentum to create convective circular flows. Such adiabatic oscillations of the plasma are characterized by the Brunt-Väisäla frequency

$$N^2 = \frac{g\delta}{H_P}\left(\nabla_{\rm ad} - \nabla + \frac{\varphi}{\delta}\nabla_\mu\right) \tag{2.14}$$

where H_P is the pressure scale height. For the oscillation to happen, $N^2 > 0$ which is the case for a

[2] μ is the mean molecular weight per gas particle that depends both on the chemical composition and the ionization degree of the gas. For both a neutral and a ionized gas, we have that

$$\mu_{\rm n} \simeq \frac{4}{4X+Y} \quad \text{and} \quad \mu_{\rm ion} \simeq \frac{4}{6X+Y+2} \tag{2.13}$$

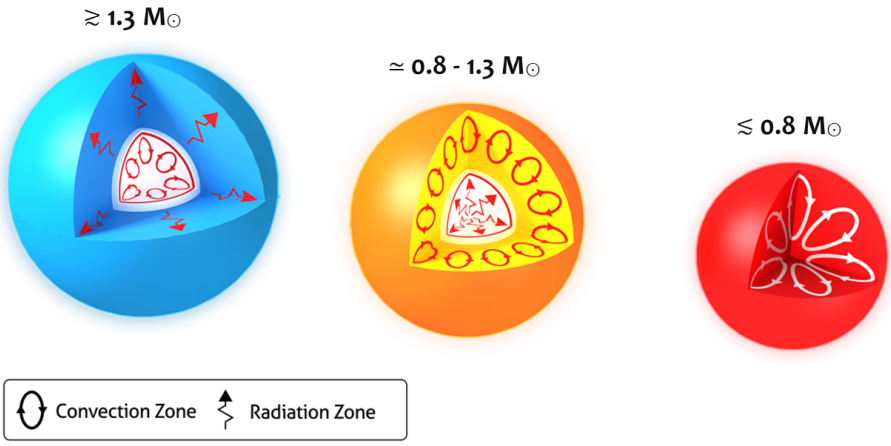

Figure 2.5: The different energy transport mechanisms that work on high-mass, mid-mass and low-mass stars [adapted from *sun.org*, released under CC-BY-SA 3.0].

convective stable region. Once a region is found to be convective, the temperature gradient of that zone (Eq. 2.7) can be defined by using the mixing-length parameter for convection $\alpha_{\rm MLT} = \ell/H_P$, where ℓ is the average distance a gas element will transverse before dissolving into the medium.

For the most massive stars (with $M \gtrsim 1.3$ M$_\odot$[3]), the generation of energy through the CNO cycle is highly concentrated in the core, producing a high temperature gradient in the innermost regions that results in convection. This allows the removal of helium ash from the H-burning region, so that even more hydrogen can be consumed during the main-sequence. The outer regions of the star transport energy by radiation.

Intermediate-mass stars similar to the Sun (with masses between 0.8 and 1.3 M$_\odot$) transport energy primarily through radiation around the core, and present a convection envelope that mixes the layers near the surface. The presence of a convective envelope has important consequences for the pulsation properties of the stars, as it stochastically produces excitation modes.

Low mass stars are fully convective, which means that the helium produced in the core can be distributed across the whole star, producing a relatively uniform composition and giving it a longer lifespan. A schematic of these stars can be found in Fig. 2.5.

Subsections 2.2.3 and 2.2.4 described the main processes that characterize the main sequence of any star, being specially important to explain the variations in chemical composition. In stellar evolution, X, Y, Z define the mass fractions of hydrogen, helium and heavier elements. In the core, energy generation is responsible for transforming hydrogen in helium during the main sequence, while convective motions mix the chemical components of the internal layers. This results in a characteristic chemical evolution through out a star's lifetime (that will be explored later).

[3]This value may vary with the initial chemical composition, that is $M \simeq 1.3$M$_\odot$ at solar metallicity (Ref. [6]).

However, other processes can also influence the internal layers. Convective efficiency (ie α_{MLT} under the mixing length formulation) is an important parameter that will be discussed in the following sections, but other physical processes such as cases of atomic diffusion, rotational mixing, the influence of magnetic fields, stellar winds, etc, should at least be referenced.

2.3 Stellar Advanced Stages

As it happens with the internal structure and internal processes that influence the main-sequence (as seen in previous subsections), the pos-main sequence stages of any star are also dependent on the stellar mass value. As the hydrogen burning ceases to be a central process, the star starts to move away from the stable main-sequence line it has been for billions of years, entering a period of intense changes that will culminate in its ultimate fate.

2.3.1 Subgiant and Giant Phases

As the H-burning ceases to be the central process and becomes a shell-burning process outside the He-rich core, the stellar envelope expands, cooling down the star that starts moving to the right in the HR diagram, entering the subgiant phase.

When nuclear reactions become inefficient, the physical conditions in the stellar interior evolve so the star gradually contracting becomes responsible for the energy production. The time it takes to radiate away its total kinetic energy content at its current luminosity rate is defined as the Kelvin-Helmholtz timescale, given by

$$\tau_{\mathrm{KH}} \simeq \frac{\text{total kinetic energy}}{\text{rate of energy loss}} \simeq \frac{GM^2}{2RL} \tag{2.15}$$

For stars with $M > 3.0\ \mathrm{M}_{\odot}$, the core contracts, since it cannot counteract the pressure exerted by the outer layers, and a convective envelope starts to develop due to the cooling down of the outer layers, marking the beginning of the red giant phase. From here onwards, the star evolves at a roughly constant temperature, shell-burning hydrogen and increasing its luminosity and radius, while further contracting the core. Eventually, the central temperature will be high enough to ignite the helium fusion in the center, marking the end of the RG phase. This occurs under non-degenerate conditions, as the central density is low enough to prevent electron degeneracy[4]. For

[4]The Pauli exclusion principle (from quantum mechanics) does not allow two identical spin particles (like electrons) to occupy the same quantum state simultaneously. This results in an emergent pressure when matter is compressed into small volumes - the electron degeneracy pressure. This limits, the transition between a classical gas and a state of strong degeneracy, occurs when $n_e \gtrsim \frac{2(2\pi m_e kT)^{2/3}}{h^3}$, where h is the Planck constant.

increasing stellar masses, the time needed to reach He-burning temperatures is very short and the RG might even disappear.

For stars with $M < 3.0$ $M_\odot$, the gas in the He-rich core is electron-degenerate, providing enough pressure to support the envelope above it and, at the same time, grow from the production of helium in the H-burning shell. During the subgiant phase, the cooling down of the outer layers results in an inward penetration of the convective envelope which drags partially processed nuclear material to the surface - the *first dredge-up*. This phenomena can be witnessed through the change in CNO abundances due to mixing of former processed core material dredged-up to the surface.

After this process, the convective envelope begins to retreat as the star ascends through the red giant branch (RGB). During this phase, stars lose some of their mass through stellar winds due to their huge envelopes. Although helium ignition occurs quietly for massive stars, the case for stars below ~ 3.0 $M_\odot$ is somewhat different. In the late stages of the RGB, stars lose large amounts of energy in the form of neutrinos, specially in the most dense regions. This provokes an inversion of the thermal profile of the He-core, with the hottest place being located off-center, within the He-rich core. When temperatures are high enough to start He-burning, the ignition takes place off-center in a sort of thermonuclear runaway defined as an core helium flash, a phenomena related with a property of the electron degenerate gas, the decoupling of the temperature dependence from the $P - \rho$ relation. During this phase, large amounts of energy produced by the ignition are used to lift up the degeneracy in the core, decreasing its luminosity and inducing secondary flashes close to the center (that produce the loops that can be observed in HR diagrams).

The star is then quiescently burning helium in a convective core surrounded by a H-burning shell, when it enters the horizontal branch phase, the second longest evolutionary phase in a life of a star.

2.3.2 Stellar Remnants

As the nuclear helium is exhausted, the next step will depend again on the stellar mass. Stars with $M \lesssim 0.8$ $M_\odot$ are not even able to start helium burning, moving directly off the RGB and becoming helium white dwarfs. The fate of more massive stars will depend on whether they meet the Chandrasekhar condition or not. This limit corresponds to the mass above which electron degeneracy pressure in the star's core becomes inefficient to balance its own gravitational attraction, establishing the maximum mass for a stable white dwarf around 1.45 $M_\odot$ (although it can get up to 8.0 $M_\odot$).

Once helium is exhausted in the core, stars with initial masses < 8.0 $M_{\odot}$ shine by helium and hydrogen shell burning. Then, they ascend through the asymptotic giant branch (AGB), a phase where extinction and re-ignition of helium leads to the occurrence of thermal pulses. Once hydrogen is largely exhausted in the burning shell, the remaining envelope is rapidly lost and shines due to ionization by the bare core of the star as a planetary nebula. This exposes the core - a white dwarf - that evolves down the white dwarf cooling curve over the course of billions of years.

Naturally, stars with core masses higher than the Chandrasekhar limit will ignite carbon under non-degenerate conditions, and keep burning even heavier elements while producing shells in a so-called onion skin model. At last, the core consisting mostly of ^{56}Fe will become dynamically unstable, collapsing and resulting in a supernova explosion that exposes one of a set of strange objects - a neutron star or a black hole.

2.4 MESA Evolution Code

MESA (Modules for Experiments in Stellar Astrophysics) is a one-dimensional stellar evolution code design to simulate stellar evolutionary tracks within a wide range of parameters (such as mass, chemical composition and mixing length parameter), that can also be applied to the study of other stellar physics problems (Ref. [8]). The code allows a full resolution of both structure and composition equations at the same time by defining a group of step and stop conditions that guide the simulation. It also features special modules that provide different aspects of the numerics and physics required to construct computational models in astrophysics, including several numerical methods important for linear algebra routines for matrix manipulation, one- and two-dimensional interpolation, and a variety of solvers for systems of ordinary differential equations (ODEs)[5].

The microphysics modules provide the physical properties of stellar matter, with each module focusing on a different aspect: mathematical constants, physical and astronomical data, equations of state (addressed in subsection 2.3.2), opacities, thermonuclear and weak reactions, and nuclear reaction networks. Meanwhile, the macrophysics modules are focused on the mixing length theory of convection (implemented by the `mlt` module inspired by Ref. [9], that calculates diffusion coefficients by treating convective mixing elements as a diffusive process), convective overshoot mixing (treated as a time dependent diffusive process with a diffusion coefficient determined via a parametric model that accounts for hydrodynamical mixing instabilities at the convective boundaries), atmosphere boundary conditions (that use the `atm` module to determine surface parameters by assuming a plane parallel limit), atomic diffusion (by solving Burger's equations using the method and diffusion coefficients in Ref. [10]), and transport of material (computed through a semi-implicit, finite difference scheme described by Ref. [11]).

The MESA code starts by reading the inputs from two inlists (one that defines the type of evolutionary calculation to be performed, the input model to be used, the source of EOS and opacity data, the chemical composition and nuclear network, among others, and other specifying the controls and options to be applied during the evolution), and initializing the physics modules to create a nuclear reaction network and access the EOS and opacity data. As the starting model is loaded and the evolution loop is entered, the procedure encores through four basic steps.

First, it prepares to take a new timestep by remeshing the model if necessary. The timestep selection is crucial, since it should be small enough to allow convergence in few interactions,

[5]Solvers for ODEs include a Newton-Raphson solver for multidimensional nonlinear root finding, linear implicit Runge-Kutta methods, with second-, third-, and fourth-order versions, and the two implicit extrapolation integrators, that can be either midpoint or Euler processes.

but large enough to allow efficient evolution. Second, it adjusts the model to reflect mass loss by winds or mass gain from accretion, adjusts the abundances for element diffusion, determines the convective diffusion coefficients, and solves for the new structure and composition using the Newton-Raphson solver. Third, it estimates the next timestep. Fourth, the code generates a list of output files that contain the required inputs for the stellar pulsation code.

Knowing how the MESA code is structured and how it works, we proceed with the analysis of the results obtained when constructing an evolutionary track.

2.4.1 Evolution of a Solar-Mass Star in the HR Diagram

From the theoretical considerations presented in Sections 2.1 to 2.3, it is clear that the stellar mass M and the chemical composition are the parameters that play the primary role in the processes that affect the lifetime of a star, being the main inputs required by our code to simulate the wanted evolutionary tracks. Other descriptive values of the macroscopic physics adopted, such as the mixing length parameter $\alpha_{\rm MLT}$ and the convective overshoot parameter $\alpha_{\rm ov}$, microscopic physics like atomic diffusion, and possible additional physical processes, such as mass losses and rotation, can also be considered in the code to describe the stellar structure and the processes that occur in-depth.

After running the simulations, MESA creates two files for each profile calculated named .data and .FGONG of which we will use essentially the latter. Each .FGONG file consists of a header (providing descriptive information and key dimensions of data vectors), a set of 15 global parameters (including stellar mass M_*, radius R_*, luminosity L_*, metallicity Z, initial hydrogen abundance X_0, mixing length parameter $\alpha_{\rm MLT}$, stellar age t in yrs, etc) and a set of 40 local variables provided at each mesh point (providing for each radial position value r the local mass in the form $\ln\left(\frac{m}{M}\right)$ (where m/M is the fraction stellar mass contained inside the radius r), and the local values of temperature T, pressure P, density ρ, hydrogen abundance X, luminosity $L_{\rm r}$, opacity κ, adiabatic gradient $\nabla_{\rm ad}$, etc).

The results for our first simulation using the MESA code are represented in Figs. 2.6 to 2.9. Fig. 2.6 shows the evolutionary track of a solar-type star in the HR diagram produced by setting $M = 1.0$ M$_\odot$, $Z = 0.018$ and $\alpha_{\rm MLT} = 1.8$ from the pre-main sequence to the luminosity bump on the Red Giant Branch (RGB). The remaining chemical composition parameters were determined through Eqs. 2.18 and 2.19 (to be discussed in Section 2.4.3), and found to be $X_0 = 0.7084$ and $Y_0 = 0.2736$. Fig. 2.8 displays the evolution of the stellar radius as a function of the stellar age, clearly showing its growth, particularly in the later stages of evolution. Fig. 2.9 illustrates the re-

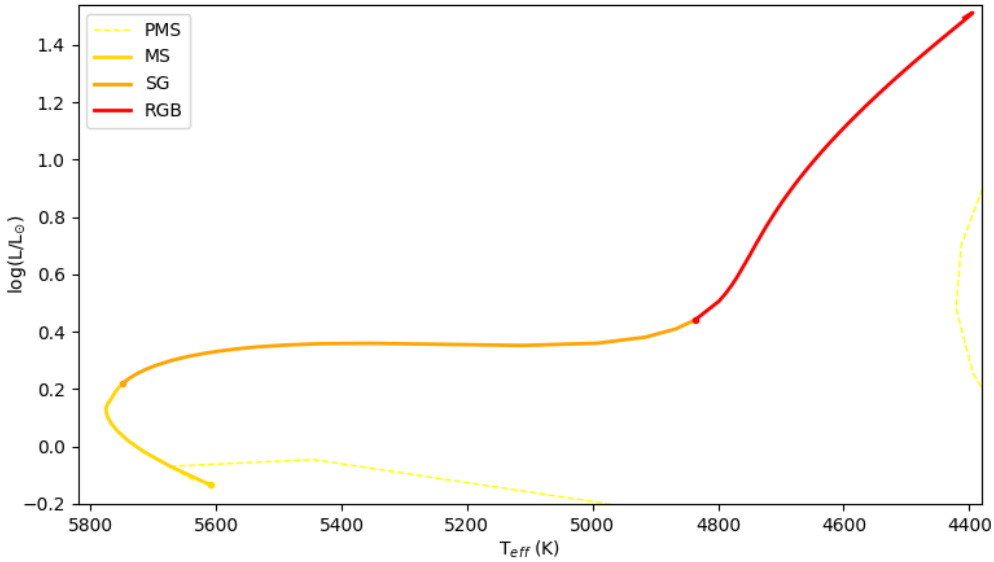

Figure 2.6: HR diagram illustrating the evolutionary track of a solar-like star with $M = 1$ M$_\odot$, $Z_0 = 0.018$, $Y_0 = 0.2736$, $X_0 = 0.7084$ and $\alpha_{\rm MLT} = 1.8$. The HR diagram presents the different evolutionary stages of a stellar's lifetime, running from the ZAMS to the luminosity bump on the RGB. Each stage was obtained considering certain step and stop conditions defined separately for the PMS, the MS, the SG, and the RGB. Histograms depicting the step conditions used in the MS and in the SG are represented in Fig. 2.7.

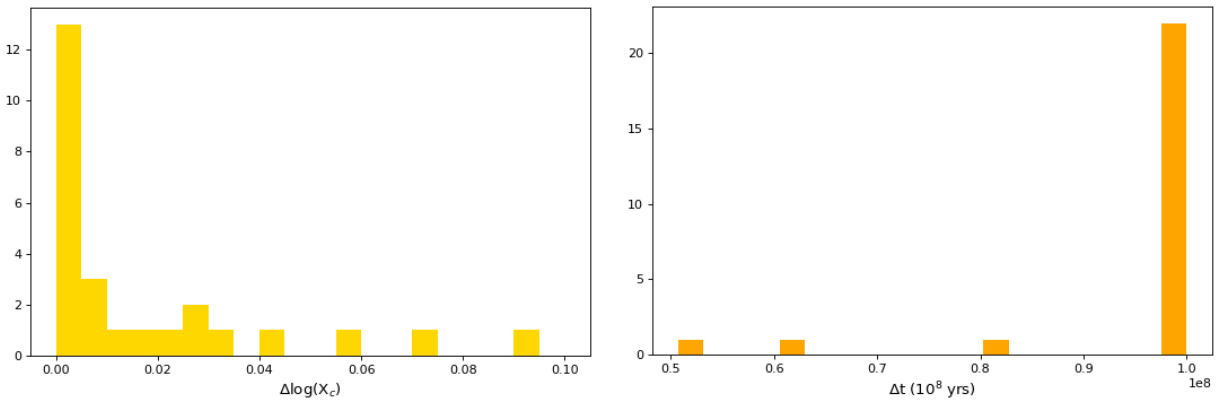

Figure 2.7: Histograms depicting the step conditions between consecutive profiles for the main-sequence (on the left) and the subgiant phase (on the right) of the solar-type star in Fig.2.6.

lation between the central temperature and the central density, with both increasing due to changes taking place around $r = 0$.

These three plots present the different evolutionary stages of the solar-type star through various colors, running from the PMS to the luminosity bump in the RGB. For each stage MESA takes a previous saved model for the star, and runs it using a group of user defined steps and stop conditions.

In order to initialize a track and simulate the pre-main sequence, MESA has a group of functions that take the parameter inputs and simulates the evolutionary track from the beginning, considering the formation of a protostar (through the condensation of interstellar matter at low

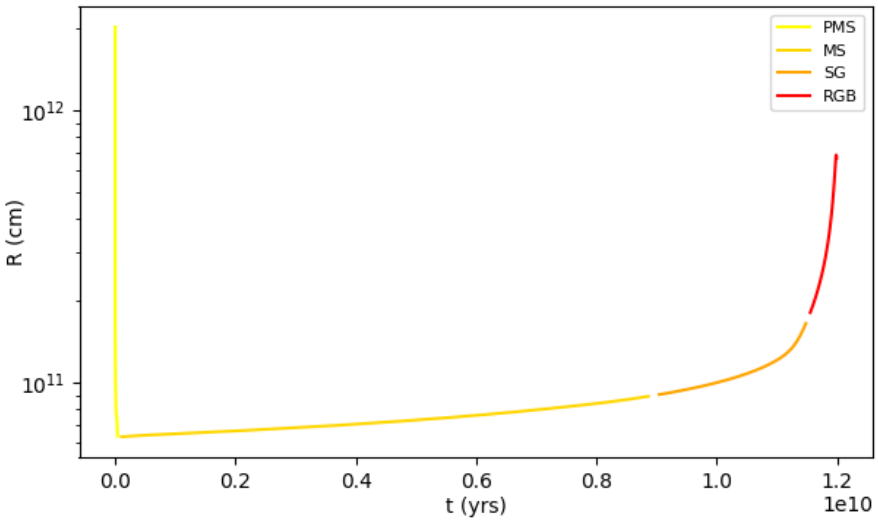

Figure 2.8: Evolution of the stellar radius with the age of a solar-type star.

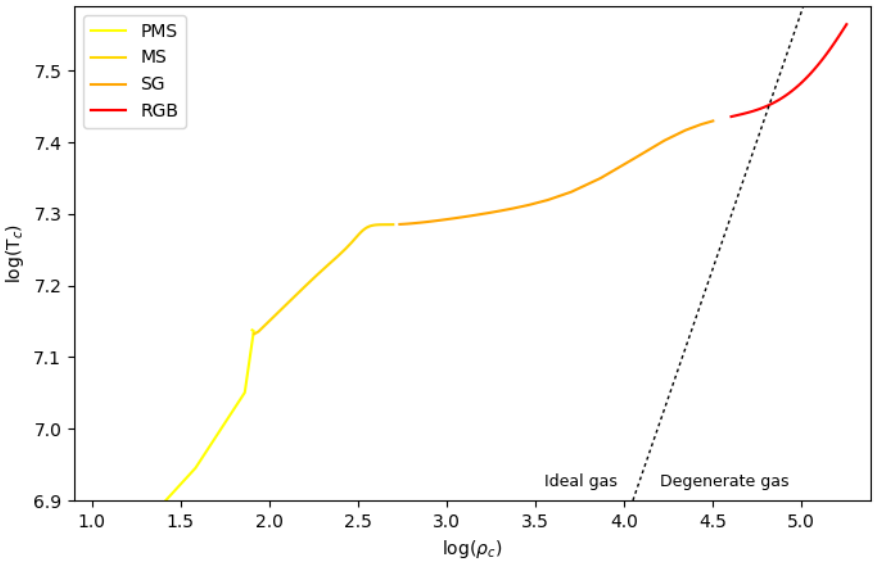

Figure 2.9: Representation of the evolutionary track of the simulated solar-like star as a function of the central values of temperature $\log(T_c)$ and density $\log(\rho_c)$, during the different stages of evolution. The black dashed line represents the separation between the conditions that allow the study of the gas in non-degenerate (that is well approximated by an ideal gas) and degenerate conditions. Under normal conditions, we need to go into the RGB phase to verify the effects of a gas in a degenerate state.

temperatures in hydrostatic equilibrium), its collapse and the formation of the new star.

The star then contracts, increasing its central temperature and density until the process of hydrogen fusion becomes efficient and releases enough energy to counteract the gravitational force - the ZAMS point. In our MESA simulations, this stage runs without a concrete step condition (since what we really want is to focus on the later phases), only stopping when $L_{\rm nuc} > 0.99\ L_{\rm ZAMS}$ (ie, when most of the luminosity of a star in this stage comes from the energy generation processes happening at the core).

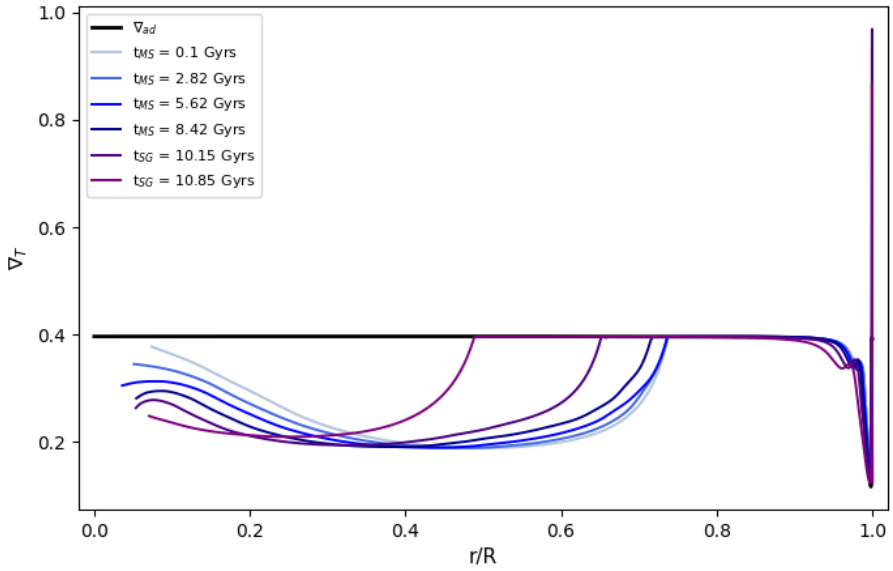

Figure 2.10: The gradient of temperature ∇T as a function of the relative stellar radius r/R for a solar-type star (with $M = 1$ M$_\odot$, $Z = 0.018$ and $\alpha_{\rm MLT} = 1.8$) at six different ages, during the main sequence and subgiant stages of evolution.

During the main-sequence, the one solar-mass star transforms hydrogen into helium in its radiative core, mainly through the pp-chain processes, which increase its central temperature and density, and transports the generated energy to the surface through radiative processes and convective motions. Computationally, the code takes the last previous saved model from the PMS stage, and starts determining the structure profiles in time considering variations in the central abundance of hydrogen up to $\Delta X_{\rm c} = 0.007$, until its value falls below $X_{\rm c} < 0.001$, marking the end of the main sequence. The star reaches the end of this stage with an age of $t = 9.05$ Gyrs, which corresponds to the longest phase of a star's life.

At the turn-off point, H-burning ceases to be the central energy generation process, and becomes a shell-burning process right outside the He-rich core. This causes the stellar envelope to expand, cooling down the star and moving it to the right in the HR diagram. This corresponds to the subgiant phase whose simulation was built considering a step of $\Delta t = 10^7$ yrs (although only saving 1 out of 10 models), and a terminating condition based on the increase of the density at the center (due to the contraction of the He-core), until $\log(\rho_{\rm c})$ becomes higher than 4.5 (Ref. [23]).

At last, we simulated the RGB phase with a contracting core, which increases the density and the temperature at the center, while the star continues its vertical ascension through the RGB line. During this time, the star also loses some of its mass through stellar winds, a collateral effect of its increasingly larger convective envelope. In this case, we constructed the time profiles in time steps of $\Delta t = 3 \times 10^6$ yrs from the end of the subgiant phase until the RGB luminosity bump that,

for this simulation, happens when the helium mass at the core becomes higher than 0.25 $M_\odot$[6].

Note that a good selection of steps and stopping conditions is important, so we can obtain a reasonable number of models along a given evolutionary phase that allow us to make a reasonable analysis of the parameter space, while maintaining the convergence of the solution and avoiding undersampling problems.

Fig. 2.10 illustrates the evolution of the internal structure of the one solar-mass star in terms of the temperature gradient. Recalling Eq. 2.11, we first conclude that the star with $t = 5.62$ Gyrs has a radiative core that goes up to $r \simeq 0.67$ $R_\odot$, and an outer convective envelope. But with time, the convective boundary sinks, reaching limits of $r \simeq 0.65$ $R_\odot$ at the end of the main sequence, and $r \simeq 0.45$ $R_\odot$ near the end of the subgiant phase.

The results found for the simulation discussed above agree with what we know from the literature, reassuring us that we have successfully applied the MESA code for this particular case. The steps and stop conditions applied to this case will be useful when simulating other stars, as well as when creating grids of models.

2.4.2 Stellar Mass

The stellar mass is one of the main parameters influencing the stellar structure and evolution. Fig. 2.11 illustrates the evolutionary tracks for 9 stars with the masses indicated in the inset, $Z = 0.018$ and $\alpha_{\rm MLT} = 1.8$, from the ZAMS until the end of the subgiant phase (previously defined as $\log(\rho_{\rm c}) \simeq 4.5$).

From Fig. 2.11, it is clear that higher mass stars present higher L and $T_{\rm eff}$ through their whole evolution. However, they also evolve faster than their low-massive counterparts. Stars with $M = 1.6$ $M_\odot$ were estimated to reach the end of the subgiant phase in $t = 1.95$ Gyrs, and stars with $M = 1.2$ $M_\odot$ would took around $t \simeq 4.38$ Gyrs to get to the end of the main sequence, and $t \simeq 5.55$ Gyrs to reach the end of the subgiant phase, while a star like the Sun ($M = 1$ $M_\odot$) would take around $t \simeq 8.84$ Gyrs and $t \simeq 11.06$ Gyrs to complete the respective phases. At the center (Fig. 2.12), the evolution of temperature and density is similar for the different masses considered, with both increasing with time, but never getting to a state of gas degeneracy.

It is noteworthy that low mass stars (specially 0.8 and 0.9 $M_\odot$ in Fig. 2.11) would take a time greater than the age of the Universe ($t_{\rm Universe} \simeq 14$ Gyrs) to complete the main sequence stage. With this in mind, we define an extra stopping condition, based on the age of the Universe, that allow us to reduce the computational efforts and the number of profiles when estimating the stellar

[6]This value does not come from literature, but from trial and error attempts and observation of the results.

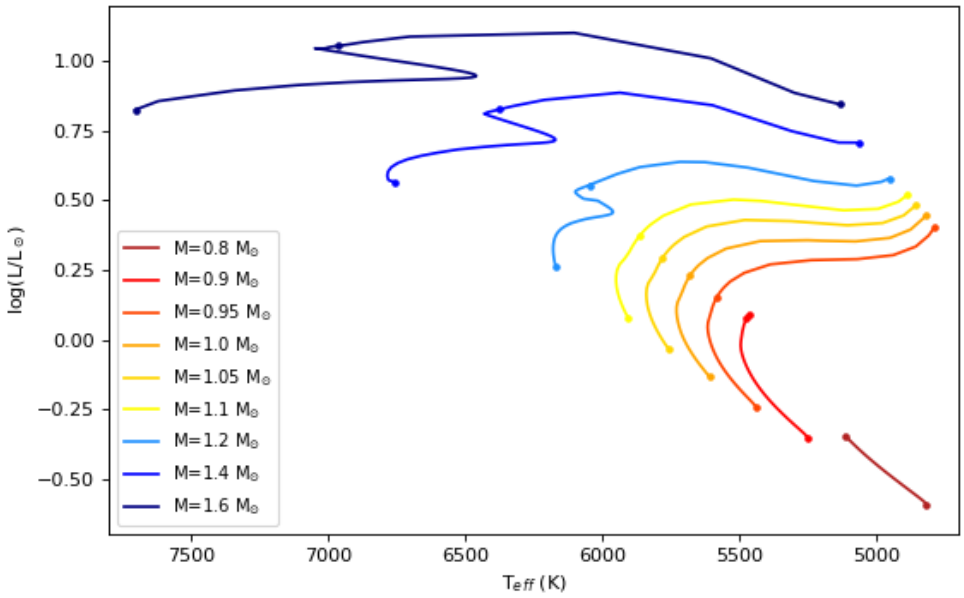

Figure 2.11: HR diagram presenting the evolutionary tracks of stars with masses $M = [0.80, 0.90, 0.95, 1.00, 1.05, 1.10, 1.20, 1.40, 1.60]$ $M_\odot$, for $Z = 0.018$ and $\alpha_{MLT} = 1.8$, from the ZAMS until the end of the subgiant phase. The points on each evolutionary track represent the ZAMS, the end of the main sequence, and the end of the subgiant phase (or the age of the Universe for low-mass stars), respectively.

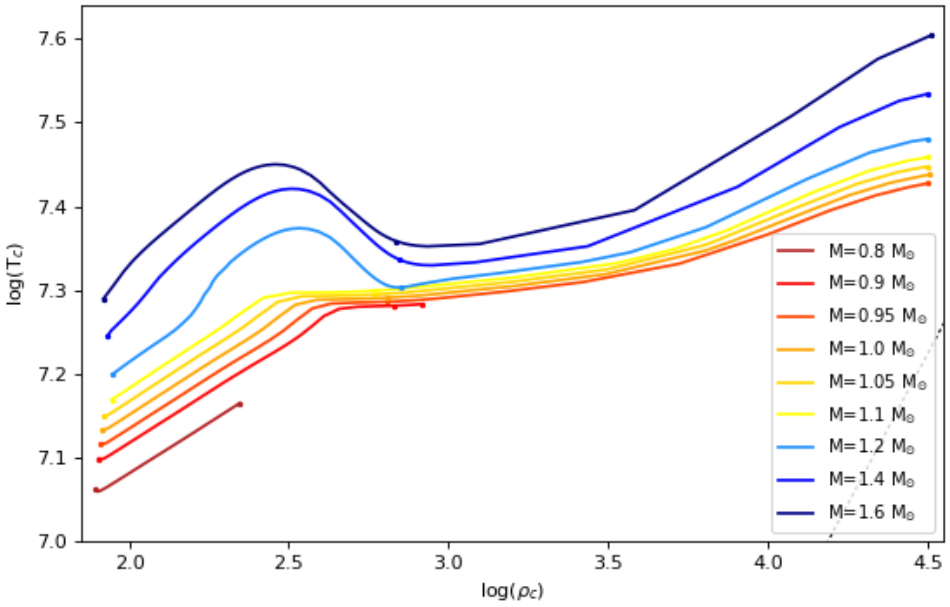

Figure 2.12: Representation of the evolutionary tracks in terms of the central values of temperature $\log(T_c)$ and density $\log(\rho_c)$, for stars with masses $M = [0.80, 0.90, 0.95, 1.00, 1.05, 1.10, 1.20, 1.40, 1.60]$ $M_\odot$, $Z = 0.018$ and $\alpha_{MLT} = 1.8$, from the ZAMS until the end of the subgiant phase.

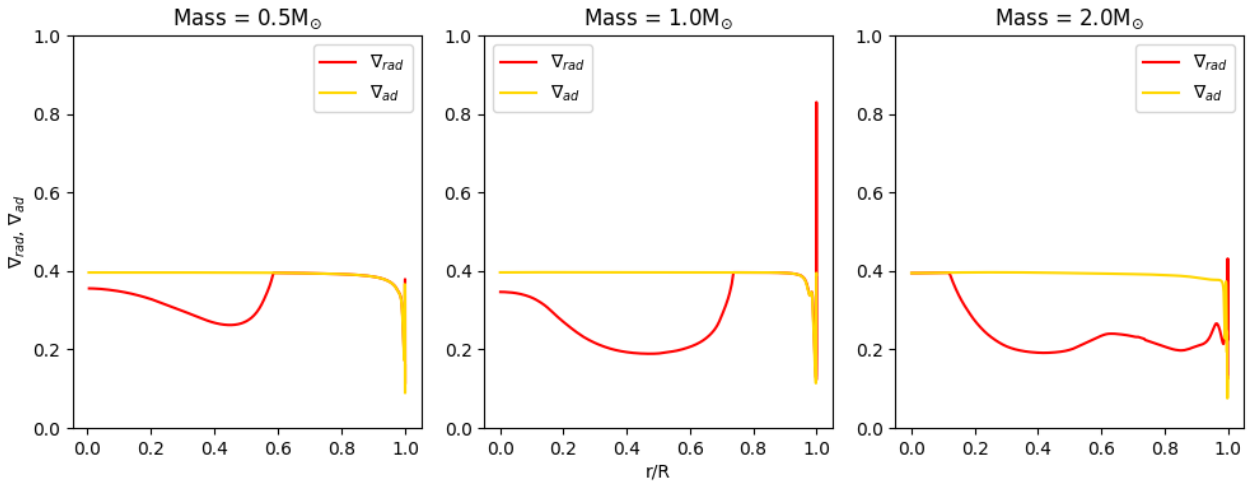

Figure 2.13: Estimated adiabatic and radiative gradients, $\nabla_{\rm ad}$ and $\nabla_{\rm rad}$, in the stellar interiors as a function or the relative radius r/R, for 3 stars with masses $[0.5, 1.0, 2.0]$ $\mathrm{M}_\odot$ during the main sequence (when $X_{\rm c} \simeq 0.5$).

parameters. By contrast, evolution tracks with $M \gtrsim 1.2$ $\mathrm{M}_\odot$ have a fast evolution, and present a hook-like feature at the end of the main sequence. These stars present a convective core during the main sequence that contracts when hydrogen is nearly depleted in order to maintain the energy production. This contraction leads to an increase in L and $T_{\rm eff}$ until the complete depletion of hydrogen in the center, which creates this prominent feature in the HR diagram. This feature can also be detected in Fig. 2.12 through the bumps at low densities for the more massive stars.

The influence of changing the mass on the stellar structure becomes even more evident when we apply the Schwarzschild criterion to verify which transport processes dominate in each region of the stellar interior. Fig. 2.13 displays these variations by presenting the relation between $\nabla_{\rm rad}$ and $\nabla_{\rm ad}$ for three values of mass. Recalling Eq. 2.11, we see that the star from Fig. 2.13(a), with $M = 0.5$ $\mathrm{M}_\odot$, has a radiative core up to $r \simeq 0.6$ R_* and a convective outer layer; the star from Fig. 2.13(b), with $M = 1.0$ $\mathrm{M}_\odot$, displays a radiative core up to $r \simeq 0.8$ R_* and a convective outer layer; and finally, the star from Fig. 2.13(c), with $M = 2.0$ $\mathrm{M}_\odot$, presents a small convective core up to $r \simeq 0.1$ R_* and a complete radiative outer layer. These results are in agreement to the energy transport theory discussed in Subsection 2.2.4.

2.4.3 Chemical Abundances and Metallicity

The second major parameter influencing the structural stratification of a star is the chemical composition, through the values of X, Y, Z, that define the mass fractions of hydrogen, helium and heavier elements in evolutionary codes, respectively.

Usually, both photometric and spectroscopic data coming from observations is used to provide a measurement of the bulk stellar metallicity in terms of the iron abundance[7] that is defined as

$$[Fe/H] \simeq \log(Z/X) - \log(Z/X)_{\odot}. \tag{2.16}$$

However, in stars with temperatures lower than $\sim 10^4$ K, the helium abundance is not directly measurable. Thus, a galactic enrichment law is often applied to determinate the helium abundance by relating the amount of fresh helium supplied by stars to the interstellar medium to their supply of heavy elements

$$\frac{\Delta Y}{\Delta Z} = \frac{Y - Y_{\rm ref}}{Z - Z_{\rm ref}}. \tag{2.17}$$

Based on both theoretical and observational studies, the enrichment law ratio $\Delta Y/\Delta Z$ can adopt values in the interval $[1.0; 3.0]$, depending on the observed region. For our MESA simulations, we considered a reformulation of the last equation by writing

$$Y = \frac{\Delta Y}{\Delta Z} Z + Y_i, \tag{2.18}$$

where $Y_{\rm i} = 0.2484$ is the primordial helium abundance (as given by Ref. [13]), and setting $\Delta Y/\Delta Z = 1.4$. Thus, by defining the initial metallicity Z_0 (ie the mass fraction of heavier elements at the ZAMS), we can determine Y_0 through Eq. 2.18, and X_0 through

$$X + Y + Z = 1. \tag{2.19}$$

The initial abundances have a clear effect on the evolution of stars, as shown in the HR diagram of Fig. 2.14, where for increasing values of the metallicity (varying from 0.008 to 0.020), the evolutionary tracks are shown to present both lower luminosities and effective temperatures. This is because opacity has a large dependence on the chemical composition, specially on the metallicity Z. For high values of Z, more opaque environments will have higher levels of photon absorption and scattering. This way, the energy transport becomes less efficient, reducing the values of L and $T_{\rm eff}$.

[7] Iron has been chosen to represent the heavier elements since it is by large the most abundant of the heavy elements in a star, but also because the fraction of each element comprising Z must be distributed accordingly to a chosen solar mixture, with a solar reference value $\log(Z/X)_{\odot}$ being defined between 0.0183 and 0.0245. For our models, we focused on the most commonly used solar metallicity mixture coming from Ref. [12].

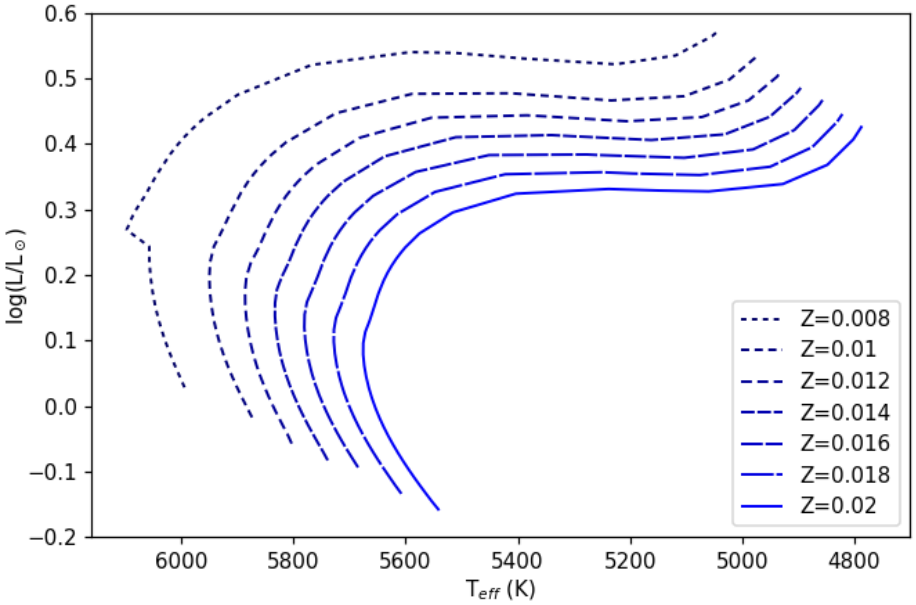

Figure 2.14: HR diagram presenting the evolutionary tracks of stars with metallicities $Z = [0.008, 0.010, 0.012, 0.014, 0.016, 0.018, 0.020]$, for $M = 1$ M$_\odot$ and $\alpha_{\rm MLT} = 1.8$, from the ZAMS until the end of the subgiant phase.

This effect also impacts the stellar age, which tends to increase for stars with higher Z. An example is the end of the subgiant phase of a star with $Z = 0.008$ that occurs around $t \simeq 8.31$ Gyrs, while a star with $Z = 0.020$ reaches the same stage with $t \simeq 11.88$ Gyrs.

During the evolution, the chemical stellar abundances vary due to the aforementioned energy generation processes. For low-mass stars, that are fully convective, the chemical composition is relatively constant throughout the stellar radius, at each instant. But for stars with a radiative core and a convective envelope, the chemical abundances in the core vary much more than in the outer region, that is not disturbed by these nuclear processes.

This second case is clearly depicted in Figs. 2.15 to 2.18 for the one solar-mass star studied before. Starting with mass fractions of $X_0 = 0.7084$, $Y_0 = 0.2736$ and $Z_0 = 0.018$, that are constant throughout the stellar radius at the ZAMS (Fig. 2.15), the mass fraction of H around the center decreases sharply while He increases due to nuclear reactions, while for $r > 0.2$ R$_\odot$, these variations are almost non-existent due to both the low rate of nuclear reactions and the radiative conditions of the layers around the core[8]. Z also changes with time, although the reactions that allow its variation are minimal during the main-sequence (Fig. 2.19). We need to wait for the star to enter the helium-burning phase for Z to undergo major changes in the core, when helium finally starts being used to produce heavier elements.

[8]For a solar-type star, the radiative core is expected to cover approximately 30% of the radius, but the radiative zone is expected to extend up to approximately 70% of the radius.

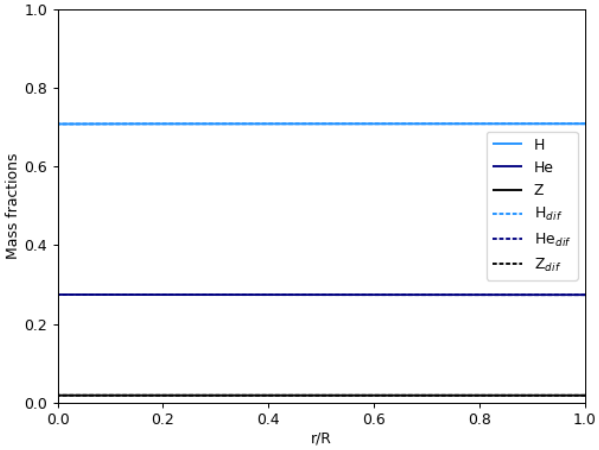

Figure 2.15: Chemical distribution of X, Y, Z for a solar-type star at the ZAMS ($t < 1$ Gyrs) with (full line) and without (dashed line) the presence of diffusion.

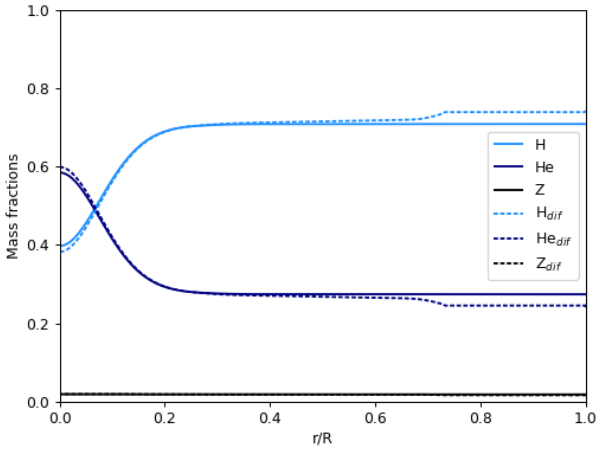

Figure 2.16: Chemical distribution of X, Y, Z for a solar-type star when $t = 4$ Gyrs, with (full line) and without (dashed line) the presence of diffusion.

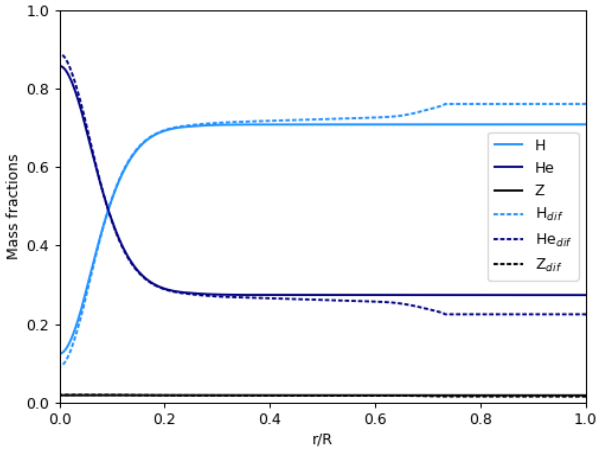

Figure 2.17: Chemical distribution of X, Y, Z for a solar-type star when $t = 7$ Gyrs, with (full line) and without (dashed line) the presence of diffusion.

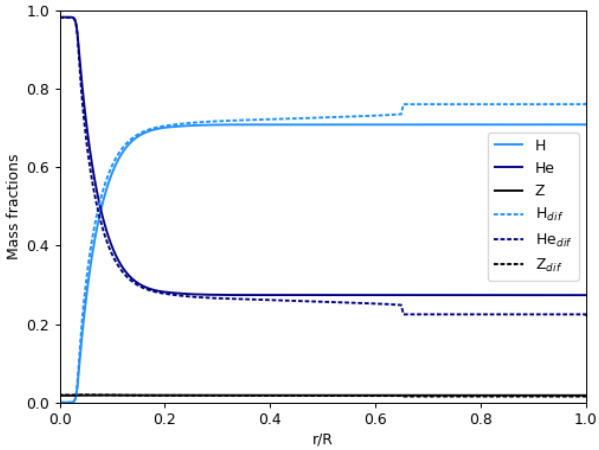

Figure 2.18: Chemical distribution of X, Y, Z for a solar-type star when $t = 10$ Gyrs, with (full line) and without (dashed line) the presence of diffusion.

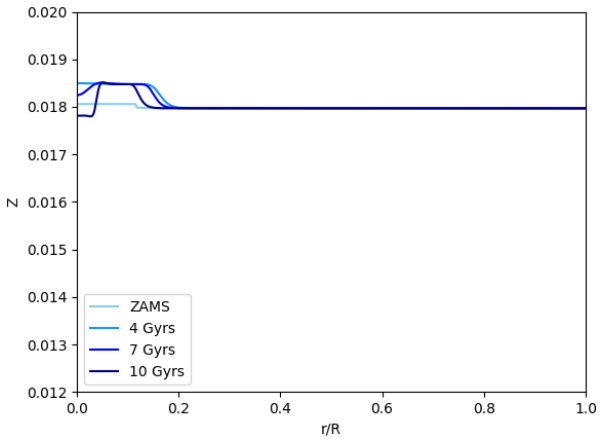

Figure 2.19: Evolution of Z for a solar-type star without diffusion. During the main sequence, the production of heavier elements is negligible, resulting in a near constant Z.

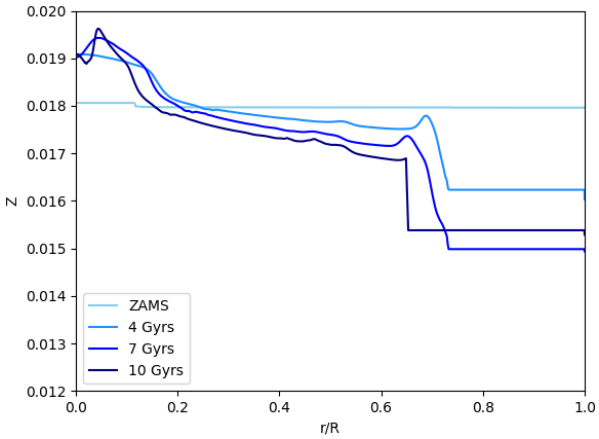

Figure 2.20: Evolution of Z for a solar-type star with diffusion. Due to its heavier molecular weight, these atoms metal enrich the core while its abundance decreases on the surface.

A significant complication to the understanding of chemical evolution in stellar interiors comes from the still poorly modeled physical processes responsible for the segregation of elements. Atomic diffusion is the process responsible for building abundance stratifications, dragging heavier elements towards the stellar center (mainly under the effect of gravity), and pushing lighter ones outwards. As a consequence, individual elements can be accumulated or depleted in certain layers, according to the variation of the radiative acceleration acting on them. These effects tend to require a quiet environment that prevents large-scale motions, but are highly dependent on both depth and photon absorption properties.

Fig. 2.21 illustrates the effects of the presence of diffusion during stellar evolution, comparing the evolutionary tracks of a solar-like star with (blue) and without (yellow) diffusion. Indeed, the star modeled with diffusion presents lower effective temperatures during the main-sequence, and a faster evolution in time, with a consequent difference in age around 0.44 Gyrs between both stars at the end of the subgiant phase. Due to atomic diffusion effects, heavier elements that sink in the stellar interior end up increasing the opacity in the radiative regions around the core. This will in turn reduce the energy transport, which lowers the effective temperature.

We can observe the effects of diffusion on the different elements in Figs. 2.15 to 2.20. The variation of the central abundances, with X decreasing and Y growing fast, is predominantly due to nuclear burning but it is also influenced by atomic diffusion processes.

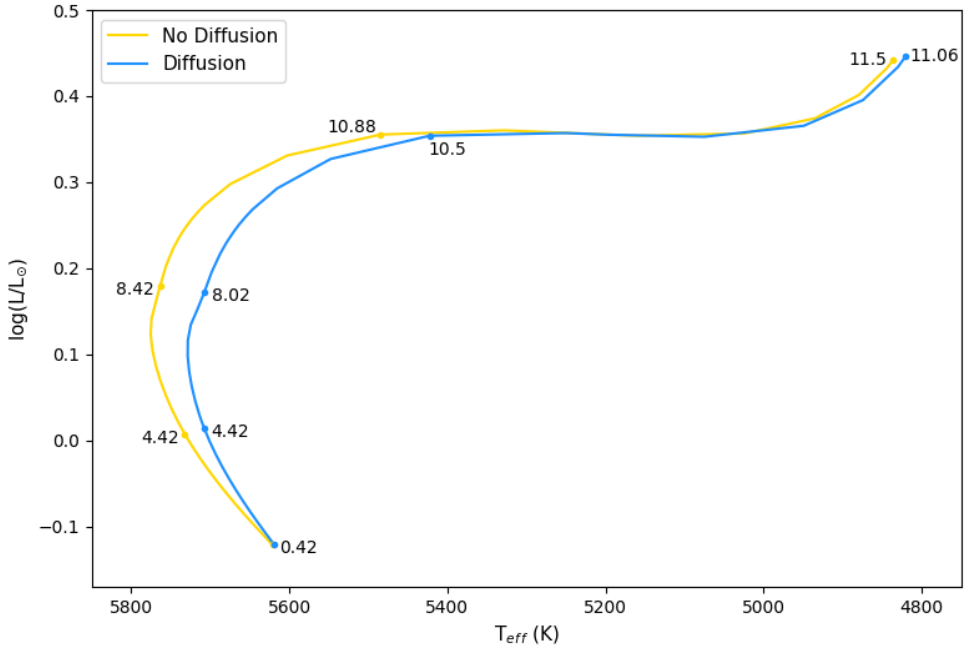

Figure 2.21: HR diagram representing the evolutionary tracks for a solar-type star with (blue) and without (yellow) diffusion. The numbers represent the age (in Gyrs) of each depicted profile in the evolutionary tracks, showing that diffusion affects the stellar age.

Another consequence of diffusion is the bump observed in Figs. 2.16 to 2.18 at $r \simeq 0.65$ $R_\odot$, a clear separation between the radiative interior and the convective envelope inside the solar-type star. While for $r < 0.65$ $R_\odot$ the hydrogen and helium mass fractions vary with depth, even when outside the region of energy production in the core, the convective motions on the outer layers keep mixing the elements so that their mass fraction remains constant with the radius, for $r > 0.65 R_\odot$.

Finally, the effects of diffusion on the heavy elements are illustrated by comparing Figs. 2.19 and 2.20. While Z is kept relatively constant in Fig. 2.19, in Fig. 2.20, where diffusion is considered, the mass fraction of heavy elements decreases in the outer layers, sinking into the stellar interior, and metal enriching the core.

2.4.4 Convective Efficiency

One of the most significant problems in producing accurate stellar models comes from stellar convection, a complex phenomenon that takes place over a large range of length scales, and it is typically approximated by implementing the mixing length theory (MLT) proposed in Ref. [14].

Here, the mixing length l_m is used as a rough approximation for the characteristic distance a fluid parcel can travel before mixing with the surrounding environment. It can be written as

$$l_\mathrm{m} = \alpha_\mathrm{MLT} H_P, \tag{2.20}$$

where

$$H_P = \left| \frac{dr}{d\ln P} \right| = \frac{P}{\rho g} \tag{2.21}$$

is the pressure scale height, and α_MLT is a free mixing length parameter with values in the interval $[1.5; 2.5]$, that ultimately defines the value of ∇ in a convective region (ie, defines the efficiency of energy transported by convection). This parameter can be determined via a standard solar calibration, an optimization process where three input parameters (usually Y, Z and α_MLT) are tuned to reproduce the properties of the Sun.

We simulated solar-type stars with $M = 1$ $M_\odot$ and $Z = 0.018$ in order to test the effects of different values of α_MLT in stellar evolution (Fig. 2.22). The most obvious consequence is the shift of the evolution tracks to higher temperatures with increasing values of α_MLT.

In fact, the higher the α_MLT, the more easily matter and energy are transported throughout the star by convective motions. A more efficient energy transport allows the core to produce even more energy, resulting in a higher luminosity of the star as represented in the HR diagram.

However, other parameters are not so much affected. For example, stars with higher α_MLT

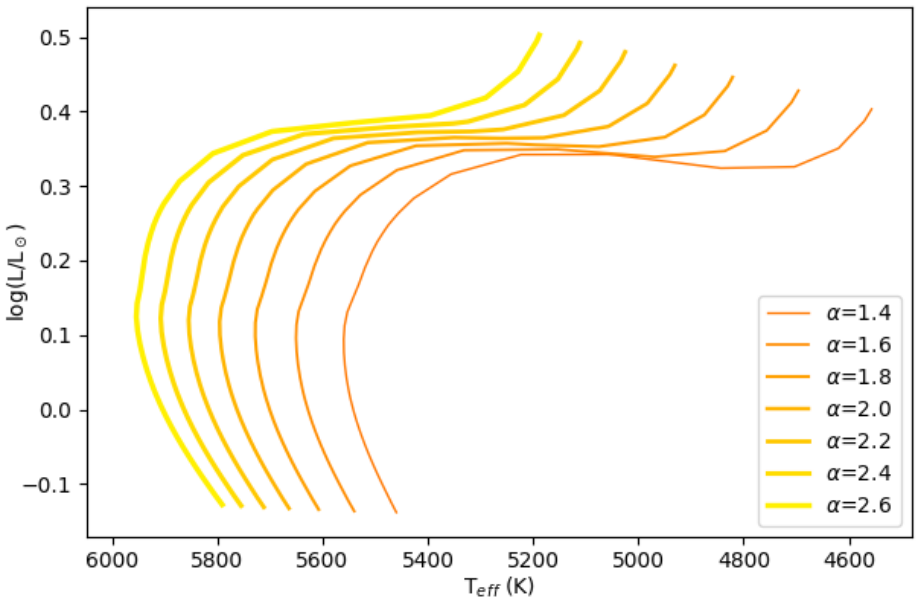

Figure 2.22: HR diagram showing the evolutionary tracks of stars with mixing length parameters $\alpha_{\rm MLT} = [1.4, 1.6, 1.8, 2.0, 2.2, 2.4, 2.6]$, for $M = 1$ M$_\odot$ and $Z = 0.018$, from the ZAMS until the end of the subgiant phase.

evolve faster, but the absolute differences are not that great: the simulation with $\alpha_{\rm MLT} = 1.4$ reaches the end of the subgiant phase with $t \simeq 11.12$ Gyrs, while the one with $\alpha_{\rm MLT} = 2.6$ reaches it with $t \simeq 10.93$ Gyrs.

Finally, Fig. 2.23 illustrates how convective regions of solar type stars are influenced by variations in the mixing length parameter. Reconsidering the Schwarzschild criterion (Eq. 2.11), we observe that the convective region of the star gets deeper as $\alpha_{\rm MLT}$ increases. For a star with

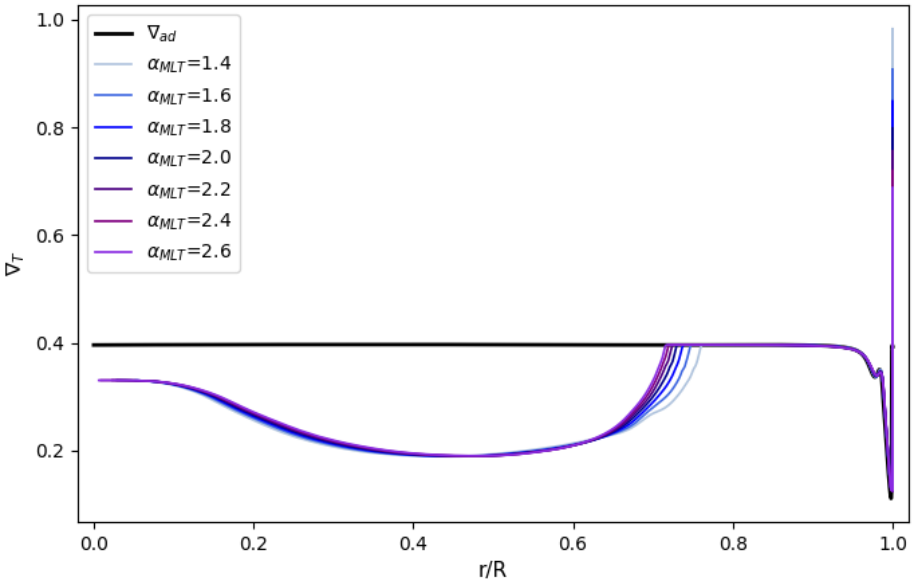

Figure 2.23: Variation of the temperature gradient ∇_T with the relative stellar radius r/R for a star with $M = 1.0 M_\odot$ and $Z = 0.018$, for different values of $\alpha_{\rm MLT}$ at $t = 4.62$ Gyrs. ∇_{ad}, that corresponds to the adiabatic gradient, is approximately the same for all cases.

$t = 4.62$ Gyrs and $\alpha_{\rm MLT} = 1.4$, the convective region corresponds to $r > 0.75$ R$_*$. This boundary decreases with increasing values of $\alpha_{\rm MLT}$, reaching $r \simeq 0.7$ R$_*$ when $\alpha_{\rm MLT} = 2.6$.

Chemical mixing can also occur beyond the convective unstable regions. In this context, convective overshoot deserves a reference since it has a significant effect on the stellar structure. The border between a radiative and a convective layer may be soft in the way that material on the convective side that approaches the boundary with enough momentum can penetrate into the radiative layer. This extension can be expressed as

$$l_{\rm ov} = \alpha_{\rm ov} H_{\rm p} \tag{2.22}$$

where $H_{\rm p}$ is the pressure scale height, and $\alpha_{\rm ov} < 0.25$. In the case of a convective core, overshoot can bring fresh fuel into it, prolonging the ongoing burning phase.

2.4.5 Construction of a Solar Grid

Before attempting to forward modelling different stars, we defined as a first task to recover the main parameters of the Sun from fitting a set of data based on a grid of models, which required building a grid of pre-computed models as a function of the inputs M, Z and $\alpha_{\rm MLT}$.

We used the MESA evolution code to generate the required model grid, considering that stellar masses would vary in the interval $M = [0.9 : 1.1]$ M$_\odot$ in steps of 0.5 M$_\odot$, the initial metallicities within $Z = [0.010 : 0.022]$ in steps of 0.002, and the mixing length parameters within $\alpha_{\rm MLT} = [1.6 : 2.2]$ in steps of 0.2. Values of X and Y were estimated through Eqs. 2.18 and 2.19. Atomic diffusion was switch on for this first grid, but convective overshoot was not included.

The tracks were evolved starting from the pre-main sequence to the Zero Age Main Sequence. However, all of the PMS models were discarded since the target star is known to be more evolved. We then evolved the models from the ZAMS to the point along the track where $t = 8$ Gyrs. Depending on the inputs of each track, the end point can vary between the middle of the main sequence stage up to the beginning of the RGB (for more massive stars). Each evolution track stored around 42 profiles, resulting in a total of 5970 profiles for all of the 140 tracks of the grid represented in Fig. 2.24.

In order to get a better comparison, we also decided to build a second grid in all similar to the first, except that models did not include diffusion.

These grids will later be used to obtain the theoretical seismic frequencies (in Chapter 3) necessary for forward modelling the Sun (in Chapter 4).

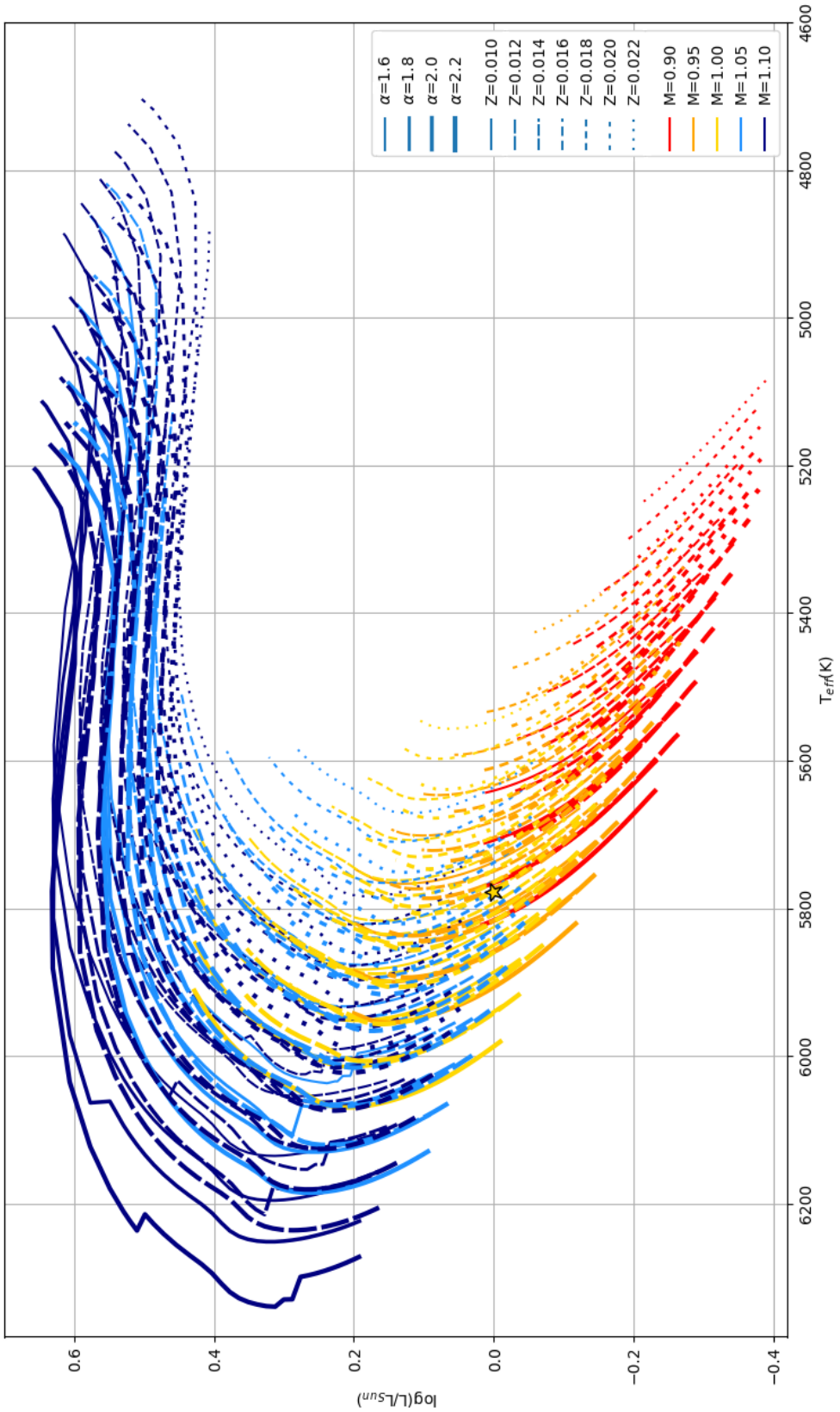

Figure 2.24: HR diagram for a solar-type grid with 140 evolutionary tracks constrained by 3 input parameters: stellar mass (with $M = [0.9, 1.1]$ $M_\odot$ in steps of 0.05), metallicity (with $Z = [0.010; 0.022]$ in steps of 0.002) and mixing length parameter (with $\alpha_{\rm MLT} = [1.6; 2.2]$ in steps of 0.2). The star represents the location of the Sun in the HR diagram ($T_{\rm eff} = 5777$ K and $\log_{10}(L/L_\odot) = 0.0$).

Chapter 3

Theory of Stellar Oscillations

Asteroseismology is a technique based on the study of the oscillation frequency spectra of a star, that allows us to comprehend its structure and dynamics. A star is capable to oscillate in different modes when suitably excited. Since these are sensitive to different regions on the star, they can be used to obtain reliable information about the chemical composition, stellar age, mixing terms, and internal rotation (otherwise not possible from properties like brightness and surface temperature). This fact has motivated a huge observational effort in this area (Ref. [1, 2, 15]).

Space missions like CoRoT by ESA, Kepler by NASA, TESS by NASA, and PLATO by ESA (this one yet to be launched) allowed for major progresses in stellar modelling, complementing the study of stars with spectroscopic data acquired from ground based observatories, and even motivating the development of other areas of astronomy.

This chapter reviews the basic theory behind stellar pulsations, considering small, adiabatic perturbations to a static, symmetric sphere in equilibrium, and putting emphasis on the physical properties of the different types of oscillation modes, in order to understand the results of the pulsation code that we will be using, GYRE (to be presented in section 3.3).

3.1 Equations for Stellar Pulsations

Assume a continuum gas with thermodynamic properties in space. Taking the hydrodynamic equations for an inviscid fluid, we can perturb and linearize them in order to consider small perturbations around the equilibrium configuration. The starting system of equations follows from the application of the basic laws of conservation of mass, linear momentum, and energy, expressed by

$$\begin{aligned} \frac{d\rho}{dt} &= -\rho\nabla\cdot\overrightarrow{v} \\ \rho\frac{d\overrightarrow{v}}{dt} &= -\nabla p + \rho\overrightarrow{g} + \overrightarrow{F}_{oth} \\ \frac{dq}{dt} &= \frac{dE}{dt} + p\frac{d(1/\rho)}{dt} \end{aligned} \tag{3.1}$$

where ρ is the fluid density, p is the pressure, $\overrightarrow{g}$ is the acceleration of gravity, $\overrightarrow{F}_{oth}$ are forces expressed per unit volume that may act on the fluid (besides gravity), E is the internal energy per unit mass supplied to the system, and q is the heat per unit mass supplied to the system.

We can then apply a perturbative analysis to the system, and obtain

$$\begin{aligned} \frac{d\rho}{dt} &= -\nabla\cdot(\rho_0\overrightarrow{\xi}) \\ \rho_0\frac{\partial^2\overrightarrow{\xi}}{\partial t^2} &= -\nabla\frac{dp}{dt} - \rho_0\nabla\frac{d\phi}{dt} - \frac{d\rho}{dt}\nabla\phi_0 \\ \nabla^2\frac{d\phi}{dt} &= 4\pi G\frac{d\rho}{dt} \\ \frac{dp}{dt} + \overrightarrow{\xi}\cdot\nabla p_0 &= \frac{\Gamma_{1,0}p_0}{\rho_0}\left(\frac{d\rho}{dt} + \overrightarrow{\xi}\cdot\nabla\rho_0\right) \end{aligned} \tag{3.2}$$

where $\Gamma_{1,0}$ is an adiabatic exponent related with the sound speed $c_0^2 = \frac{dp}{d\rho} = \frac{\Gamma_{1,0}p}{\rho}$ and G is the Newtonian gravitational constant. The solutions, describing small linear adiabatic perturbations[1] to a spherically symmetric equilibrium, are given by

$$\begin{aligned} f'(r,\theta,\varphi,t) &= \mathcal{R}\{f'(r)Y_l^m(\theta,\varphi)e^{-i\omega t}\} \\ \overrightarrow{\xi}(r,\theta,\varphi,t) &= \mathcal{R}\left\{\left[\xi_r(r)Y_l^m(\theta,\varphi)\hat{e}_r + \xi_h(r)\left(\frac{\partial Y_l^m}{\partial\theta}\hat{e}_\theta + \frac{1}{sin\theta}\frac{\partial Y_l^m}{d\varphi}\hat{e}_\varphi\right)\right]e^{-i\omega t}\right\} \end{aligned} \tag{3.3}$$

where f' stands for the scalar perturbations, $\overrightarrow{\xi}$ to the displacement perturbations, with radial and horizontal components ξ_r and ξ_h, and $\hat{e}_i$ are the unitary vectors of the spherical coordinate system (r,θ,φ).

The time dependence of the solution is associated to the angular oscillation frequency ω, whose values are determined by imposing boundary conditions (at the center and at the surface). This way, the system of equations and the associated boundary conditions constitute an eigenvalue problem which admits non-trivial solutions only for discrete values of the eigenvalues $\omega = \omega(n,l,m)$, where n is related to the number of nodes of the perturbation along the radial direction, and l and

[1]The adiabatic condition implies that no heat is exchanged with the element of fluid during the perturbation.

m are related to the angular dependence of the solutions, in particular to the horizontal scale of the perturbation and its orientation on the stellar surface. In the absence of physical agents that tend to break the spherical symmetry of the problem, the solution becomes degenerate in m, and the eigenvalues can now be written as $\omega = \omega(n, l)$.

The angular dependence of the solutions is given by the spherical harmonic functions Y_l^m, characterized by the angular degree l (a non-negative integer that defines the number of surface nodes), and the azimuthal order m (an integer between $-l$ and l that defines the subset of those that cross the equator). A clear example of these is shown in Fig. 3.1 through the Legendre functions described by $Y_l^m \propto P_l^m cos(\theta) e^{im\varphi}$. From the properties of the spherical harmonics, we have that

$$\nabla_{\rm h}^2 Y_l^m = -\frac{l(l+1)}{r^2} Y_l^m = -\kappa_{\rm h}^2 Y_l^m \tag{3.4}$$

where $\kappa_{\rm h}$ is the horizontal wavenumber of a local plane wave-like perturbation.

Using the solutions presented in Eq. 3.3 in the system of Eqs. 3.2, we can derive a new set of equations governing the radial-dependent amplitude functions $p'(r)$, $\phi'(r)$ and $\xi_r(r)$ obeying the following system

$$\begin{aligned} \frac{1}{r^2}\frac{d}{dr}\left(r^2\xi_r\right) - \frac{g_0}{c_0^2}\xi_r - \left(\frac{S_l^2}{\omega^2} - 1\right)\frac{1}{c_0^2\rho_0}p' &= \frac{l(l+1)}{r^2\omega^2}\phi' \\ \frac{dp'}{dr} + \frac{g_0}{c_0^2}p' - \rho_0(\omega^2 - N_0^2)\xi_r &= -\rho_0\frac{d\phi'}{dr} \\ \frac{1}{r^2}\frac{d}{dr}\left(r^2\frac{d\phi'}{dr}\right) - \frac{l(l+1)}{r^2}\phi' &= 4\pi G\left(\frac{p'}{c_0^2} + \frac{\rho_0 N_0^2}{g_0}\xi_r\right) \end{aligned} \tag{3.5}$$

where two characteristic frequencies are defined: the buoyancy (or Brunt-Väisälä) frequency N_0 (that serves as a marker to the stellar layers that are stable to convection), and the Lamb frequency S_l (that scales with the inverse of the dynamical timescale of the star, hence depending on the stellar radius), respectively given by

$$N_0^2 = g_0\left[\frac{1}{\Gamma_{1,0}}\frac{d{\rm ln}p_0}{dr} - \frac{d{\rm ln}\rho_0}{dr}\right] \quad , \quad S_l^2 = \frac{l(l+1)c_0^2}{r^2} \tag{3.6}$$

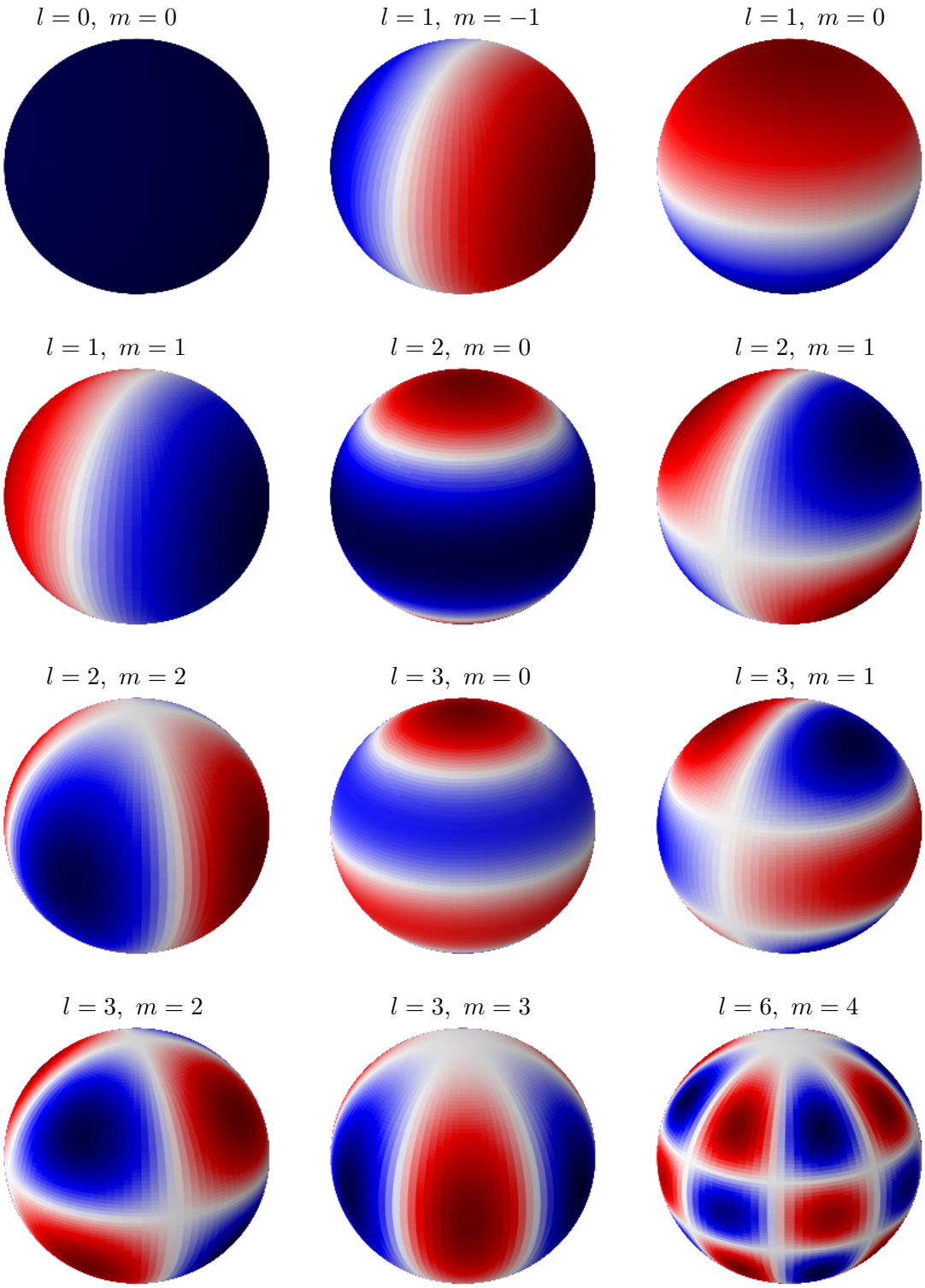

Figure 3.1: Examples of spherical harmonic functions Y_l^m (for the l and m indicated on top of each image) that describe the temperature distortion or the displacement on a stellar surface. The value l stands for the total number of nodal lines on the surface, while the azimuthal order m defines the number of nodal lines crossing the symmetry axis of pulsation, whereby $|m| \leq l$. Red and blue show perturbations with opposite signs, meaning that spherical harmonics with symmetric values of m to the ones indicated have the same format with exchanged colors, as explicitly shown for the cases $l = 1,\ m = \pm 1$.

3.2 Types of Oscillation Modes

Approximate solutions of the linear, adiabatic pulsation equations can be analytically analyzed under the Cowling approximation[2], assuming that local oscillations can be treated as under a plane-parallel layer with constant gravity. This way, the system of Eqs. 3.5 can be reduced to 2nd order on the variables p' and ξ_r, namely,

$$\begin{aligned} \frac{1}{r^2}\frac{d}{dr}\left(r^2\xi_r\right) - \frac{g_0}{c_0^2}\xi_r - \left(\frac{S_l^2}{\omega^2} - 1\right)\frac{1}{c_0^2\rho_0}p' = 0 \\ \frac{dp'}{dr} + \frac{g_0}{c_0^2}p' - \rho_0(\omega^2 - N_0^2)\xi_r = 0 \end{aligned} \tag{3.7}$$

Introducing a new variable $\Psi = \rho_0^{1/2} c_0^2 \nabla \cdot \xi$, the respective wave equation is given by

$$\frac{d^2\Psi}{dr^2} + \kappa_{\rm r}^2\Psi = 0, \text{ where } \begin{cases} \kappa_{\rm r}^2 = \frac{1}{c_0^2}\left[S_l^2\left(\frac{N_0^2}{\omega^2} - 1\right) + \omega^2 - \omega_c^2\right] \text{ is the local radial wavenumber} \\ \omega_{\rm c}^2 = \frac{c_0^2}{4H^2}\left(1 - 2\frac{dH}{dr}\right) \text{ is the critical frequency} \end{cases} \tag{3.8}$$

For the case considered, there are three families of solutions that can be identified in Fig. 3.2: (i) the acoustic (or p-) modes at higher frequencies, (ii) the gravity (or g-) modes at lower frequencies, and (iii) the f-mode. For comparison, the eigenfrequencies for the real Sun are shown on the right panel of Fig. 3.2, only displaying the observed p- and f-modes.

First, consider the higher frequency limit $\omega^2 \gg N_0^2$ corresponding to the p-modes, acoustic waves that are maintained by the gradient of a pressure fluctuation that can propagate in both radiative and convective regions. Their propagation cavity is determined by the combination of the Lamb frequency S_l (that is strongly dependent on the mode degree l) in the deeper regions, and the critical frequency ω_c (independent from l) near the surface. From Fig. 3.2, we can find that the frequency of p-modes increases when increasing the radial order n (when l is fixed) and the mode degree l (when n is fixed), both expected dependencies from the dispersion relation for acoustic waves. Indeed, acoustic waves with similar frequency but higher mode degree l present shallower propagation cavities, while their energy becomes more concentrated in the outer layers of the star.

Now, consider the low frequency limit $\omega^2 \ll S_l^2$ that corresponds to the g-modes. Internal gravity waves are maintained by gravity acting on the perturbation to the density, showing a constant spacing in the period domain, and only being able to propagate in convectively stable

[2]The Cowling Approximation consists on the disregard of the gravitational field perturbation when its variation happen on relatively short scales (much smaller than the radius of the star). In our case, it is valid for large values of $|n|$ or l.

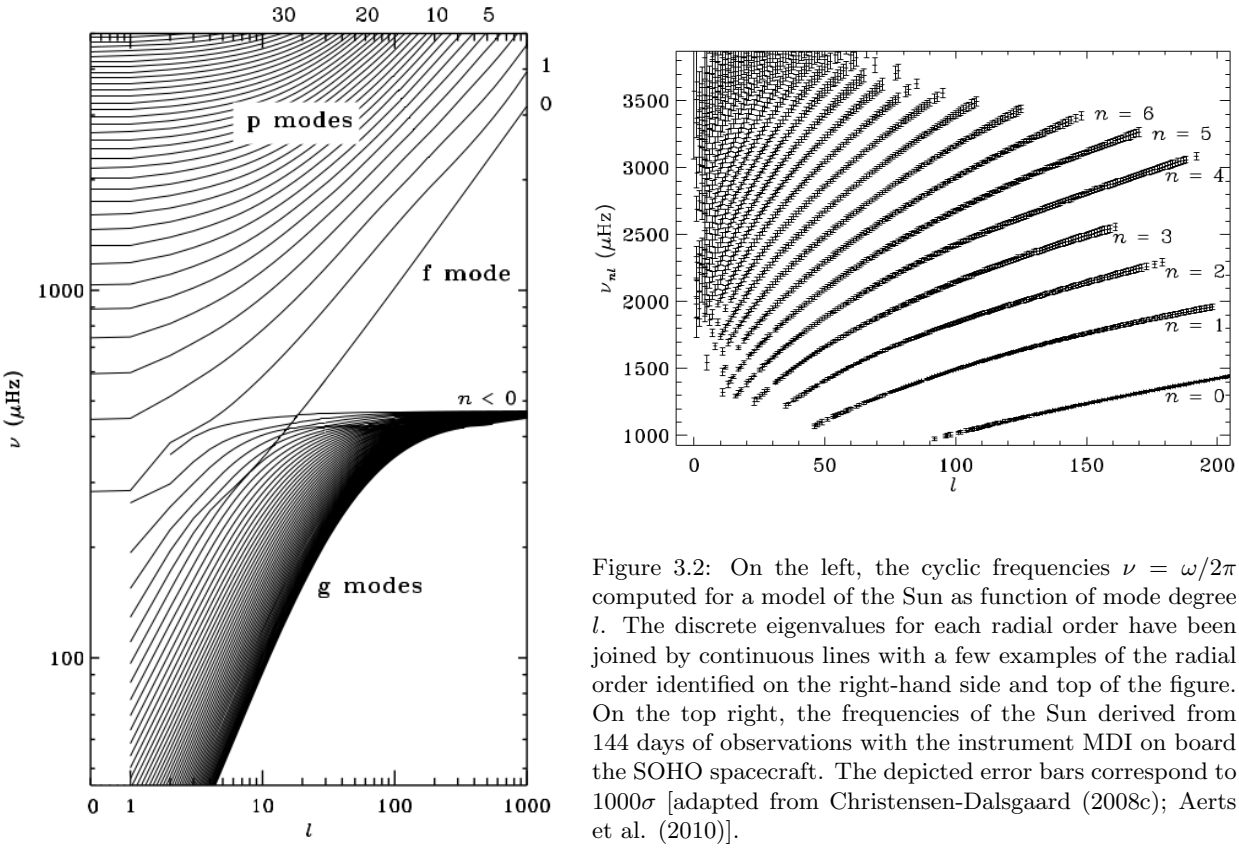

Figure 3.2: On the left, the cyclic frequencies $\nu = \omega/2\pi$ computed for a model of the Sun as function of mode degree l. The discrete eigenvalues for each radial order have been joined by continuous lines with a few examples of the radial order identified on the right-hand side and top of the figure. On the top right, the frequencies of the Sun derived from 144 days of observations with the instrument MDI on board the SOHO spacecraft. The depicted error bars correspond to 1000σ [adapted from Christensen-Dalsgaard (2008c); Aerts et al. (2010)].

regions. Since a fluid element in these regions cannot move strictly vertically, the gravity waves can never be associated to spherically symmetric perturbations, meaning that there are no gravity waves with $l = 0$. By Fig. 3.2, we observe that the frequency of g-modes decreases with increasing absolute value of the radial order $|n|$ (when l is fixed), and increases with increasing degree (when n is fixed). The maximum frequency for the g-modes corresponds to the maximum value of the buoyancy frequency N_0 in the model, which enters the dispersion relation associated to these modes. Their energy is mostly concentrated towards the innermost layers of the star, trapped below the convective envelope, in a cavity that is mostly independent of the mode degree.

Finally, the f-mode found between the p-mode and g-mode eigenfrequencies considers perturbations obeying $\delta p = 0$. This solution is identified as a surface gravity wave whose perturbation takes place without compression or refraction of the fluid, being independent of the stratification of the star.

For the case of the Sun, the lower frequency gravity modes are essentially trapped between the center of the star and the base of the convective region, while the highest frequency gravity modes are confined to the deeper layers (where the density is higher). This may explain why these modes have not been observed in the Sun yet (although claims of detections have been made, e.g., Ref [17]), in contrast to the p and f-modes previously mentioned.

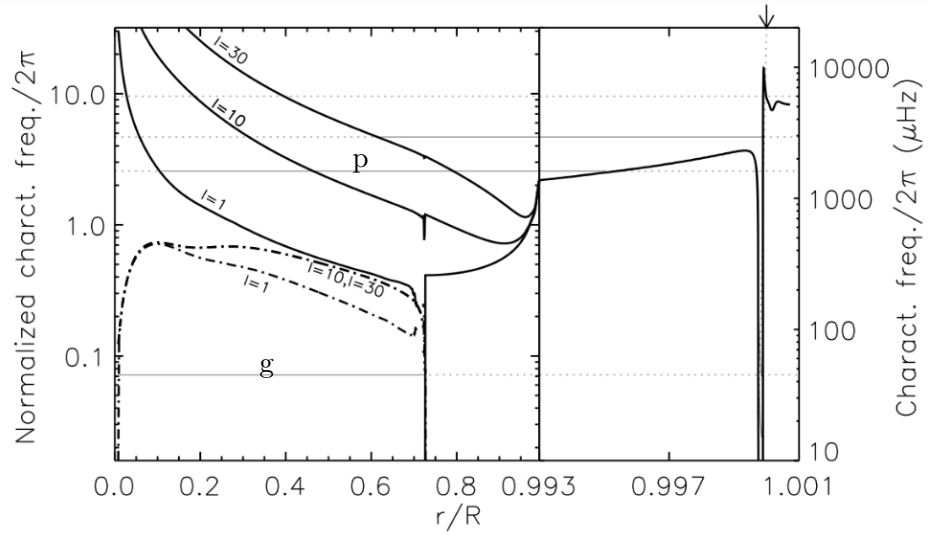

Figure 3.3: Lamb frequency S_l (continuous line) and buoyancy frequency, N_0 (dashed-dotted line) for mode degrees $l = [1, 10, 30]$, divided by 2π, against the fractional radius r/R for a model of the Sun during the main sequence. The left vertical axis shows dimensionless values of these characteristic frequencies obtained by multiplying them by $t_{\rm dyn}$. The right vertical axis indicates the true physical values. The light horizontal lines represented indicate the trapping regions for a g-mode with frequency $\nu \simeq 45$ μHz, and for two p-modes, one with $l = 1$, $\nu \simeq 1613$ μHz, and another with $l = 30$, $\nu \simeq$ 2936 μHz. At the top, we have a frequency $\nu \sim 6000$ μHz that is too high to be trapped inside the star. From the diagram, it is evident that there are regions where p- and g-modes can coexist (for $l = 1$, they coexist within $r/R \simeq [0.10; 0.73]$, and for $l = 30$, within $r/R \simeq [0.62; 0.73]$). These are regions prone to the formation of mixed modes [adapted from Ref. [1]].

For more massive stars, the innermost layers are convective, meaning the cavity of gravity waves become inner bounded by the edge of the convectively unstable core, while the convective envelope dwindles, allowing the propagation of g-modes near the surface.

For solar-like stars, as it evolves beyond the main sequence and the core contracts, the buoyancy frequency N_0 increases significantly towards the center, resulting in the appearance of mixed modes, ie, modes that are maintained by gravity acting on density perturbations in the deep interior, and, at the same time, by the gradient of the pressure perturbation in the outer layers. During the main sequence, the frequency of the p-modes is much higher than that of the g-modes (as shown in Fig. 3.2). However, as the buoyancy frequency increases during the subgiant phase, and the frequency of the p-modes decreases , the frequencies of p- and g-modes eventually overlap, which results in the appearance of mixed modes that tend to complicate the identification of individual modes in more evolved stars.

Finally, we note that stellar pulsators are usually separated in two groups, related to the nature of their oscillations: classical pulsators and solar-like pulsators. The first corresponds to stars with an excitation mechanism able to amplify the perturbations making them intrinsically unstable, which leads to oscillations of larger amplitude, hence to larger changes in the brightness of the star. These are found mostly in main-sequence stars more massive than the Sun and in the later stages of evolution. On the other side, solar-like stars in the main sequence, as well as subgiants

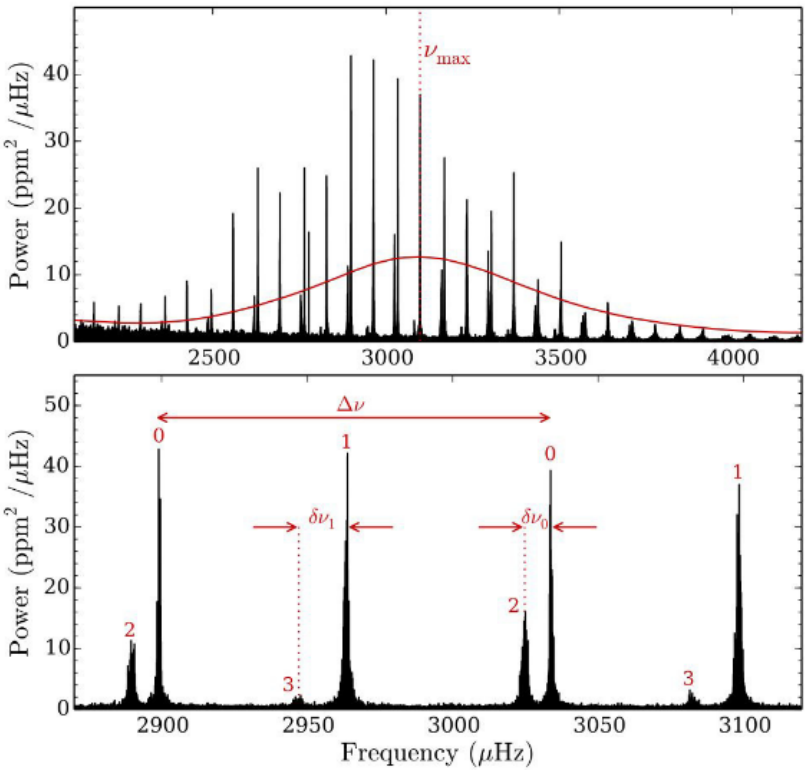

Figure 3.4: Power density spectrum of the Sun obtained from data acquired with VIRGO/SPM onboard the SOHO satellite. On top, the red line shows the power spectrum density smoothed by $3\Delta\nu$ and multiplied by 50, used to estimate ν_{max}. On bottom, a zoom of the upper panel illustrating a few modes, identified by mode degree. The large frequency separation, $\Delta\nu$, and the small frequency separations between pair of modes with degrees $l = 0, 2$, $\delta\nu_0$, and pairs with degrees $l = 1, 3$, $\delta\nu_1$, are also show [Ref. [1]].

and red giants present oscillations caused by turbulent motions in the convective regions that are intrinsically stable (meaning that small perturbations can be damped), being denominated as solar-like pulsators.

3.3 The Solar Oscillation Spectrum

For the case of the Sun, its oscillation spectrum is composed by a number of discrete frequencies, whose power is modulated over frequency, showing a Gaussian shape - typical of a solar-like pulsator, - whose maximum is defined as the frequency of maximum power, that has been suggested to scale with the surface gravity and effective temperature as $\nu_{max} \propto gT_{eff}^{-1/2}$.

The lower panel in Fig. 3.4 shows a close-up of the regular peak structure, with each mode being identified by the respective mode degree l. Two main separations are identified in the figure: the large separation between consecutive modes of the same degree, that has been shown to scale as $\Delta\nu \propto \sqrt{\rho}$, and the small separation between modes of similar frequency and degree differing by two, $\delta\nu$. Together, these scaling relations provide interesting and useful estimations of the stellar

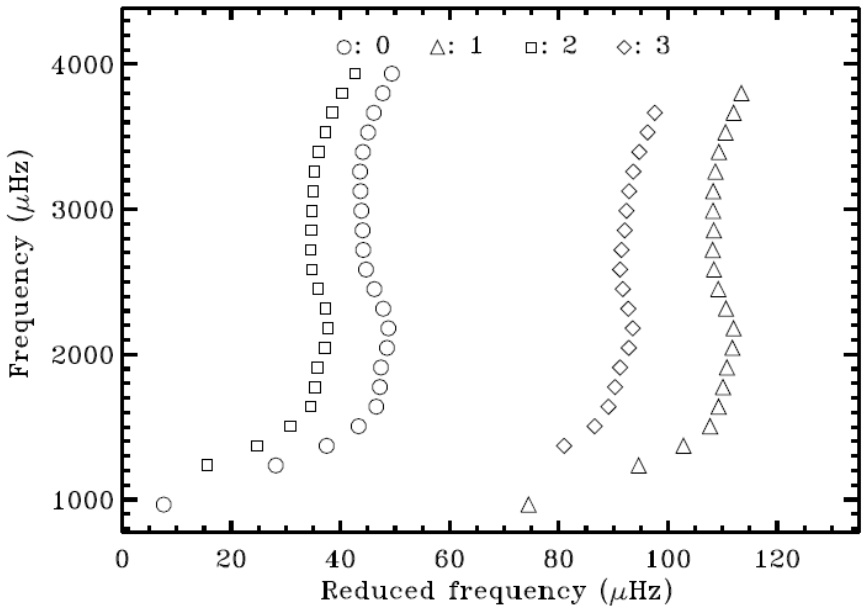

Figure 3.5: Échelle diagram for observed solar frequencies obtained with the BiSON network (Chaplin et al., 2002a), plotted with $\nu_{\max} = 830$ μHz and $\Delta\nu = 135$ μHz. Circles, triangles, squares and diamonds are used to represent modes of degree $\ell = 0, 1, 2, 3$, respectively (Ref. [18]).

mass and radius, once the effective temperature is known,

$$\begin{aligned}\left(\frac{R}{R_\odot}\right) &\simeq \left(\frac{\nu_{\max}}{\nu_{\max,\odot}}\right)\left(\frac{\Delta\nu}{\Delta\nu_\odot}\right)^{-2}\left(\frac{T_{\rm eff}}{T_{\rm eff,\odot}}\right)^{1/2} \\ \left(\frac{M}{M_\odot}\right) &\simeq \left(\frac{\nu_{\max}}{\nu_{\max,\odot}}\right)^{3}\left(\frac{\Delta\nu}{\Delta\nu_\odot}\right)^{-4}\left(\frac{T_{\rm eff}}{T_{\rm eff,\odot}}\right)^{3/2}\end{aligned} \tag{3.9}$$

We can divide the discrete frequencies of the full spectrum in equal intervals of $\Delta\nu$ that can be stack on top of each other to produce an échelle diagram, a plot that shows the listed frequencies as a function of the reduced ones,

$$\nu_{\rm reduced} = \nu.mod(\Delta\nu). \tag{3.10}$$

as in Fig. 3.5. For each interval, we notice that the 4 main frequency peaks associated with the mode degrees $l = 0, 1, 2, 3$ are preferentially paired in even or odd orders (as shown on the lower panel in Fig. 3.4), forming approximately vertical ridges. This is true during the main sequence, as shown by the échelle diagram in Fig. 3.5, but the appearance of mixed modes during the subgiant phase will shuffle the results.

3.4 GYRE Oscillation Code

The differential equations and boundary conditions that govern the small-amplitude, non-radial oscillations of a star about an equilibrium state - the so-called linearized stellar pulsation equations (Eq. 3.5) - constitute a two-point boundary value problem (BVP) that can be solved numerically. GYRE is an oscillation code built in FORTRAN (2008) to solve these equations, by calculating the (adiabatic and/or non-adiabatic) eigenfrequencies and eigenfunctions of an input stellar model (Ref. [19]).

Unlike previous prevalent codes, GYRE rightly implements a Magnus Multiple Shooting (MMS) scheme to determine the eigenvalues of the system, and solve the linearized pulsation equations. The MMS scheme solves BVPs defined by a system of linear homogeneous first-order ODEs defined on an interval, with a group of boundary conditions. As a linear homogeneous system matrix $\mathbf{S}$, the system only admits non-trivial solutions when the respective determinant vanishes. However, in the case of the pulsation equations, $\mathbf{S}$ implicitly depends on ω; thus, the stellar eigenfrequencies are the roots of a discriminant function defined as

$$\mathcal{D}(\omega) = \det[\mathbf{S}(\omega)], \tag{3.11}$$

that can be determined by using a suitable root-finding algorithm.

A typical GYRE run involves three main steps. First, a stellar model is either built analytically or read from files (in our case, the FGONG files produced with the MESA code), and calculation grids are constructed. Then, a scan through the frequency space searches for sign changes in the discriminant function $\mathcal{D}(\omega)$, which are used as initial guesses for a discriminant root-finding routine based on the algorithm described by Ref. [20]. After finding these roots, the corresponding eigenfunctions are reconstructed on a separate grid, using a secant-line approximation to the Magnus matrix within each sub-interval.

Experimental simulations made with this code proved its efficiency, showing its robustness while running and producing sensible outputs without manual intervention, with accuracy in the determination of eigenfrequencies and ability to address various physical processes that complicate calculations such as non-adiabaticity, rotation and magnetic fields. The communication between MESA and GYRE is accomplished through a simple application programming interface that allows the generation of the right format files ready to work in GYRE.

3.5 Seismic Properties of the Solar Grid

Lets focus on the results obtained with GYRE for the solar grid we built at Section 2.4.5, considering the evolution of a group of stellar tracks up to $t = 8$ Gyrs presented in Fig. 2.24. From its various configurations, we have chosen to use the GYRE code in its adiabatic settings to generate the theoretical oscillation frequencies, in order to compute the acoustic modes for harmonic degrees $l = [0, 1, 2, 3]$ below the acoustic cut-off frequency.

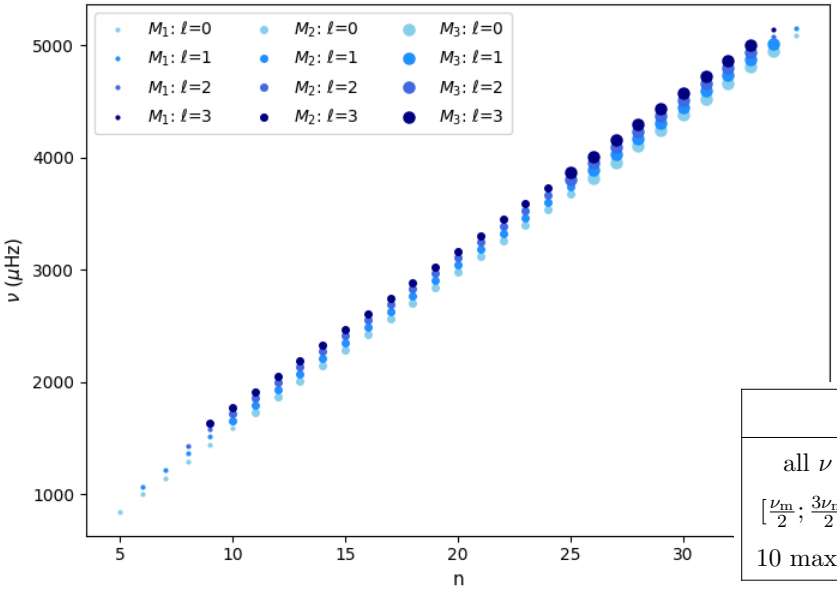

	$\ell = 0$	$\ell = 1$	$\ell = 2$	$\ell = 3$
all ν	135.13	135.05	134.96	135.17
$[\frac{\nu_m}{2}; \frac{3\nu_m}{2}]$	134.43	134.63	134.73	135.04
10 max ν	135.90	136.03	136.12	136.41

Figure 3.6: Representation of the frequencies as a function of the radial order, $\nu(n)$, for a single profile corresponding to $t \simeq 4.49$ Gyrs, for the angular degrees $\ell = [0, 1, 2, 3]$ represented by the increasing tones of blue. The different point sizes indicate the subgroups used to perform the polynomial fit in order to obtain the average slope (corresponding to $\Delta\nu$), considering the 3 methods referred in the text. Note that bigger points include all the small points. The results of the linear fit to estimate $\Delta\nu$ are presented in the table.

Figures 3.6 to 3.8 display the frequencies calculated by GYRE as a function of the radial order n, for different values of the mode degree l. For each set of points, we can determine the associated large frequency separation, $\Delta\nu$, through a linear fit.

A common question is which set of points allows the best determination of $\Delta\nu$: should we consider all of the frequencies, or only a subgroup of them? To address this, we considered a single profile of our grid, one with $M = 1$ M$_\odot$, $Z = 0.018$, $\alpha_{\rm MLT} = 0.18$ and $t \simeq 4.49$ Gyrs, and compared the model results with the observed values for the Sun, which has a p-mode large frequency separation of $\Delta\nu_\odot = 135.0$ μHz and a maximum power frequency of $\nu_{\rm max,\odot} = 3104.0$ μHz (for $t \simeq 4.57$ Gyrs).

We considered 3 different sets of points to compute $\Delta\nu$ as shown in the table associated with Fig. 3.6. Method 1 (all ν) produces the polynomial fit by considering all of the frequencies in the

plot. Method 2 ($\left[\frac{\nu_{\max}}{2}; \frac{3\nu_{\max}}{2}\right]$) presents the same estimation by considering a distribution of points around $\nu_{\max}$, calculated from

$$\frac{\nu_{\max}}{\nu_{\max,\odot}} = \left(\frac{g}{g_\odot}\right)\left(\frac{T_{\text{eff}}}{T_{\text{eff},\odot}}\right)^{-1/2} \quad \text{where } g = \frac{GM}{R^2} \tag{3.12}$$

where $\nu_{\max,\odot} = 3104.0\ \mu$Hz, $g_\odot = 274$ m.s^{-2} and $T_{\text{eff},\odot} = 5777.0$ K (see Ref. [23]). Finally, method 3 (10 max ν) produces the same estimation by only considering the 10 highest frequencies for each mode degree. It is clear from the table in Fig. 3.6 that the values for $\Delta\nu$ vary depending on both the method applied as of the number of modes considered. This emphasizes the importance of considering the same region of observed frequencies when comparing the estimated values with the observations.

Secondly, we want to study how the frequency separation $\Delta\nu$ evolves with time. The results for a solar-type star are shown in Fig. 3.7 for 3 moments of the stellar evolution and for the 4 different mode degrees. As the star ages during the main sequence, its radius R increases causing the mean density ρ to decrease with R^{-3}. Since $\Delta\nu \propto \sqrt{\rho}$, then the large frequency separation will decrease with time (regardless of the mode degree), as shown in the table of Fig. 3.7.

The evolution of frequencies (specially of p-modes frequencies) with time has a strong influence on the appearance of mixed modes during the later stages of evolution. This is shown in Fig. 3.8 for a solar-like star. During the main sequence (left plot), the star is well-behaved, only presenting observable p-modes for all of the mode degrees, arranged in approximately vertical ridges.

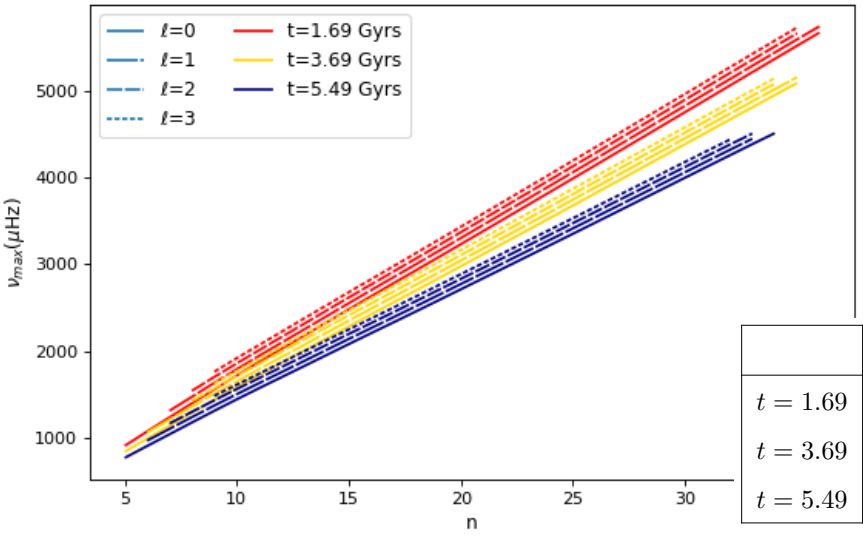

	$\ell = 0$	$\ell = 1$	$\ell = 2$	$\ell = 3$
$t = 1.69$	152.24	151.84	151.85	152.85
$t = 3.69$	140.43	140.25	140.12	140.39
$t = 5.49$	128.01	127.95	127.88	128.12

Figure 3.7: Representation of the frequency as a function of the radial order $\nu(n)$, for 3 different profiles of the solar evolution, corresponding to the ages indicated (in Gyrs) and represented by the different colors. The mode degrees $\ell = [0, 1, 2, 3]$ are represented by the different linestyles. The results of the linear fit to estimate $\Delta\nu$ are presented in the table.

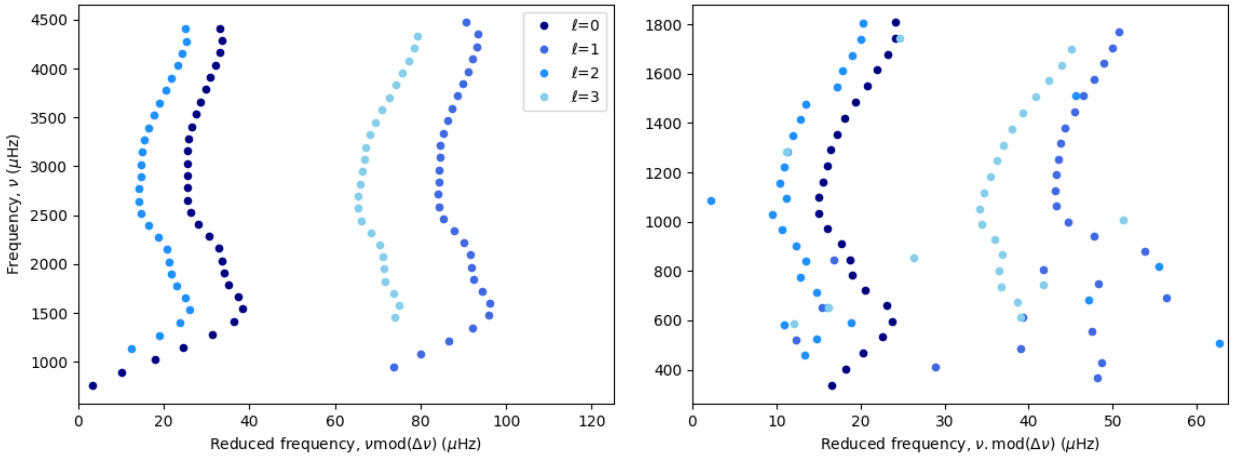

Figure 3.8: Échelle diagrams depicting the evolution of the oscillation modes of a solar like-star in the main sequence (on the left) and in the subgiant phase (on the right). The mixed modes characteristic of the subgiant phase correspond to the misaligned points from the correspondent ridges. The other points are fundamentally p-modes.

But when the star enters the subgiant phase (right plot), the increasing compactness of the deep interior structure results in the appearance of mixed modes. What we end up observing in the échelle diagram is some typical mixed modes, that correspond to the points with obvious departures from the regular behavior, among a number of modes that are fundamentally p-modes. As expected, radial modes do not show any difference, since g-modes with $l = 0$ are not possible.

We also want to understand how the large frequency separation $\Delta\nu$ is influenced by two of the main parameters of our grid, the stellar mass M and the metallicity Z. For that, we analised the frequencies of the various profiles, whose results are presented in Tables 3.1 and 3.2.

The mass-radius relation tell us that as the stellar mass increases, there is a roughly proportional associated increase of the radius. Since the density is more influenced by R than by M, ρ will decrease with increasing mass. This means that $\Delta\nu$ will decrease with increasing M (as shown in Table 3.1).

Mass ($M_\odot$)	$\ell = 0$	$\ell = 1$	$\ell = 2$	$\ell = 3$
$M = 0.95$	155.34	154.97	154.97	155.25
$M = 1.00$	140.43	140.26	140.12	140.39
$M = 1.05$	123.51	123.43	123.36	123.56

Table 3.1: Results of the polynomial fit to $\nu(n)$ when applied to models of different masses $M = [0.95, 1.00, 1.05]$ $M_\odot$ for a star with $Z = 0.018$ and $t = 3.69$ Gyrs.

Metallicity	$\ell = 0$	$\ell = 1$	$\ell = 2$	$\ell = 3$
$Z = 0.016$	137.26	137.12	137.06	137.26
$Z = 0.018$	140.42	140.26	140.12	140.39
$Z = 0.020$	143.17	143.01	142.87	143.12

Table 3.2: Results of the polynomial fit to $\nu(n)$ when applied to models of different metallicities $Z = [0.016, 0.018, 0.020]$ for a star with $M = 1$ $M_\odot$ and $t = 3.69$ Gyrs.

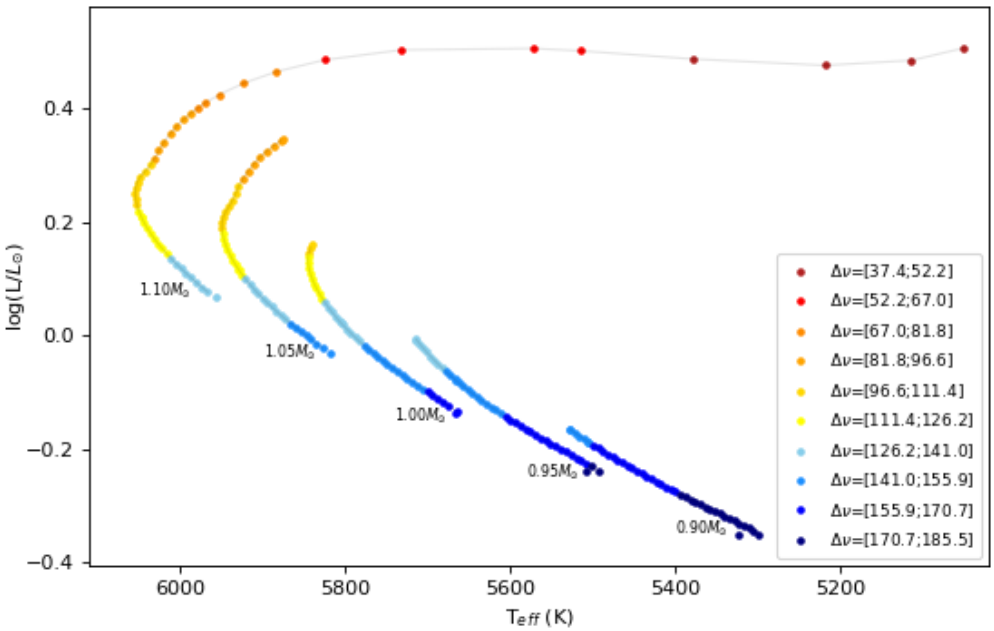

Figure 3.9: Contour map of the HR diagram for stars with different masses in our solar grid, highlighting the different large frequency separation intervals.

As previously discussed, the metallicity influences the opacity of the stellar models by influencing the way energy is transported throughout the star. Hence, its variation will influence the stellar radius. From Eq. 2.2, for $T_{\rm eff}$ constant, we see that for an increasing Z, the luminosity L decreases, which results in a decrease of the stellar radius R. Again, $\Delta\nu$ is influenced by R, this time increasing with increasing values of Z.

Finally, Fig. 3.9 summarizes most of the results discussed above. Indeed, different ranges of $\Delta\nu$ are covered during the stellar evolution according to different values of stellar mass, but two conclusions remain the same: (i) the values of $\Delta\nu$ are smaller for increasing stellar masses M, and (ii) $\Delta\nu$ decreases with the stellar age.

Chapter 4

Data Analysis in Asteroseismology

In order to characterize a star using asteroseismology, we want to obtain precise estimates of the individual parameters through a list of frequencies (and associated radial orders and mode degrees), and classical observables (such as L, $T_{\rm eff}$ and $[Fe/H]$). In this chapter, we introduce some topics on Bayesian theory and Markov Chain Monte Carlo (MCMC) techniques, both being used in the optimization code we implemented to our data (Ref. [23, 24]).

This optimization process searches a 3-dimensional parameter space (the grid in Fig. 2.24 presented as a function of mass, metallicity and $\alpha_{\rm MLT}$) for the solar models that match our list of frequencies. This procedure considers a forward modelling method, where we specify a model with a list of inputs that defines the current state of the system, and then, by applying the known physics to the system, it predicts how it will behave, its future state, so we can compare with the actual observations.

4.1 Optimization Process Method

An optimization process corresponds to a method that tries to optimize some specified parameters without violating a set of pre-defined constraints. In order to do this, the optimization code resorts to Bayesian statistics, which allows the determination of marginal probability density functions (PDFs) for each of the model parameters, while considering known prior information.

For a given model describing the system, let A represent the different stellar parameters we want to estimate, and I represent the observations that serve as constraints to the model (with assumed Gaussian distributed errors). Thus, the Bayes theorem gives that

$$p(A|I) \propto p(I|A)\ p(A) \tag{4.1}$$

where $p(A)$ denotes a certainty in our prior assumptions, $p(I|A)$ defines the likelihood function of A (ie how likely a certain value for the parameter is for a given set of observations), $p(I)$ plays the role of a normalization constant, and $p(A|I)$ corresponds to the posterior distribution, or, in our case, the PDF of each one of our stellar parameters A.

For each of the parameters of our grid (M, Z and α_{MLT}), we assign an uniform prior distribution, so that the likelihood function of obtaining a set of observables given a set of model parameters is

$$p(I|A) = \frac{1}{(2\pi)^{1/2}\sqrt{C}} . \exp^{-\chi^2/2} \tag{4.2}$$

where C is the covariance matrix of the observed parameters, and χ^2 is defined as

$$\chi^2 = \sum_{i=1}^{N} \left(\frac{I_i - \theta_i}{\sigma_i} \right)^2 \tag{4.3}$$

where I_i is the observed value, θ_i is the modeled value, and σ_i is the associated observed uncertainty (when dealing with independent observables).

The most commonly used technique to determine the PDFs of high-dimensional models are the Markov Chain Monte Carlo (MCMC) methods. These methods create samples from a possibly multi-dimensional continuous random variable in a space $\mathcal{S}^d$ that can be used to evaluate an integral over that variable, ie

$$\int_{\mathcal{S}^d} f(x)dx \quad \text{that can be approximated by} \quad \frac{1}{n}\sum_{i=0}^{n-1} f(x_i) \tag{4.4}$$

from where we can also calculate the expected value μ and respective variance σ. In practice, the optimization code defines a set of arbitrary points distributed in the space, the *walkers*, that develop an ensemble of chains corresponding to a stochastic process, accordingly to an algorithm that looks for places with high contribution to the integral to move into next, assigning them higher probabilities.

4.2 AIMS Optimization Code

AIMS (Asteroseismic Inference on a Massive Scale) is a Pyhton written code created to estimate credible intervals and errors for stellar parameters in a Bayesian way, from a set of pre-defined seismic and classical constraints (Ref. [24]).

The optimization process with AIMS takes three steps: the generation of a binary grid, the interpolation testing, and the characterization of the stellar parameters. From a group of user pre-defined analytical priors, the code looks into a list of pre-computed models given by the files obtained through MESA and GYRE codes. Then, it uses a MCMC algorithm combined with model interpolation that acts on the pre-defined grid, providing a better compromise between accuracy and efficiency while determining the required PDFs.

During this process, the code uses a two step interpolation procedure to explore the regions between the pre-defined models, namely (i) interpolating between the evolutionary tracks (which relies on the multidimensional Delaunay tessellation of the grid parameters M, Z and $\alpha_{\rm MLT}$), and (ii) interpolating along an evolutionary track (which consists in a linear interpolation between the two closest profiles). Both interpolation methods are outlined in Fig. 4.1 (Ref. [25]).

The main obstruction to constraining stellar models using individually-identified frequencies is the known systematic differences between theoretical models and observations caused by improper modelling of near-surface layers, which result in frequency shifts produced by poorly-modelling physical processes[1]. Motivated by the lack of a method for modelling these surface effects, Ref. [26] proposes a correction to the oscillation frequencies where these effects are modeled by terms proportional to $\nu^{\alpha}/\mathcal{I}$, where ν is the frequency of the oscillation mode and $\mathcal{I}$ is the corresponding inertia normalized by the total displacement at the photosphere (Ref. [15]). For solar-type models, the mode inertia decreases rapidly with frequency below $\sim$ 2000 μHz, before leveling out and reaching a minimum around 4000 μHz, suppressing the magnitude of the shifts at low frequency.

Arguments say that the perturbations caused by a magnetic field concentrated into filaments, which modifies the sound speed without affecting the gas density, cause a shift proportional to $\nu^3/\mathcal{I}$, while changes in the description of convection, which modify the pressure scale height, cause a shift proportional to $\nu^{-1}/\mathcal{I}$. Therefore, a combination of both terms is expected to produce significant better fits, resulting in a potential parametrization of the surface effects given by

[1] Poor-modelling of temperature gradients in the adiabatic layer, the use of the adiabatic approximation when calculating oscillation frequencies, and the absence of a description of interactions between convection and the oscillations are examples of these.

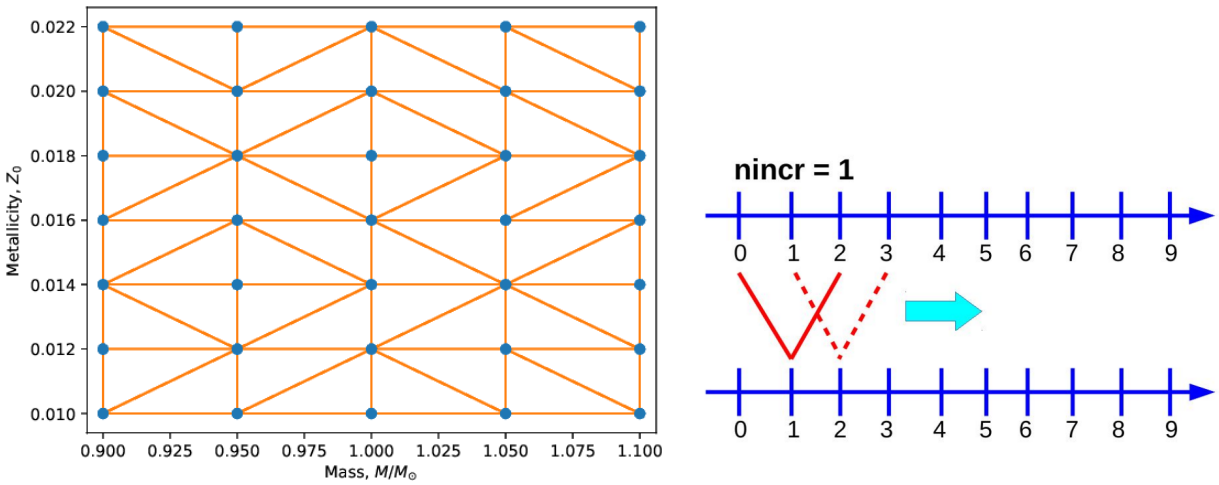

Figure 4.1: On the left, the interpolation plot shows the positions of the evolutionary tracks in the parameter space. Dots represent the previous tracks with which a new tessellation is created, as represented by the connecting lines. The tessellation is also displayed in the figure. On the right, a schematic plot presents the interpolation process along an evolutionary track. However, note that successive profiles are not necessarily equally spaced in age.

$$\delta\nu = \left(A_{-1} \left(\frac{\nu}{\nu_{\rm ac}} \right)^{-1} + A_3 \left(\frac{\nu}{\nu_{\rm ac}} \right)^{3} \right) / \mathcal{I} \tag{4.5}$$

where $\delta\nu$ is the frequency shift from the expected oscillation value, A_{-1} and A_3 are the coefficients that fit the stellar model under consideration, and $\nu_{\rm ac}$ is the acoustic cut-off frequency, given by

$$\frac{\nu_{\rm ac}}{\nu_{\rm ac,\odot}} \simeq \frac{g}{g_\odot} \left(\frac{T_{\rm eff}}{T_{\rm eff,\odot}} \right)^{-1/2} \tag{4.6}$$

where $\nu_{\rm ac,\odot} = 5000$ μHz, $g_\odot = 274$ m.s^{-2}, and $T_{\rm eff,\odot} = 5777.0$ K.

4.3 Discussion of the Results

We can now discuss the results obtained with AIMS, by analyzing the posterior distributions that resulted from the MCMC run of the solar model grid, limited by the group of classical and seismic constraints presented in Table 4.1 and Table A.7.1, respectively.

Note that equal weights have been given to the seismic and each classical constraints during the determination of χ^2, according to the following equation,

$$\chi^2 = \chi^2_\nu + \left(\frac{T_{\rm eff}^{\rm (obs)} - T_{\rm eff}^{\rm (mod)}}{\sigma(T_{\rm eff})} \right)^2 + \left(\frac{[Fe/H]^{\rm (obs)} - [Fe/H]^{\rm (mod)}}{\sigma([Fe/H])} \right)^2 + \left(\frac{L^{\rm (obs)} - L^{\rm (mod)}}{\sigma(L)} \right)^2 \tag{4.7}$$

	Luminosity ($L_\odot$)	$T_{\rm eff}$ (K)	$[Fe/H]$ (dex)
Sun	1.00 ± 0.03	5777 ± 65	0.0 ± 0.05

Table 4.1: Classical constrains for the Sun that will complement the asteroseismic parameters (in Table A.7.1) in the optimization process.

One of the outputs that comes from the optimization of the grid is a list of the frequencies of the oscillation peaks in the power oscillation spectrum, that can be used to produce an échelle diagram for the AIMS best model and the solar data (Fig. 4.2). For low frequencies, we observe an approximation between the values of $\nu_{\rm obs}$ and $\nu_{\rm theo}$ for all ℓ. But for higher frequencies, there is a systematic deviation between these two values, that tend to increase with ν. This is due to the already referred surface effects that are more significant for modes of higher frequency. This problem is solved during the interpolation step, by summing $\nu_{\rm theo}$ to an interpolation function (Eq. 4.5) in order to obtain $\nu^{\rm surf}_{\rm theo}$, which results in a better estimation of the frequencies (as shown by the nice overlapping between blue and purple points in Fig. 4.2).

The optimization code also estimated the coefficients from the interpolation function as $A^{-1}_{\rm surf} = (-6.127 \pm 7.803) \times 10^{-9} \mu$Hz and $A^{3}_{\rm surf} = (5.444 \pm 2.218) \times 10^{-16}$ μHz. These values show that effects due to convection have a larger impact on the frequencies than the effects due to magnetic fields.

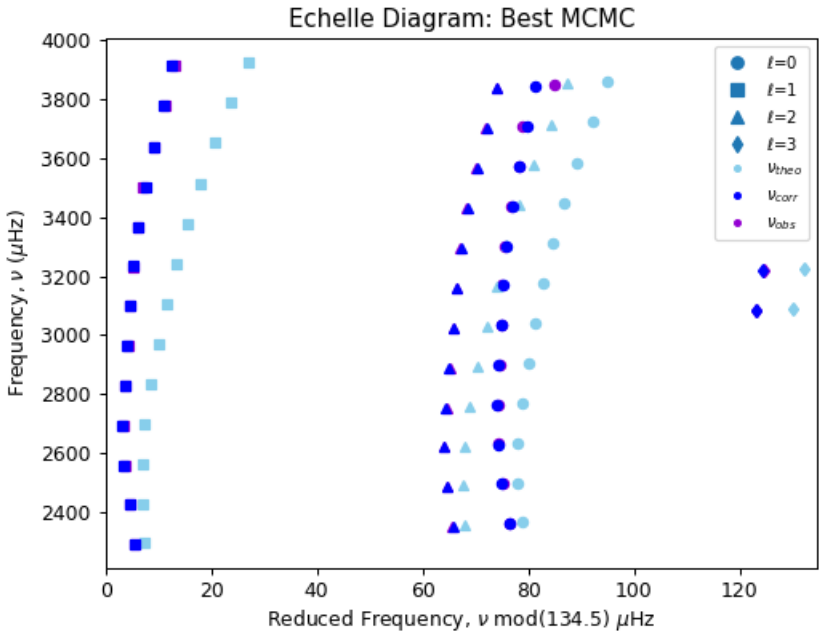

Figure 4.2: Échelle diagram for the best MCMC model of the Sun, showing the theoretical frequencies (in cyan), the surface corrected theoretical frequencies (in blue) and the observed frequencies (in purple) for orders of $\ell = [0, 1, 2, 3]$, considering the interpolation function given by Eq. 4.5 and taking into account both classical and seismic constrains previously mentioned.

The results obtained from the AIMS code are derived from the probability density functions represented in Fig. 4.3, from which we can extract the statistical mean value and the respective uncertainty (68% at 1σ) for each one of the required stellar parameters. The correlations between these parameters (mass, age, metallicity, $\alpha_{\rm MLT}$, and both surface parameters) are shown in a corner plot in Fig. 4.4.

At last, Table 4.2 summarizes the main numerical results for the model grid, presented in Fig. 2.24, and compares them with the real solar parameters and with estimations from other optimization codes and stellar grids. Fits with AIMS were performed considering the same grid with and without diffusion (whose results are labeled $\rm AIMS_{dif}$ and $\rm AIMS_{no\ dif}$). The results for the models without diffusion reproduce quite well the solar parameters, but not as well as when diffusion is considered. This is in agreement with the literature and with the helioseismic results that tend to prefer models with atomic diffusion.

In general, we can conclude that our grid of stellar models is quite capable to reproduce the Sun, with acceptable uncertainties between the estimated and the real values.

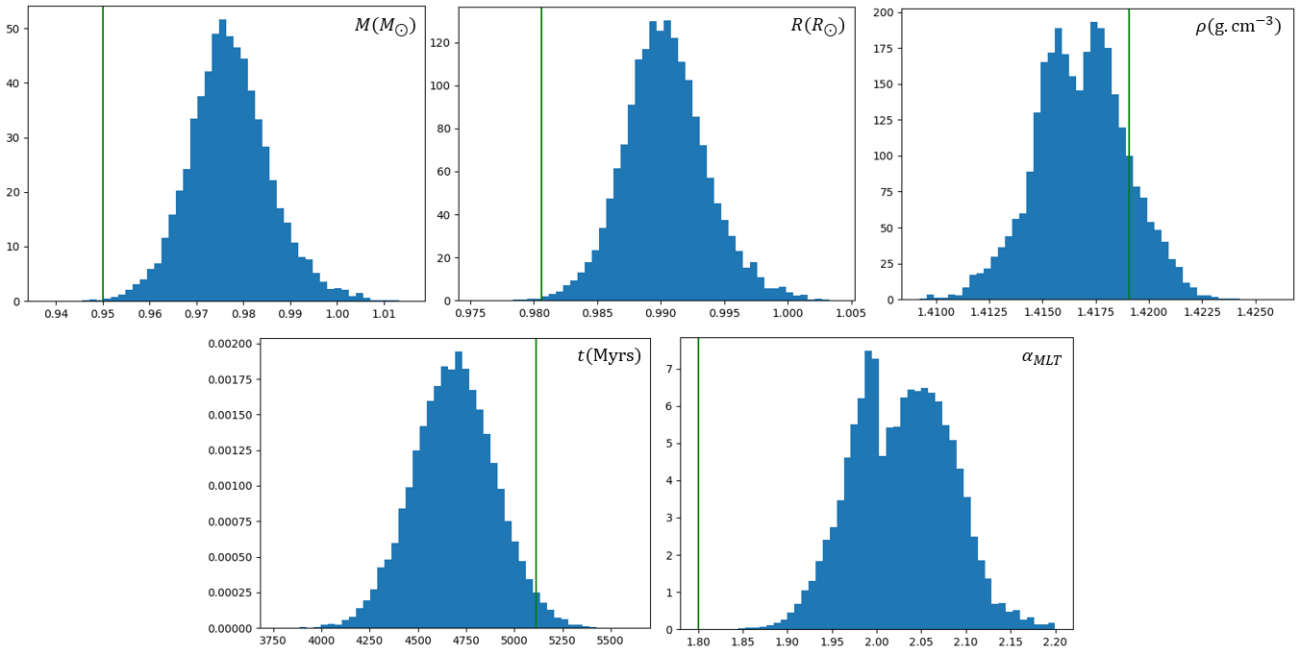

Figure 4.3: Probability distribution functions for the five main stellar parameters: stellar mass $M(\mathrm{M}_\odot)$, radius $R(\mathrm{R}_\odot)$, mean density ρ ($\mathrm{g.cm^{-3}}$), age t (Myrs) and mixing length parameter $\alpha_{\rm MLT}$. These were estimated to be (with an associated error of 1σ) 0.977 ± 0.009, 0.990 ± 0.003, 1.417 ± 0.002, 4688.52 ± 213.67 and 2.028 ± 0.055, respectively. The theoretical values are presented in the table below.

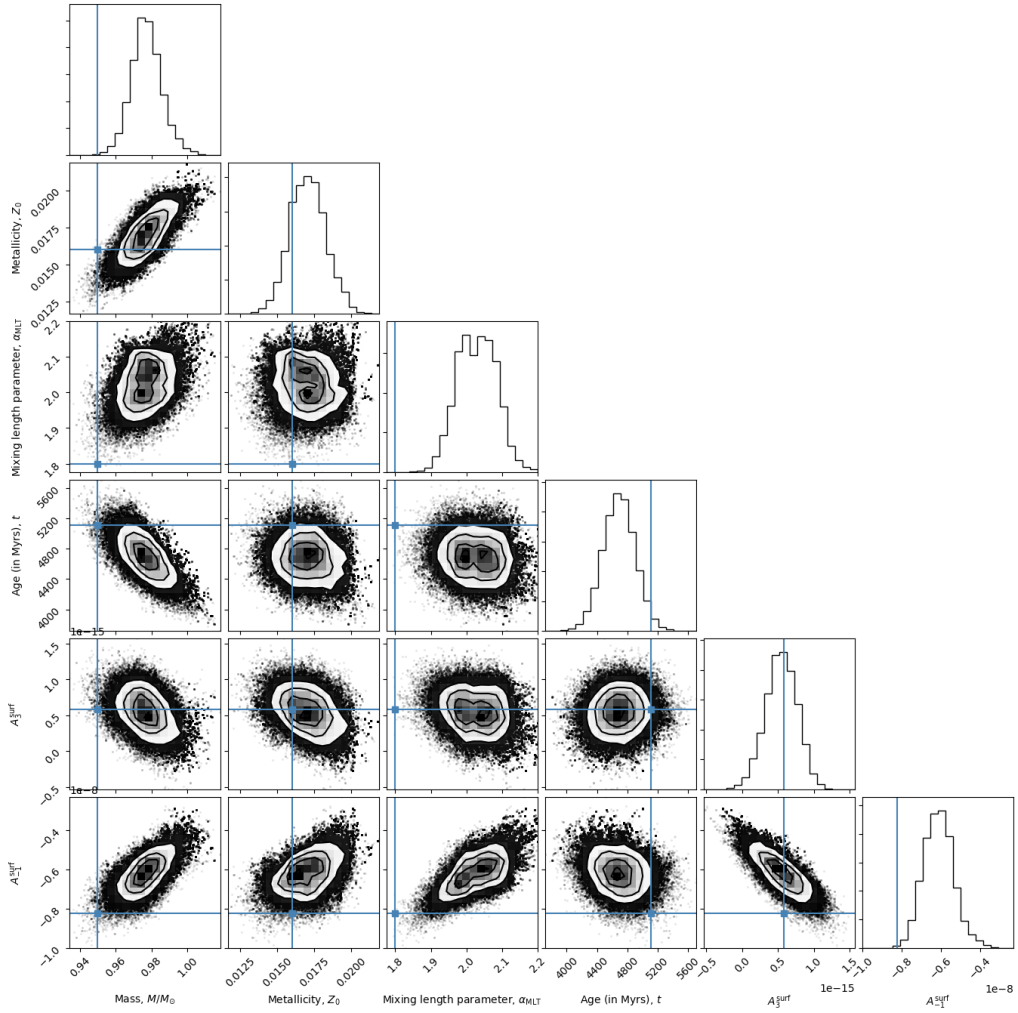

Figure 4.4: Corner plot with the correlation between the MCMC samples between the main different solar parameters: stellar mass M, initial metallicity Z_0, mixing length parameter $\alpha_{\rm MLT}$, age t and interpolation function constants A_3 and A_{-1}. The blue lines indicate the values estimated for the initial search grid.

	Mass ($M_\odot$)	Radius ($R_\odot$)	Age (Myrs)	Luminosity ($L_\odot$)	Density (g.cm^{-3})	Y_s
Solar Values	1.000	1.000	4570	1.000	1.408	0.248
AIMS $_{\rm no\ dif}$	0.968 ± 0.010	0.987 ± 0.004	5106 ± 238	0.926 ± 0.025	1.419 ± 0.002	0.270 ± 0.003
AIMS $_{\rm dif}$	0.977 ± 0.009	0.990 ± 0.003	4688 ± 214	0.955 ± 0.023	1.417 ± 0.002	0.272 ± 0.002
ASTFIT	0.986 ± 0.023	0.994 ± 0.008	4686 ± 393	0.972 ± 0.052	1.411 ± 0.003	0.249 ± 0.009
BASTA	$0.978^{+0.039}_{-0.030}$	$0.993^{+0.012}_{-0.012}$	4852^{+1181}_{-1069}	$0.976^{+0.054}_{-0.052}$	$1.411^{+0.021}_{-0.022}$	$0.247^{+0.012}_{-0.01}$
C2kSMO	1.021 ± 0.003	1.006 ± 0.010	4331 ± 85	1.084 ± 0.048	1.412 ± 0.048	0.245 ± 0.003
GOE	0.997 ± 0.006	0.995 ± 0.018	4859 ± 128	0.947 ± 0.041	1.412 ± 0.002	0.234 ± 0.009
V&A	0.927 ± 0.030	0.973 ± 0.015	4621 ± 200	0.937	1.418 ± 0.006	0.277
YMCM	$1.037^{+0.031}_{-0.047}$	$1.012^{+0.005}_{-0.005}$	5297^{+350}_{-350}	$1.008^{+0.043}_{-0.042}$	$1.406^{+0.001}_{-0.001}$	$0.248^{+0.01}_{-0.01}$

Table 4.2: Table comparing the actual values of the Sun with those estimated by various programs, including our results with AIMS (with and without diffusion), and the results obtained with ASTFIT, BASTA, C2kSMO, GOE, V&A and YMCM. These results follow the considerations in Ref. [27].

Chapter 5

The PLATO Simulations

5.1 PLATO Science Requirements

The PLATO mission (PLAnetary Transits and Oscillations of stars) is a group of 30 telescopes foreseen to be launched in 2026, with the mission to detect and characterize extrasolar planets by deriving accurate planetary radii, masses, and ages. A better understanding of the physical processes involved in stellar evolution is therefore a key factor of PLATO. This involves updating stellar models in terms of mixing, rotation, magnetism, etc., to eliminate the dependency of the estimated parameters on underlying physical assumptions used in stellar modelling, so we can improve the accuracy of the parameters.

The mission comprises a combination of three measurements and analysis methods: (i) the analysis of the photometric light curves aimed at detecting planetary transits and derive planet/star-radius ratios; (ii) the asteroseismic analysis of the same light curves, aimed at deriving accurate stellar masses, radii and ages, and (iii) the analysis of spectroscopic radial velocity measurements, to be acquired from follow-up observations from the ground, that will provide the required planet mass.

PLATO's goals include the determination of radii with an accuracy of 3-5% for exoplanets, and 2-4% for the host stars, and masses within a 10% accuracy for planets orbiting stars with a visual magnitude brighter than 10, and therefore about 10-15% for the mass of the host star. It also includes the determination of accurate ages up to 10% (for bright solar-like stars in the main sequence) through asteroseismology techniques applied to the host star. Since planet formation is fast, the age of the system will be assumed to be basically equal to the age of its host star (Ref. [4, 5]).

Before the mission is launched, it is necessary to verify that the pipelines are developed and the science requirements of the mission are met. To ensure that the stellar parameters (mass, radius and age) are retrieved within the accuracy set by the science requirements, a set of hares and hounds (H&H) exercises was designed. In these exercises, the hares produced artificial observational constraints for a set of simulated solar-like stars from theoretical stellar models. These observations include classical parameters, namely $T_{\rm eff}$, L and $[Fe/H]$, and seismic constraints, which include the individual frequencies for each star. Then, these are sent to the hounds who apply various methods to estimate the properties of these stars based on the simulated data produced by the hares. One of these applied methods uses a forward modelling approach to find the optimal models, the stellar properties, and the associated error bars.

A team at the University of Birmingham started the exercise by acting as the hares, producing a set of observations for 6 stars simulated in their subgiant phase. Another team at the University of Aarhus, built the dense model grid that was to be used by the hounds adopting a grid-based forward modelling approach, such as in our work. The 2000 evolutionary tracks that are part of the grid were computed only considering two variables: the stellar mass in range of $M = [0.6; 2.0]\ M_{\odot}$, and the initial metallicity (in the form of iron-content) within the range of $[Fe/H] = [-0.5; 0.5]$ dex. All of the models produced correspond to stars that were able to reach the subgiant phase before reaching a stellar age of 20 Gyrs. Considering the tendency of the large frequency separation $\Delta\nu$ to decrease with evolution time and the fact that the hares were known to be subgiant stars, a limit of 70 μHz was established as a condition for accepting models in the grid. Models were produced until the star reached the age of 20 Gyrs or until $\Delta\nu$ fell below 20 μHz.

Building a grid for stars in the subgiant phase raises problems related to the appearance of mixed modes. As previously mentioned, these are modes that are maintained by both gravity acting on density perturbations in the stellar interior and by the gradient of the pressure perturbation on the outer layers. The frequencies of these modes vary very rapidly as the star evolves, which renders interpolation less precise. This motivates the construction of a very dense grid. The increased number of models available for comparison allows a better identification of the individual modes, including the mixed ones. However, there is a significant drawback associated with this solution: when increasing the number of parameters of the models, the number of models on the grid extremely increases, and the computational efficiency will be quickly affected. In order to expand the grid to include more input parameters, we need to reduce the initial grid, at the same time as we ensure that the science requirements for the PLATO mission are still satisfied.

One interesting exception to the problem just described is the modelling based only on radial

modes ($\ell = 0$), along with the classical constraints. These modes are always purely acoustic, thus provide a convenient way to test whether the PLATO requirements may be satisfied without recurring to such a dense grid. With this in mind, our goal is first to test whether forward modelling based on this grid and on the radial modes alone is successful in reproducing, within the desired accuracies, the true stellar parameters for each of the hares. Further, we aim at investigating to what extent can the density of the grid be reduced while still retrieving stellar parameters within the accuracy set by the PLATO science requirements.

5.2 The Mass/[Fe/H] Simulated Grid

We start by analyzing the properties of the grid that was provided by a team from the University of Aarhus that is also participating in the H&H exercise. The grid consists of a set of 2000 evolutionary tracks computed in a two dimensional space: the stellar mass M, and the initial metallicity (in the form of iron-content) $[Fe/H]$. The computed tracks were provided along with a list of files containing both the global parameters associated with each profile (mass, radius, density, age...) computed with MESA, and the respective oscillation frequencies (associated to each pair of radial order and harmonic degree) computed with the Aarhus adiabatic oscillation package (ADIPLS) code (Ref. [29]).

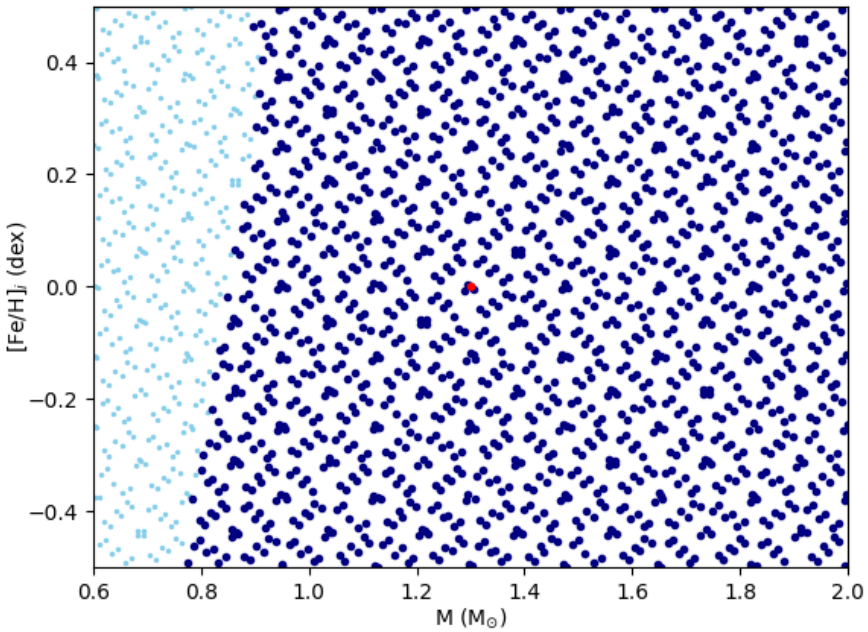

Figure 5.1: Distribution of evolutionary tracks in mass M and iron-content $[Fe/H]$ for the grid used in the H&H exercise. Each point represents the parameters for a single evolution track. However, only the dark blue points are considered in this study. The light blue points represent tracks with no models, since the large frequency separation of the respective star only falls below 70 μHz for an age beyond 20 Gyrs. The red point in the center of the grid represents the initial parameters for the first track *track0001*.

The distribution of the evolution tracks in mass M and iron-content $[Fe/H]$ is shown in Fig. 5.1. Some of the tracks (represented in light blue in Fig. 5.1) have no models, specially at low mass. This is because of the limit of 70 μHz in large frequency separation set in the construction of the simulations. For these models, the age goes beyond 20 Gyrs before the large frequency separation falls below 70 μHz, which means that these stars have not had the time to get to the subgiant phase yet. Although the age of the Universe is approximated by 14 Gyrs and, thus, not all tracks left in the grid (dark blue) reach the subgiant phase before that time, the value chosen as a lower limit for the large frequency separation ensures that the resulting probability density functions for the various parameters will not be truncated. Although this increases the number of models to be considered, slightly reducing the computational efficiency, it will not influence the results. From the HR diagrams of the tracks, we also identified that the limit of $\Delta\nu = 70$ μHz leads to the inclusion in the grid of some models that are still in the main sequence. This ensures that all models that describe the subgiant phase of each track are present on the grid.

The property that stands out from Fig. 5.1 is the unusual standardization of the grid. This is due to the way each pair of variables (M, $[Fe/H]$) was chosen. The grid was created using an algorithm involving Sobol sequences, a quasi-Monte Carlo (QMC) method that uses low-discrepancy sequences from a group of free parameters calibrated by the user (Ref. [30]). Such method creates a more uniformly distributed grid than random points, but with fewer points than a Cartesian grid, which improves the computational efficiency and the rate of convergence of the algorithm.

For a low-discrepancy sequence, if we consider a subgrid with tracks *track0001, track0002, ..., track1000*, and another with tracks *track1001, ..., track2000*, the parameters will be uniformly distributed in space in both subgrids, but with smaller density. Likewise, if we divide the grid in four sequential subsets and so forth. This property can be observed in both Figs. 5.2 and 5.3. Both the 2 and 4 subgrids present a good level of uniformity, which is important if they are to be considered for the forward modelling study. In our grid, this uniformity happens for every block of tracks of size 4n+1, where n is an integer. This is because the first track *track0001* is placed right in the middle of the grid, without belonging to any of the subspaces, so the grid will only exhibit its uniformity strength for every 4 new points added.

The success of quasi-Monte Carlo methods (and, in particular, Sobol sequences) lies at their uniformity in low-dimensional projections. Many practical problems have low effective dimensions, which means that either the integrand depends mostly on an initial handful of variables, or the integrand can be well approximated by a sum of functions with each one depending on a small number of variables at a time, such as

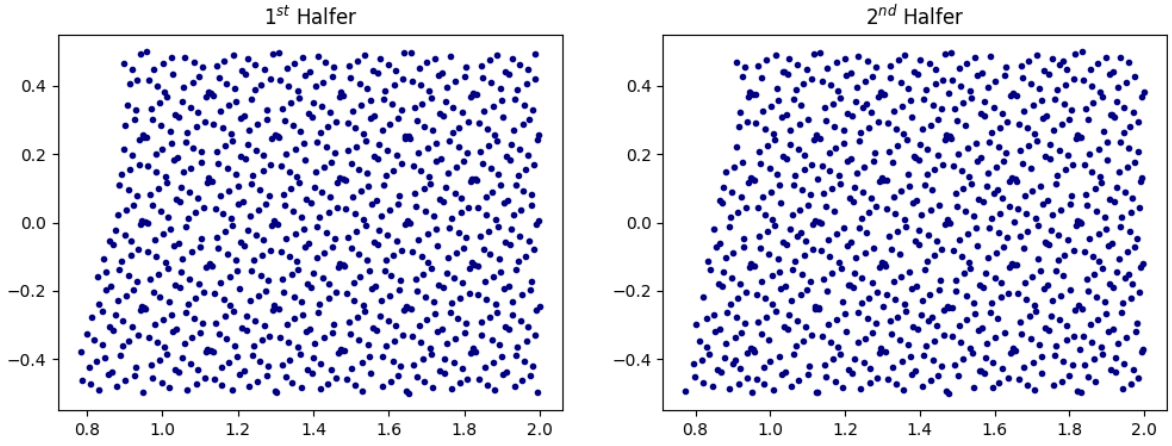

Figure 5.2: Dynamical plot displaying the 2 different subgrids produced from considering the first and second 1000 tracks of the full grid - 2 halves.

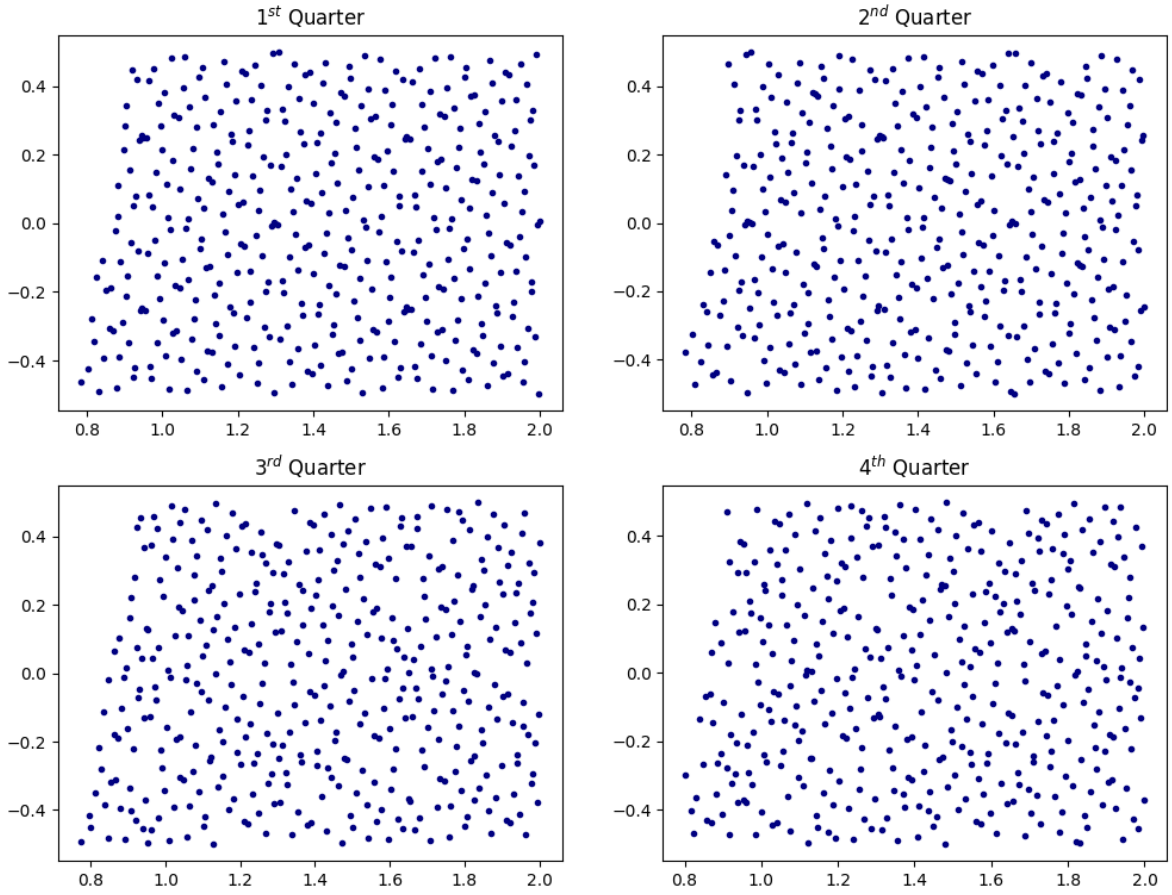

Figure 5.3: Dynamical plot displaying the 4 different subgrids produced from considering the first, second, third and forth 500 tracks of the full grid - 4 quarters.

$$f(x) = f_0 + \sum_{i=1}^{s} f_i(x_i) + \sum_{1 \le i \le j \le s} f_{i,j}(x_i, x_j) + \mathcal{O}^2(x_i, x_j). \tag{5.1}$$

This way, when projecting the sequence in each one of its n dimensions (in our case, when projecting the N points of the grid along M or $[Fe/H]$), the average distance between the points of the Sobol sequence can be approximated by the total range covered by the parameter divided by the number of tracks, $\Delta x_i/N$, providing a more uniform distribution for a given parameter when compared, for example, with a cartesian grid whose average distance between two consecutive values of the same parameter is given by $\Delta x_i/\sqrt{N}$.

Therefore, the aforementioned quasi-random distribution also allows a greater small-scale resolution of both parameters of the grid as seen in Fig. 5.4 (where the average step corresponds to the range of values divided by the total number of tracks). By changing both parameters simultaneously the grid will cover the lower dimensional parameter space more uniformly. However, for each projection at a lower dimension there is only one point in the grid to support the result (in contrast to a cartesian grid where each point of the projection has a larger number of points coming from the other dimensions supporting the estimation). While some debate still exists regarding whether the type of grid adopted for this exercise is optimal, recent tests by the team at the University of Aarhus do support this choice.

Concerning the specific case of the grid under consideration (presented in Fig. 5.1), we further investigated the two parameters considered in its construction, namely, mass and iron-content. Fig. 5.4 shows two histograms that uncover the average separation between two consecutive points of each parameter of the grid. The histogram on the left displays a very stable criteria, with the average value for the separation between two models of closest mass being $\Delta M = 0.00074 M_{\odot}$.

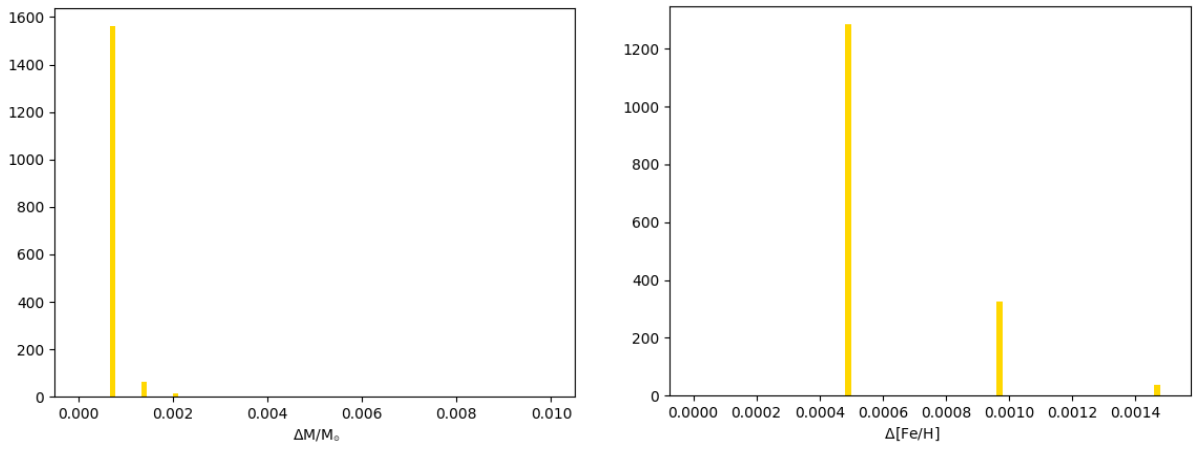

Figure 5.4: Histograms displaying the differences between consecutive values of mass in solar units (left) and iron-content (right).

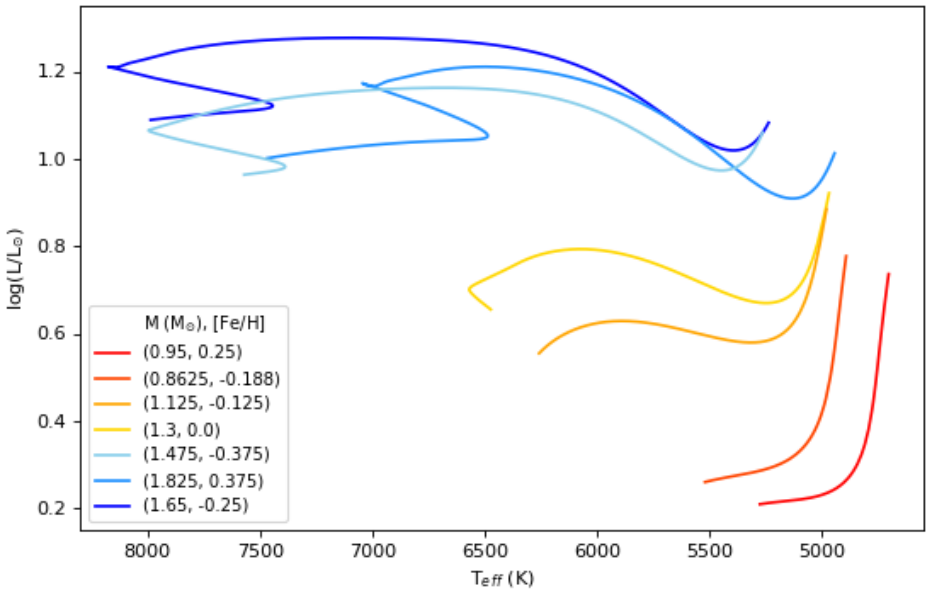

Figure 5.5: HR diagram of the subgiant phases of seven simulated tracks within various ranges of the different parameters. The legend presents the mass and iron-content, respectively, for each colored track.

The same can be seen in the histogram on the right, that reveals an average separation between two models of closest metallicity of $\Delta[Fe/H] = 0.00049$. The smaller bars in each histogram, representing larger differences, are mostly due to theoretical conventions and due to the quasi-randomness of the process. For the case of stellar mass, most of the counts to these bars can be explained by the lack of models on the less massive tracks that did not reach the subgiant phase in time, resulting in the larger differences between consecutive model masses in $\sim [0.75; 0.90]$ $M_{\odot}$. However, this argument is not applicable to metallicity. These conclusions are in agreement with the properties discussed before.

In addition to the distribution of tracks in the two-dimensional parameter space (M, $[Fe/H]$), one has also to consider the distribution of the models output along the evolution for each track. Fig. 5.5 shows the subgiant phase for the first 7 evolutionary tracks in the grid, illustrating that they cover a significant range of the parameter space.

Using these case-examples, we were able to verify the criteria used by the Aarhus team to define the output of models along the evolution. We considered three possibilities, namely: stellar age t, large separation frequency $\Delta\nu$, and frequency of maximum power $\nu_{\max}$. For each of these quantities, and for each track, we computed the difference between consecutive models and built the respective histograms. For the seven tracks indicated, we verified a prominent peak in the histograms for the stellar age, as illustrated in Fig. 5.6, while the histograms for both $\Delta\nu$ and $\nu_{\max}$ presented more irregular steps. From these, we concluded that the age was the parameter used by the grid modelers to define the output of the models along each evolution track.

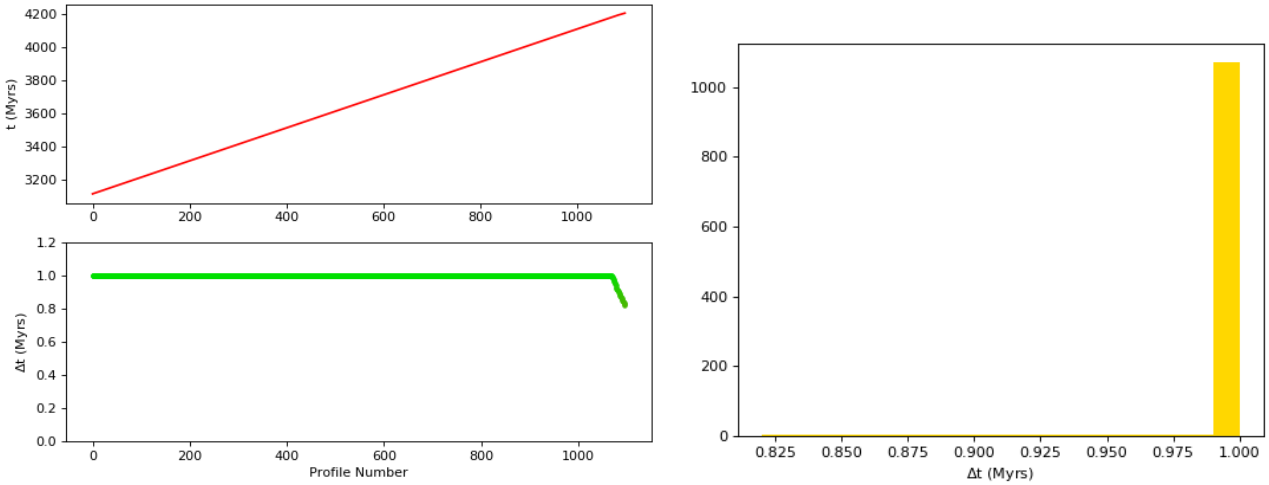

Figure 5.6: On the left, the age (t in Myrs) and the difference between consecutive ages (Δt) are plotted as a function of the respective profile for *track0001* in Fig. 5.5 ($M = 1.3$ M$_\odot$, $[Fe/H] = 0.0$). It is obvious that for most of the track, age is the main step that defines the construction of the grid. However, at the end of it (profiles $[1040; 1099]$), the track enters the RGB phase, and the time step loses the control to other parameter.
The histogram on the right shows the differences between consecutive ages, exhibiting a prominent peak in $[0.99; 1.00]$. This track has 1099 profiles, and it is configured between the interval of $[3111.9; 4207.1]$ Myrs. Taking this parameter as uniformly distributed, we get $\Delta t = 0.9966$ Myrs, which is in agreement with the conclusions of the plot on the right. Although not visible, there are some counts for Δt that fall off the peak over the represented x-axis. These are the ones corresponding to the end of the track, where other parameter then Δt take control of the simulation.

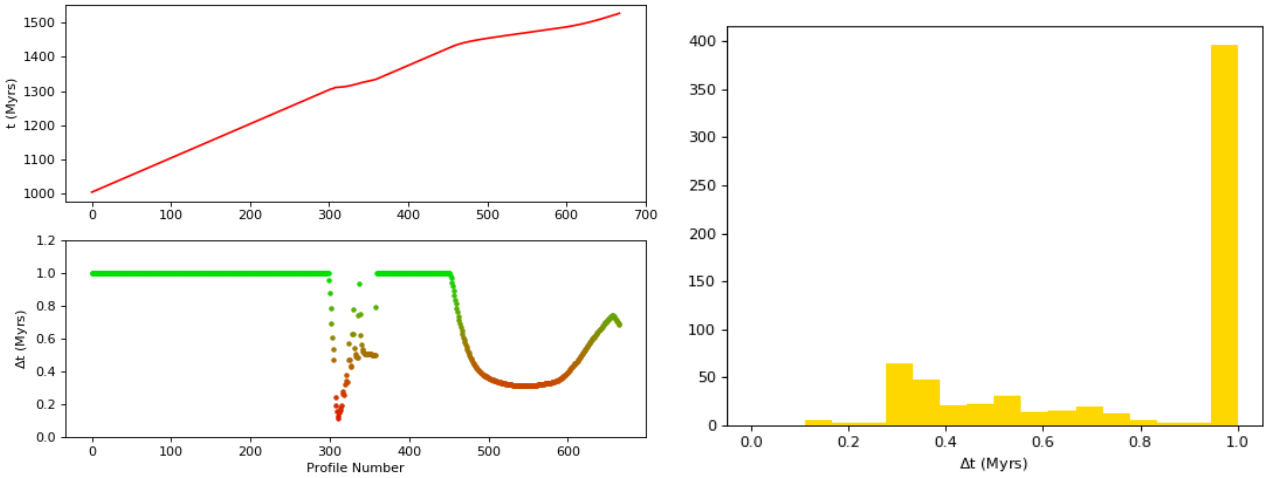

Figure 5.7: On the left, the age (t in Myrs) and the difference between consecutive ages (Δt) are plotted as a function of the respective profile for *track0002* in Fig. 5.5 ($M = 1.65$ M$_\odot$, $[Fe/H] = 0.25$). The histogram on the right shows the differences between consecutive ages, exhibiting a prominent peak within $[0.9445; 1.0000]$ (Myrs). Note that this track has 665 profiles, and is configured between the interval of ages $[1003.7; 1527.2]$ Myrs. If we take this parameter as uniformly distributed, we get $\Delta t = 0.7872$ Myrs.
Unlike *track0001* (in Fig. 5.6), Δt is much more unstable in *track0002*, as evidenced in the histogram by the large number of counts that fall off the main peak, that correspond to profiles $[292; 360]$ and $[461; 665]$. Identifying the profiles in the HR diagram, we can observe that profiles $[0; 360]$ are part of the main sequence of the star (with profiles $[292; 360]$ being part of the hook that characterizes more massive stars), while profiles $[461; 665]$ correspond to the RGB phase of the star. Thus, the main peak corresponds to models of the stable phase of the main sequence and of the subgiant phase.

However, exceptions to this output criteria do occur, as can be seen from the plots in Figs. 5.6 and 5.7. The conditions that limit the evolution tracks of our grid ($\Delta\nu = [70; 20]$ μHz) do not fully restrict the stars to the phase of subgiant, meaning that the tracks may also contain parts of other evolutionary phases. This is clearly shown in Fig. 5.5, where the track of a more massive star presents a stable main sequence section, the hook feature, the subgiant phase, and the beginning of the RGB. Inspecting Figs. 5.6 and 5.7 in light of the information from Fig. 5.5, one verifies that the main condition that controls the subgiant phase is indeed time. This simplifies the problem since the subgiant phase is our main stage of interest, and it follows our condition.

5.3 Definition of the Model Subgrids

The most significant problem to estimate stellar parameters through forward modelling based on a very dense grid of models is the computational space needed, since the number of models tends to increase with the power of the number of parameters. In addition, exploring a grid with an overwhelming number of models decreases the efficiency of the modelling, which may become a problem when analyzing the data of a large sample of stars, as it will be the case for the PLATO pipeline. Thus, the goal is to reduce the grid's density by first, building subgrids with fewer evolutionary tracks, and, then, by breaking down the number of models in each track, while still guaranteeing that the stellar properties estimated through forward modelling are within the science requirements of PLATO.

In order to test the grid and subgrids, we used a target sample consisting of the 6 simulated stars mentioned before (the *hares*), whose classical constraints, presented in Table 5.1, and asteroseismic frequencies, found in Table A.7.2, made available by a team at the University of Birmingham, shall be used during the optimization process implemented by the AIMS code. Due to the presence of mixed modes during the subgiant phase, that complicate the individual identification of modes,

	Luminosity ($L_\odot$)	$T_{\rm eff}$ (K)	$[Fe/H]$ (dex)
Brie	2.21 ± 0.07	5369 ± 85	0.19 ± 0.09
Cheddar	5.99 ± 0.19	5864 ± 85	-0.09 ± 0.09
Feta	6.74 ± 0.21	5674 ± 85	0.14 ± 0.09
Manchego	2.31 ± 0.07	5322 ± 85	0.31 ± 0.09
Parmesan	6.22 ± 0.19	5851 ± 85	-0.06 ± 0.09
Stilton	5.32 ± 0.16	5794 ± 85	-0.19 ± 0.09

Table 5.1: Classical constraints for each of the 6 simulated stars. Seismic constraints (oscillation frequency values) for the $\ell = 0$ considered in the results shown in this chapter can be found in A.7.2.

	Mass ($M_\odot$)	Radius ($R_\odot$)	Density (g/cm^3)	Age (Gyrs)
Brie	1.037 ± 0.008	1.722 ± 0.004	0.2858 ± 0.0002	10.8647 ± 0.2483
Cheddar	1.279 ± 0.022	2.420 ± 0.014	0.1271 ± 0.0004	3.9547 ± 0.1208
Feta	1.434 ± 0.018	2.725 ± 0.012	0.0998 ± 0.0003	2.9093 ± 0.0586
Manchego	1.042 ± 0.009	1.810 ± 0.005	0.2476 ± 0.0002	10.6201 ± 0.2565
Parmesan	1.329 ± 0.020	2.459 ± 0.020	0.1258 ± 0.0005	3.6386 ± 0.084
Stilton	1.219 ± 0.016	2.327 ± 0.011	0.1363 ± 0.0004	4.5829 ± 0.1245

Table 5.2: Statistical summary of the posterior probability distribution of the main parameters estimated for the 6 stars using the full grid.

	Mass ($M_\odot$)	Radius ($R_\odot$)	Density (g/cm^3)	Age (Gyrs)	X_i	Y_i	Z_i
Brie	1.0360	1.7219	0.2861	10.9866	0.6883	0.2852	0.02655
Cheddar	1.2565	2.4032	0.1276	4.0201	0.7236	0.2646	0.01183
Feta	1.4366	2.7272	0.0998	2.8892	0.7067	0.2744	0.01886
Manchego	1.0882	1.8365	0.2477	9.1537	0.6796	0.2902	0.03017
Parmesan	1.3018	2.4338	0.1273	3.8441	0.7132	0.2706	0.01616
Stilton	1.1583	2.2872	0.1365	4.5294	0.7022	0.2871	0.01077

Table 5.3: True parameters that characterize the 6 simulated stars. Note that density values were calculated from the true values of mass and radius considering the equation $\rho = \frac{3M}{4\pi R^3}$.

these tests only considered radial modes (with $\ell = 0$). Since there are no g-modes of degree $\ell = 0$, radial modes are simple p-modes, which are easier to identify, and whose frequencies vary comparatively slower with evolution.

As explained back in Chapter 4, the optimization process for the full grid and each of the subgrids takes the same 3 steps: the binary grid generation, the interpolation testing, and the stellar parameter characterization. In the same way, equal weights were given to each of the classical constraints and all of the seismic constraints (as considered in Eq. 4.7), and the surface corrections to the frequencies considered the same two-term function as Eq. 4.5.

Note that the true identity of these stars was concealed from the modeler until the very end of the study. The values of the stellar properties (mass, radius, age and density) were first derived from forward modelling based on the full grid. These results are displayed in Table 5.2, and are to be compared with the real values displayed in Table 5.3.

A more detailed study is made in Fig. 5.8, where we not only compare the true values of the stellar parameters with the ones estimated from applying the optimization process to the full grid

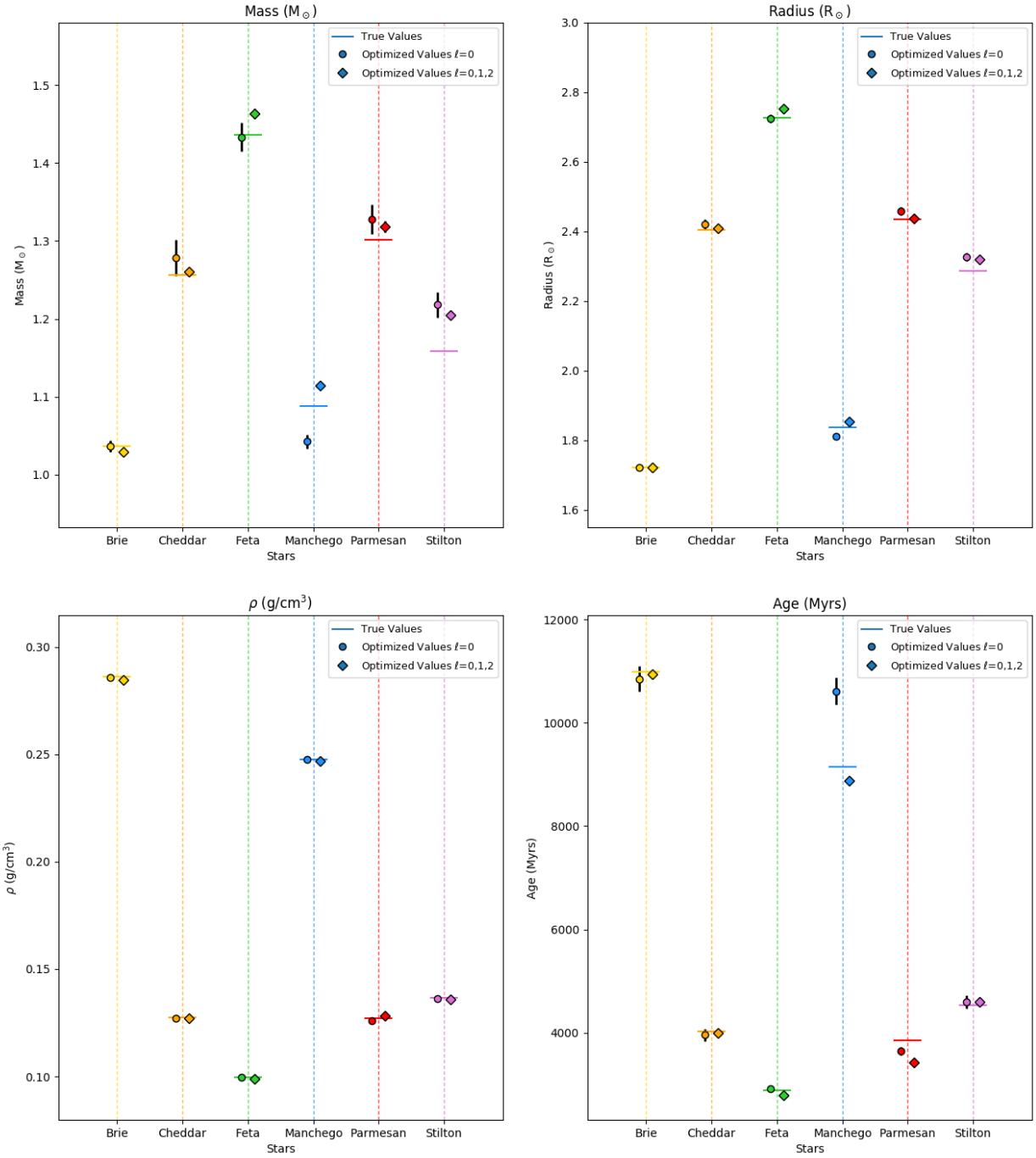

Figure 5.8: Comparison between the true values with the ones estimated from applying the optimization procedure to the full grid, considering the cases of ℓ=0 (only radial modes) and ℓ=0,1,2 (all modes) (with the respective uncertainties) for the stellar parameters (mass, radius, density and stellar age) of the 6 simulated stars.

for $\ell = 0$, but we also compare them for $\ell = 0, 1, 2$. Both optimizations for the full grid were implemented by B. Nsamba. For all targets, the mass and radius estimated from the $\ell = 0$ modes differ from the true values by less than the accuracy requirements set by PLATO, justifying the use of this procedure in the following tests. The agreement is specially good for Brie and Feta, while the estimations for the other stars are a little further away from the respective true values. For the most outlying cases, this means that considering $\ell = 0$ modes is not enough to retrieve the real values within the 1σ uncertainty. When we include the other mode degrees, $\ell = 0, 1, 2$, we end up with more accurate and precise estimations (with a mean value usually closer to the real parameter and smaller associated error bars), although, most of the times, the true value falls outside of the 1σ uncertainty which are often significantly smaller than in the case when only radial modes are used.

5.4 Results for Different Subgrids

As a first step towards finding the optimal subgrid, we cut the number of evolutionary tracks of the grid into different subsets. Having in mind that this process may strongly impact the results from the optimization process the smaller the tested subgrids became, we have made conservative, consecutive cuts and evaluated the outcome. The subgrids created by dividing the original grid in 2 are presented in Fig. 5.2, as the ones from dividing the same grid by 4 are presented in Fig. 5.3.

In both cases, the Sobol sequence method used to create the original grid ensures a similar distribution of the evolution tracks in the parameter space of each subgrid, thus we expect to arrive to similar conclusions for all of the subgrids in each of the figures. Interestingly, some subgrids from Fig. 5.2 and 5.3 seem to retain traces from the original pattern of the full grid. This can be partially explained by another property of the Sobol sequences. If we consider a sequence of models $(x_1, ..., x_n)$ and remove the first $m < n$ models in order to build a sub sequence $(x_1, ..., x_m)$ (where m is preferentially a multiple integer of n), this sub-sequence will be also a Sobol sequence. However, this is not guaranteed for the other sequences $(x_{m+1}, ..., x_{2m}), ..., (x_{(n-1)m+1}, ..., x_n)$. This interesting mathematical property explains the apparent patterns in the first subgrids in both figures. However, the presence of a pattern (or not) do not affect the results in any way.

Following the discussion above, the grid was first divided into 2 subgrids of 1000 evolution tracks each - 2 halves, - second, into 4 subgrids of 500 tracks each - 4 quarters, - and last, into 8 subgrids of 250 tracks each - 8 eighters, - with each subgroup containing the correspondent fraction of tracks of the total grid (i.e. with the 1^{st} quarter containing the evolutionary tracks from 1 to

500, the 2nd quarter containing them from 501 to 1000, and so forth).

The complete results of the study for $\ell = 0$ are presented in Tables A.7.3 to A.7.6. The plots depicting these results are shown in Fig. 5.9, displaying the relative deviation between the stellar properties estimated for each of the subgrids ($x_{i,\text{estimated}}$) and the true value ($x_{i,\text{true}}$), given by

$$\frac{\Delta x_i}{x_i} = \frac{x_{i,\text{estimated}} - x_{i,\text{true}}}{x_{i,\text{true}}} \tag{5.2}$$

for each one of the 6 simulated stars, with x_i representing mass, radius, density and stellar age.

In all cases, an increase scattering of the results is obvious when considering smaller subgrids, but, with the exception of the grid divided by 8, the science requirements of PLATO, namely, accuracies of 2-4% in the radius and of 10-15% in the mass of the stars, are satisfied. While stellar masses are kept within the desired accuracy limits for all stars, the radii of Cheddar, Manchego and Parmesan are at the limit when the grid is divided by 8. Now, the relative deviations estimated for the age can reach up to $\simeq 18.4\%$ (for Manchego). However, the 10% accuracy in age is a science requirement for solar-like stars in the main sequence, so the values that we obtained for our 6 simulated stars in the subgiant phase are acceptable, considering their evolved nature.

This way, for our subsequent analysis, we decided to adopt the 4 subgrids of 500 tracks each, whose results correspond to the 4 points overlapping each vertical dashed line in the plots. The maximum absolute deviations observed in each case for these subgrids are 4.99%, 1.73%, 1.05% and 16.21%, for mass, radius, density, and stellar age, respectively, all fulfilling the science requirements. Note that, although the estimations and relative deviations are different for different subgrids of identical size, the selection of the subgrid should be irrelevant, due to the way they were constructed from the original grid. That is confirmed by the fact that, for different stars, the results closest to those of the full grid are obtained with different quarters.

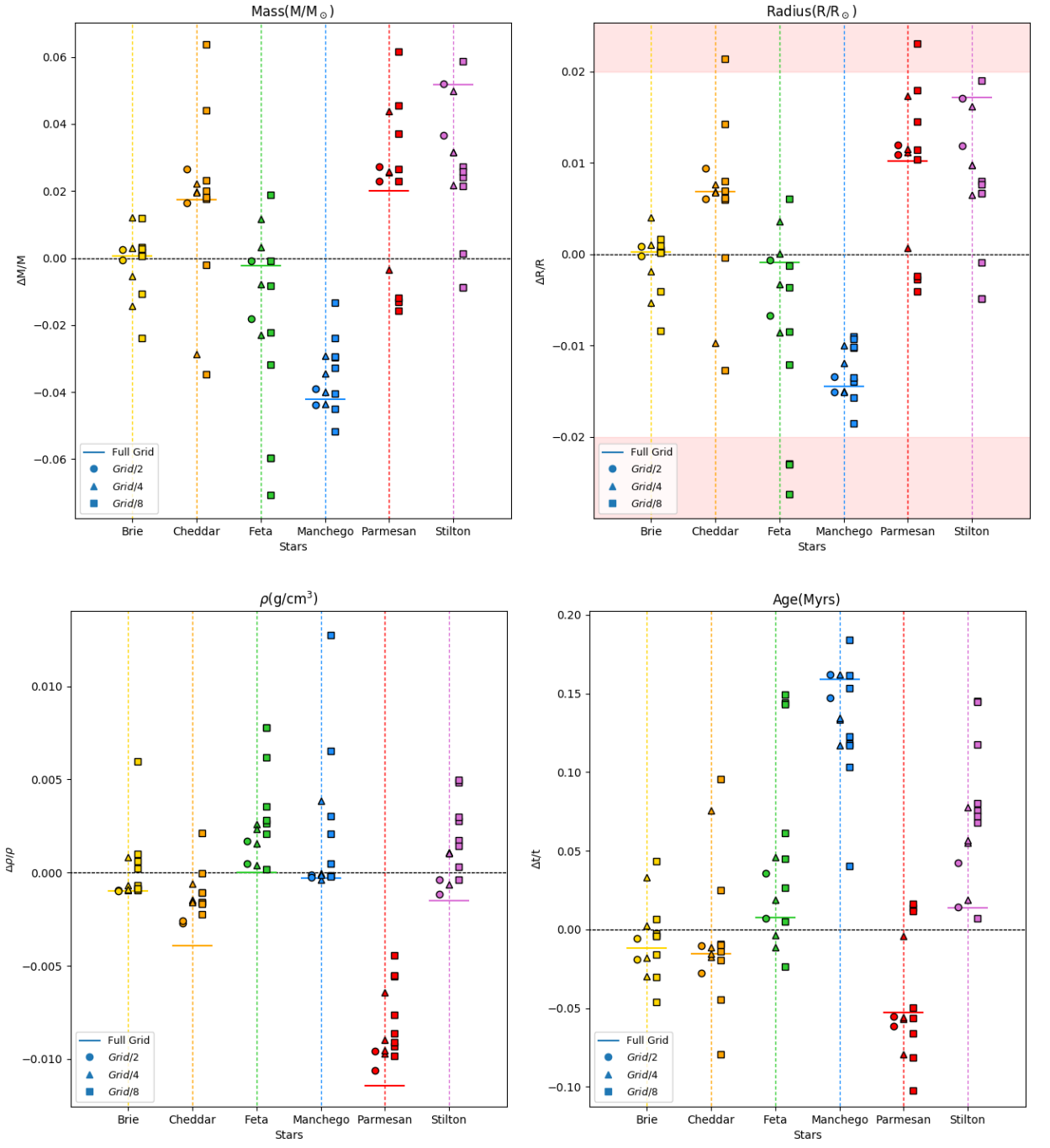

Figure 5.9: Relative deviations with respect to the true values of mass, radius, density and stellar age for each one of the 6 simulated stars, when considering subsections of the original grid covering different lengths of the parameter space $(M, [Fe/H])$. The results for the different subgrids, for each given star, are displayed vertically with different associated symbols, with circles showing the results for the half grids, triangles for the quarter grids, and squares for the eighter grids. Each full color line represents the relative deviation between the full grid and the theoretical results, for comparison.

5.5 Reducing the Number of Models Along Evolution

After dividing the original grid into 4 quarters of 500 tracks each, we wanted to test the impact of reducing the number of profiles in each evolutionary track, whose number can vary between 500 and 2000 models in the original grid.

The first tests were made by retaining one profile in each group of 2, 4 and 8 models (for now, by considering the first profile in each group only, t_1). It quickly became clear that a cut in the number of profiles would not affect the results as much as a cut in the parameter space as we verified that the scattering of the points for the 4 tested parameters barely increased when cutting the number of models by 2, 4 and 8. Thus, we continued cutting the number of profiles in each track by 16, 32, etc. with the results finally starting to spread out. It was necessary to consider every model in 100 for the subgrids to produce results whose relative deviation surpassed the accuracy threshold for the stellar properties (here considered as an average accuracy for the radius of 3%). These results are shown in Tables A.7.7 to A.7.10.

However, up until this, we only considered the first element of each subgroup of models, t_1. Tests with different groups of profiles would clearly vary the estimated results, and the point of break of the subgrids observed at $t/100$ would surely decrease.

Preliminary tests were carried out, starting with the subgrids that contained the greatest number of profiles, but fewer number of variations in the initial timestep. Thus, a subgrid whose number of profiles had been divided by 4 could start with the terms whose mod(index number) + 1 was t_1, t_2, t_3, t_4. These simulations were performed until the subgrids broke, which happened when the number of profiles was cut by 16, when the relative error of three subgrids approached the average limit imposed for the radius. The results for the least dense grids whose estimations fall reasonably well within the science requirements (and the 3% radius accuracy limit) ($t/8$) are presented in Fig. 5.11. For comparison, we also show the slightly better case of the grid with density ($t/4$) in Fig. 5.10. The results for the first tested subgrids to approach the limit of these requirements ($t/16$) are presented in Fig. 5.12 (only for the 3$^{\text{rd}}$ quarter).

Thus, we defined our final subgrids: 4 subgrids of 500 evolutionary tracks each, with one-eighth of the original number of models uniformly distributed throughout the evolutionary track. The results are listed in Table A.7.15 to A.7.18, and plots are presented in Fig. 5.11 showing the relative deviation between the estimated parameter of each subgrid and the respective theoretical value, for each of the 6 simulated stars. The maximum absolute deviations observed for each parameter was 7.24%, 2.56%, 2.77% and 25.03%, respectively, which are very acceptable.

We also note that one of our main problems, the time cost associated with the optimization of these grids, has been reduced. While the first and second steps of the procedure would take around 2 continuous hours, and the third would take around 1 day when considering the optimization procedure applied to the full grid, the procedure steps would take no longer then 20 minutes and 6 hours when applied to our final subgrids, nicely increasing the efficiency of the optimization.

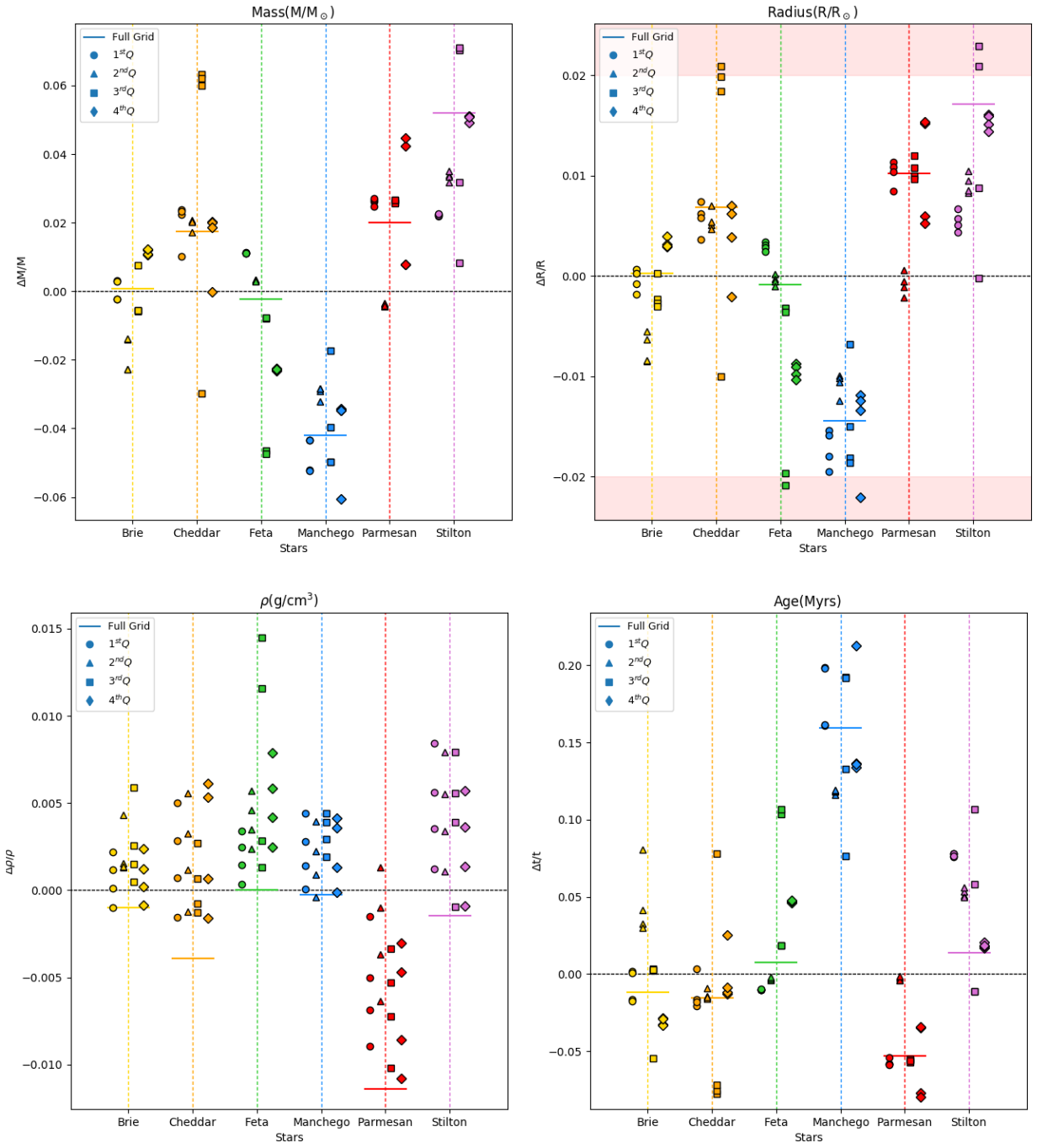

Figure 5.10: Relative deviations with respect to the true values of mass, radius, density and stellar age, respectively, for each one of the 6 simulated stars, when comparing the results for the 4 different subgrids, when the number of profiles of each track is reduced by 4, but considering all of the 4 possible starting points (t_1,t_2, ..., t_4). The results for the different quarters of each star are displayed vertically, with different associated symbols, with circles representing the 1st quarter, triangle the 2nd, squares the 3rd, and diamonds the 4th. Finally, the 4 points of each column represent the 4 possible starting points. Each full color line represents the relative deviation between the full grid and the theoretical results, for comparison.

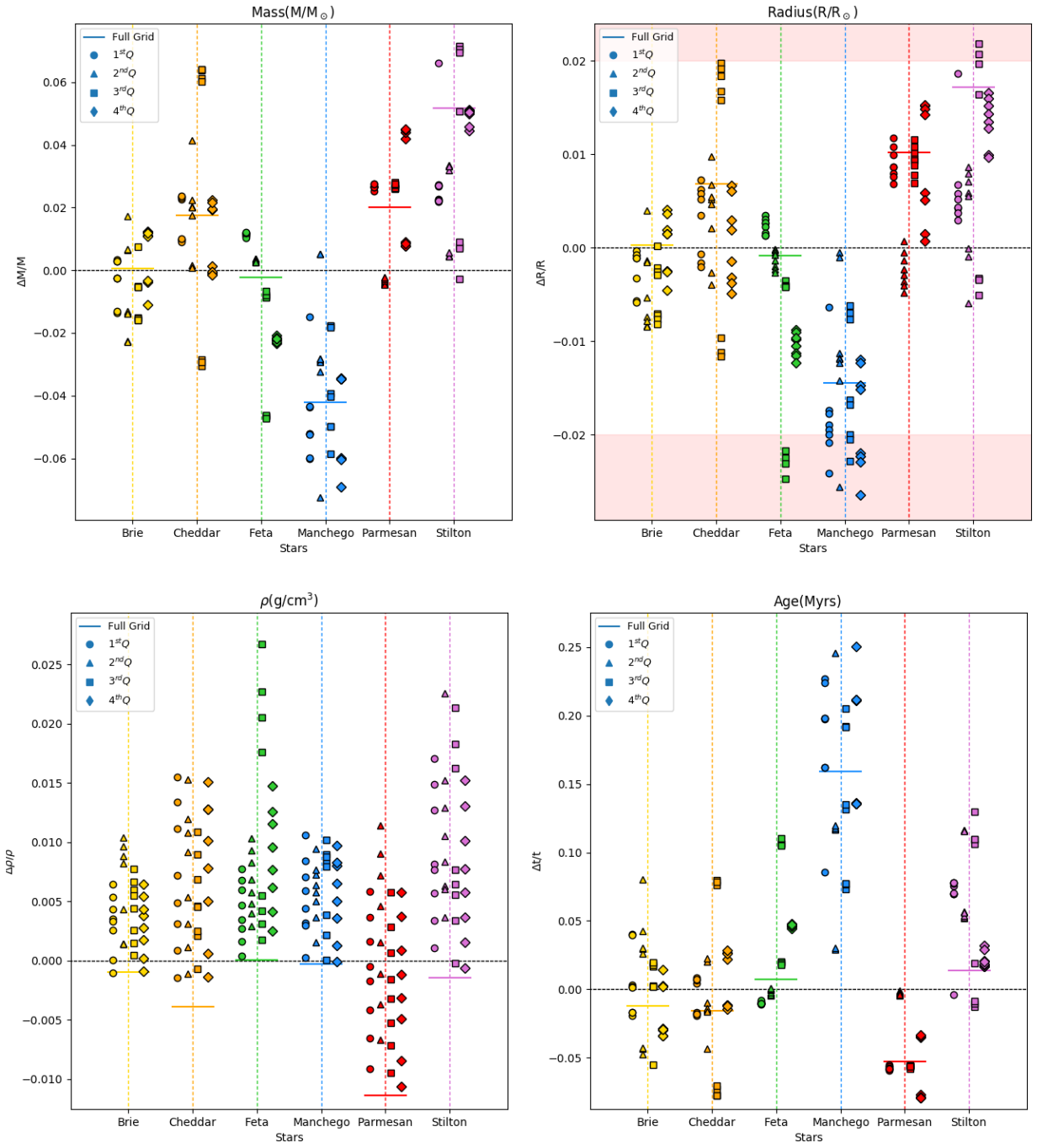

Figure 5.11: Relative deviations with respect to the true values of mass, radius, density and stellar age, respectively, for each one of the 6 simulated stars, when comparing the results for the 4 different subgrids, when the number of profiles of each track is reduced by 8, but considering all of the 8 possible starting points (t_1,t_2, ..., t_8). The results for the different quarters of each star are displayed vertically, with different associated symbols, with circles representing the 1st quarter, triangle the 2nd, squares the 3rd, and diamonds the 4th. Finally, the 8 points of each column represent the 8 possible starting points. Each full color line represents the relative deviation between the full grid and the theoretical results, for comparison.

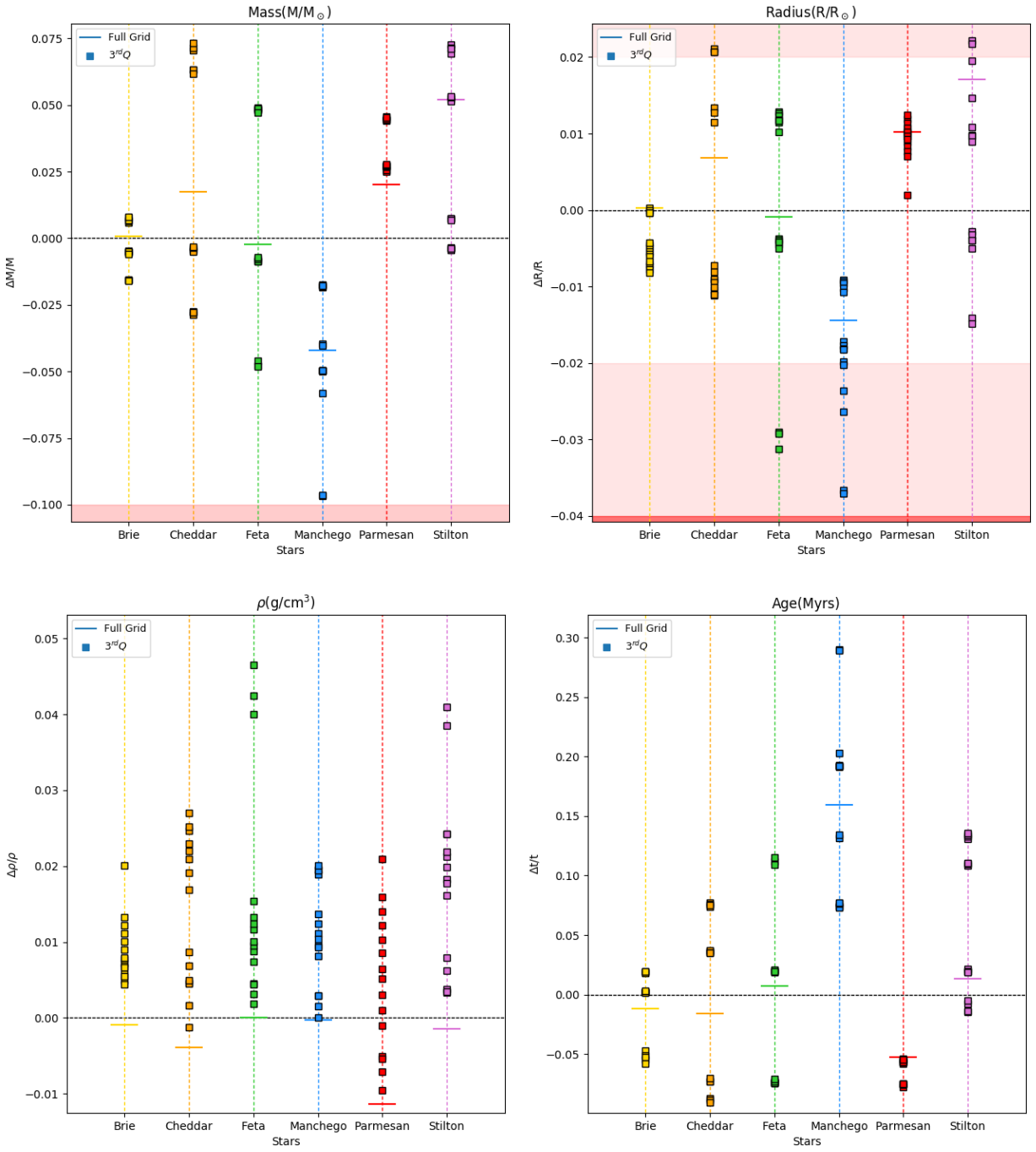

Figure 5.12: Relative deviations with respect to the true values of mass, radius, density and stellar age, respectively, for each one of the 6 simulated stars, when comparing the results for the 4 different subgrids, when the number of profiles of each track is reduced by 16, but considering all of the 16 possible starting points (t_1,t_2, ..., $t_1$6). The results here are only represented for the 3rd quarter, the first to be tested by the modeler, that immediately failed to meet the requirements, as shown by the points in the red regions. The 16 points of each column represent the 16 possible starting points. Each full color line represents the relative deviation between the full grid and the theoretical results, for comparison.

Chapter 6

Conclusions

From the beginning, we interacted with some programming codes that are very important in asteroseismic studies. We were able to reproduce the main parameters of the Sun using the AIMS optimization code, from a set of pre-computed grid models built with the MESA evolution code, a list of theoretical seismic frequencies obtained with the GYRE pulsation code, and a group of classical and seismic constraints obtained from observations. The conclusions we took from this first exercise were in agreement with the literature and most of them (especially the ones related with the AIMS optimization code) were of great importance for the ultimate goal of this thesis.

Concerning our main goal, we tested whether forward modelling based on a pre-computed grid of models and on the radial modes alone is successful in reproducing, within the desired accuracies, the true stellar parameters for each of the hares, and investigated the effects of reducing the density of the grid in conditions that still retrieved the stellar parameters (mass, radius, density and stellar age) of the 6 simulated stars within the accuracy set by the PLATO science requirements. For that, we considered a very dense grid produced by the Aarhus team with only 2 parameters, namely mass M and $[Fe/H]$. This grid was built to study the subgiant evolution phase of stars, during which the oscillation spectra of stars becomes particularly complex due to the appearance of mixed modes. In order to avoid that complexity, we only tested fits based on $l = 0$ modes.

The results for the full grid were presented in Table 5.2, and compared with the theoretical results in Table 5.3 through the plots in Fig. 5.8. Comparing the values of the stellar parameters estimated using the full grid with our optimization code with the theoretical ones, we find that the performance is quite good, with relative deviations no higher than 5.19%, 1.71%, 1.22% and 15.92% for mass, radius, density and age, respectively.

Following on this encouraging results, we started reducing the density of the original grid by

cutting the number of evolutionary tracks into smaller subgrids that cover uniformly the parameter space. This was possible due to the way the original grid was built, considering the properties of Sobol sequences. We cut the original grid in 2, 4 and 8 subgrids, and verified the accuracies on the stellar parameters were still within the science requirements (as shown in Tables A.7.3 to A.7.6). Considering all the 4 quarters with 500 tracks each, we obtained maximum deviations of 4.99%, 1.73%, 1.05% and 16.21% for mass, radius, density and age, respectively, fulfilling the PLATO scientific requirements.

For each of these quarters, we applied a second cut by reducing the number of profiles in each evolutionary track by 2, 4, 8... up until 100, when the science requirements applied to the subgrids were no longer satisfied. Such large value resulted from the fact that reducing the grid in the number of profiles in each track is much less efficient than reducing the number of tracks. The results of such work are presented in Tables A.7.7 to A.7.10. However, these subgrids only considered the first model in each subgroup of models. By testing all the possible time cuts combinations, we ended up defining our final subgrids with 500 evolutionary tracks, each with one-eighth of the original number of models uniformly distributed throughout the evolutionary track. For these, we obtained maximum deviations of 7.24%, 2.56%, 2.77% and 25.03% for mass, radius, density and age, respectively. The accuracies for all cases are presented in Tables A.7.15 to A.7.18. We have also minimized a major problem, by reducing the time cost of this optimization procedure to approximately one-fourth of the initial value.

With these new grids and only fitting $\ell = 0$ modes, it is possible to obtain the stellar parameters within the science requirements of the PLATO mission. Since these subgrids have a significantly reduced number of models when compared to the full grid, it is then possible to introduce new variables to the grid that will allow a more correct description of the physics of the observed stars (like the mixing length parameter and convective overshoot during the main sequence) without significantly increasing computational and storage cost. Future work can discuss the result of including these new parameters in the grid. Also, it would be interesting to observe the behavior of the subgrids when including all the mode degrees, $\ell = 0, 1, 2$. However, it is to be expected that achieving these results will be more challenging, as non-radial mode degrees include mixed modes, whose frequencies evolve very rapidly, hence making it more difficult to correctly interpolate between models.

This work has provided information that will be important for the building of a key section of the pipeline of the one of the most promising future missions in the context of the discovery and characterization of exoplanetary systems, namely the ESA mission's PLATO.

Bibliography

[1] M.S. Cunha, *Theory of Stellar Oscillations*, In: T.L. Campante, N. Santos, M. Monteiro (eds), *Asteroseismology and Exoplanets: Listening to the Stars and Searching for New Worlds*, Astrophysics and Space Science Proceedings, Springer, Vol 49 (2018)

[2] W.J. Chaplin, A. Miglio, *Asteroseismology of Solar-Type and Red-Giant Stars*, Annual Review of Astronomy and Astrophysics, Vol 51 (2013)

[3] T.L. Campante, M. Schofield, J.S. Kuszlewicz, et al., *The Asteroseismic Potential of TESS: Exoplanet-Host Stars*, The American Astronomical Society, Vol 830 (2016)

[4] H. Rauer, C. Aerts, J. Cabrera, and PLATO Team, *The PLATO 2.0 Mission*, Astronomische Nachrichten, Vol 337 (2016)

[5] H. Rauer, C. Catala, C. Aerts, and PLATO Team, *The PLATO 2.0 Mission*, Experimental Astrononomy, Vol 249 (2014)

[6] V.S. Aguirre, *Stellar Evolution and Modelling Stars*, In: T.L. Campante, N. Santos, M. Monteiro (eds), *Asteroseismology and Exoplanets: Listening to the Stars and Searching for New Worlds*, Astrophysics and Space Science Proceedings, Vol 49, Springer (2018)

[7] A.C. Phillips, *The Physics of Stars*, 2nd Edition, Wiley-VCH (1999)

[8] B. Paxton, L. Bildsten, *Modules for Experiments in Stellar Astrophysics (MESA)*, The Astrophysical Journal Supplement Series, Vol 192 (2011)

[9] J.P. Cox, R.T. Giuli, *Principles of Stellar Structure*, New York: Gordon and Breach (1968)

[10] A.A. Thoul, J.N. Bahcall, A. Loeb, *Element Diffusion in the Solar Interior*, Astrophysical Journal - Part 1, Vol 421 (1994)

[11] I. Iben, J. MacDonald, *The effects of diffusion due to gravity and due to composition gradients on the rate of hydrogen burning in a cooling degenerate dwarf. I - The case of a thick helium buffer layer*, Astrophysical Journal, Vol 296, 540-553 (1985)

[12] N. Grevesse, A. Sauval, *Standard Solar Composition*, Space Science Reviews, Vol 85 (1998)

[13] R.H. Cyburt, B.D. Fields, K.A. Olive, *Primordial Nucleosynthesis in Light of WMAP*, Physics Letters B, Vol 567, (2003)

[14] E. Böhm-Vitense, *Über die Wasserstoffkonvektionszone in Sternen verschiedener Effektivtemperaturen und Leuchtkräfte*, Zeitschrift für Astrophysik, Vol 46, 108 (1958)

[15] C. Aerts, J. Christensen-Dalsgaard, D.W. Kurtz, *Asteroseismology*, 1st Edition, Springer Netherlands (2010)

[16] P. G. Beck, *Asteroseismology of Red-Giant Stars: Mixed Modes, Differential Rotation, and Eccentric Binaries*, PhD Thesis, Arenberg Doctoral School of Science, Engineering & Technology, Faculty of Science, Department of Physics and Astronomy, KU Leuven, Belgium (2013)

[17] R.A. Garcia, J. Ballot, A. Eff-Darwich, R. Garrido, et al. *Detecting individual gravity modes in the Sun: Chimera or reality?*, International Astronomical Union, Vol 5, 345-346 (2009)

[18] M.S. Cunha, C. Aerts, J. Christensen-Dalsgaard, et al., *Asteroseismology and interferometry*, Astronomy & Astrophysics Review, Vol 14 (2007)

[19] R. H. D. Townsend, S. A. Teitler, *GYRE: an open-source stellar oscillation code based on a new Magnus Multiple Shooting scheme*, Royal Astronomical Society, Vol 435 (2013)

[20] R.P. Brent, *Algorithms for minimization without derivatives*, Prentice-Hall (1973)

[21] S. Hekker, *Asteroseismology of Red Giants and Galactic Archaeology.* In: T.L. Campante, N. Santos, M. Monteiro, *Asteroseismology and Exoplanets: Listening to the Stars and Searching for New Worlds.* Astrophysics and Space Science Proceedings, Springer, Vol 49 (2018)

[22] T.L. Campante, *An Introduction to Data Analysis in Asteroseismology.* In: T.L. Campante, N. Santos, M. Monteiro, *Asteroseismology and Exoplanets: Listening to the Stars and Searching for New Worlds*, Astrophysics and Space Science Proceedings, Springer, Vol 49 (2018)

[23] B. Nsamba, T.L. Campante, M.J.P.F.G. Monteiro, M.S. Cunha, et al. *Asteroseismic modelling of solar-type stars: internal systematics from input physics and surface correction methods*, Royal Astronomical Society, Vol 477 (2018)

[24] D.R. Reese, M.N. Lund, *AIMS: Asteroseismic Inference on a Massive Scale - Tutorial*, In: T.L. Campante, N. Santos, M. Monteiro (eds), *Asteroseismology and Exoplanets: Listening to the Stars and Searching for New Worlds*, Astrophysics and Space Science Proceedings, Springer, Vol 49 (2017)

[25] B.M. Rendle, G. Buldgen, A. Miglio, D. Reese, et al. *AIMS - A New Stellar Tool for Stellar Parameter Determinations Using Asteroseismic Constraints*, Monthly Notices of the Royal Astronomical Society, Vol 484 (2019)

[26] W.H. Ball, L. Gizon, *A New Correction of Stellar Oscillation Frequencies for Near-Surface Effects*, Astronomy & Astrophysics, Vol 568 (2014)

[27] V.S. Aguirre, M.N. Lund, H.M. Antia, W.H. Ball, et al. *Standing on the Shoulders of Dwarfs: the Kepler Asteroseismic LEGACY Sample II: Radii, Masses, and Ages*, The Astrophysical Journal, Vol 835 (2017)

[28] D.R. Reese, W.J. Chaplin, G.R. Davies, A. Miglio, et al., *SpaceInn Hare-and-Hounds Exercise: Estimation of Stellar Properties Using Space-Based Asteroseismic Data*, Astronomy & Astrophysics, Vol 592 (2016)

[29] J. Christensen-Dalsgaard, *ADIPLS - the Aarhus Adiabatic Oscillation Package*, Astrophysics and Space Science, Vol 316 (2008)

[30] S. Joe, F.Y. Kuo, *Constructing Sobol' sequences with better two-dimensional projections*, SIAM Journal on Scientific Computing, Vol 30 (2008)

Chapter 7

Appendix

7.1 Tables of Frequencies for the Sun

ℓ	n	ν	$\delta\nu$
0	16	2362.81	0.09
0	17	2496.34	0.09
0	18	2629.93	0.08
0	19	2764.41	0.10
0	20	2890.28	1.06
0	27	3850.83	1.42
0	21	3033.77	0.06
0	22	3168.50	0.06
0	23	3303.62	0.10
0	24	3439.12	0.18
0	25	3575.20	0.43
0	26	3710.28	1.06
0	27	3850.83	1.42
1	15	2291.98	0.04
1	16	2425.51	0.07

ℓ	n	ν	$\delta\nu$
1	17	2559.10	0.13
1	18	2693.48	0.09
1	19	2829.07	0.05
1	15	2291.98	0.04
1	16	2425.51	0.07
1	17	2559.10	0.13
1	18	2693.48	0.09
1	19	2828.25	0.07
1	20	2963.32	0.06
1	21	3098.09	0.07
1	22	3233.21	0.10
1	23	3368.69	0.11
1	24	3504.17	0.16
1	25	3640.74	0.26
1	26	3777.34	0.26

ℓ	n	ν	$\delta\nu$
1	27	3913.77	0.34
2	15	2352.13	0.18
2	16	2485.66	0.21
2	17	2619.55	0.14
2	18	2754.52	0.20
2	19	2889.69	0.14
2	20	3024.69	0.09
2	21	3159.80	0.10
2	22	3295.11	0.11
2	23	3430.60	0.31
2	24	3566.98	0.32
2	25	3703.44	0.31
2	26	3840.02	0.39
3	20	3082.18	0.47
3	21	3217.96	0.36

Table 7.1: Table of asteroseismic frequencies (used as seismic constraints) for the Sun.

7.2 Tables of Seismic Constraints for the 6 Simulated Stars

		Brie		Cheddar		Feta		Manchego		Parmesan		Stilton	
ℓ	n	ν	$\delta\nu$	ν	$\delta\nu$	ν	$\delta\nu$	ν	$\delta\nu$	ν	$\delta\nu$	ν	$\delta\nu$
0	10	-	-	466.03	0.31	-	-	-	-	-	-	483.37	0.26
0	11	-	-	506.89	0.17	449.02	0.12	-	-	503.66	0.18	525.63	0.14
0	12	829.44	0.06	547.12	0.12	484.73	0.08	770.99	0.05	544.43	0.12	566.47	0.10
0	13	889.66	0.04	586.98	0.10	519.73	0.07	826.84	0.04	583.71	0.09	607.83	0.09
0	14	949.90	0.04	627.28	0.09	555.60	0.06	883.05	0.03	623.93	0.08	649.87	0.08
0	15	1011.09	0.04	668.54	0.09	592.25	0.06	940.04	0.03	664.40	0.08	692.80	0.08
0	16	1072.39	0.04	709.94	0.10	628.55	0.06	996.98	0.03	705.63	0.09	735.25	0.09
0	17	1133.67	0.04	750.92	0.11	664.76	0.07	1053.99	0.04	746.78	0.10	777.88	0.11
0	18	1195.02	0.05	791.93	0.15	701.24	0.09	1111.11	0.04	787.51	0.12	820.46	0.15
0	19	1256.71	0.06	834.12	0.23	738.07	0.12	1168.71	0.05	828.75	0.18	863.54	0.27
0	20	1318.82	0.08	875.22	0.51	775.43	0.23	1226.59	0.07	870.18	0.34	908.21	0.69
0	21	1381.14	0.14	-	-	-	-	1226.59	0.07	-	-	-	-
0	22	1444.18	0.33	-	-	-	-	1342.71	0.27	-	-	-	-
1	6	-	-	555.27	0.08	543.49	0.04	-	-	519.01	0.11	574.85	0.07
1	7	-	-	577.58	0.06	570.17	0.04	-	-	550.04	0.08	597.04	0.06
1	8	785.64	0.07	603.97	0.07	590.41	0.04	745.93	0.05	575.01	0.07	624.68	0.06
1	9	818.61	0.05	632.89	0.06	614.16	0.05	793.46	0.03	601.79	0.06	655.56	0.06
1	10	863.93	0.04	659.49	0.06	642.23	0.04	826.02	0.02	629.46	0.06	683.02	0.06
1	11	918.99	0.03	691.28	0.07	661.15	0.04	860.82	0.03	655.64	0.06	715.30	0.07
1	12	975.30	0.03	722.56	0.07	687.90	0.06	912.08	0.03	689.28	0.07	747.18	0.06
1	13	1021.84	0.02	745.45	0.07	720.13	0.08	966.36	0.03	726.15	0.07	771.87	0.07
1	14	1051.42	0.03	776.98	0.10	744.87	0.07	1019.50	0.03	757.37	0.06	804.71	0.10
1	15	1103.92	0.03	815.11	0.15	763.49	0.14	1058.63	0.02	777.42	0.08	844.14	0.16
1	16	1162.70	0.04	853.36	0.26	796.96	0.33	1088.59	0.03	811.29	0.12	884.04	0.32
1	17	1222.64	0.04	887.72	0.40	-	-	1139.96	0.04	850.34	0.20	-	-
1	18	1283.28	0.05	-	-	-	-	1195.77	0.05	890.27	0.46	-	-
1	19	1343.74	0.08	-	-	-	-	1252.53	0.07	-	-	-	-
1	20	1401.53	0.14	-	-	-	-	1309.41	0.13	-	-	-	-
1	21	1442.82	0.19	-	-	-	-	1366.13	0.35	-	-	-	-
2	5	-	-	664.63	0.14	661.92	0.11	-	-	619.88	0.14	688.69	0.13
2	6	-	-	-	-	698.71	0.07	-	-	652.91	0.03	-	-
2	7	884.58	0.07	706.17	0.15	700.13	0.12	875.88	0.05	660.90	0.13	731.64	0.14
2	8	944.22	0.06	747.19	0.17	735.08	0.19	884.19	0.03	701.88	0.13	773.21	0.17

2	9	-	-	-	-	-	-	934.90	0.05	-	-	816.85	0.23
2	10	1006.23	0.06	788.47	0.22	772.89	0.35	991.53	0.05	743.44	0.15	859.30	0.39
2	11	1066.93	0.06	829.77	0.35	-	-	-	-	784.03	0.19	-	-
2	12	1127.86	0.06	-	-	-	-	1049.19	0.06	825.85	0.27	-	-
2	13	1176.91	0.02	-	-	-	-	1106.18	0.07	866.46	0.51	-	-
2	14	1190.59	0.07	-	-	-	-	1163.41	0.08	-	-	-	-
2	15	1251.63	0.09	-	-	-	-	1217.81	0.05	-	-	-	-
2	16	1313.35	0.12	-	-	-	-	1223.99	0.10	-	-	-	-
2	17	1375.46	0.20	-	-	-	-	1279.91	0.17	-	-	-	-

Table 7.2: Table of asteroseismic frequencies (used as seismic constraints) for the 6 simulated stars used in our project.

7.3 Results for Different Subgrids

(n, N, t, T)	Brie	Cheddar	Feta	Manchego	Parmesan	Stilton
$(1, 1, 1, 1)$	0.0007	0.0175	−0.0022	−0.0420	0.0201	0.0519
$(1, 2, 1, 1)$	0.0025	0.0265	−0.0009	−0.0438	0.0272	0.0367
$(2, 2, 1, 1)$	−0.0006	0.0164	−0.0180	−0.0390	0.0229	0.0521
$(1, 4, 1, 1)$	0.0031	0.0222	0.0117	−0.0435	0.0256	0.0218
$(2, 4, 1, 1)$	−0.0142	0.0199	0.0033	−0.0291	−0.0035	0.0317
$(3, 4, 1, 1)$	−0.0055	−0.0286	−0.0079	−0.0400	0.0259	0.0317
$(4, 4, 1, 1)$	**0.0121**	0.0197	−0.0228	−0.0345	0.0438	0.0499
$(1, 8, 1, 1)$	0.0018	0.0201	**0.0188**	**-0.0134**	**0.0617**	0.0240
$(2, 8, 1, 1)$	0.0032	0.0232	**-0.0706**	−0.0451	0.0266	0.0214
$(3, 8, 1, 1)$	0.0008	0.0177	−0.0596	−0.0297	−0.0130	**-0.0088**
$(4, 8, 1, 1)$	**-0.0239**	0.0441	−0.0008	−0.0238	0.0371	0.0272
$(5, 8, 1, 1)$	−0.0106	**0.0639**	−0.0084	**-0.0517**	0.0231	0.0258
$(6, 8, 1, 1)$	0.0029	**-0.0348**	−0.0319	−0.0404	**-0.0158**	0.0014
$(7, 8, 1, 1)$	0.0007	0.0182	−0.0598	−0.0293	−0.0119	−0.0087
$(8, 8, 1, 1)$	0.0120	−0.0021	−0.0222	−0.0328	0.0454	**0.0588**

Table 7.3: Relative deviations in mass obtained for each one of the 6 simulated stars, for $\ell = 0$, when considering subgrids of the original grid covering different lengths of the parameter space. Each row presents the obtained accuracies for the n^{th} subgrid of the full grid divided by N, and divided by T the number of profiles of each evolutionary track, starting with profile t. The values in bold of each column represent the maximum (positive and negative) deviations for each simulated star.

(n, N, t, T)	Brie	Cheddar	Feta	Manchego	Parmesan	Stilton
$(1, 1, 1, 1)$	0.0002	0.0069	−0.0009	−0.0144	0.0102	0.0171
$(1, 2, 1, 1)$	0.0008	0.0094	−0.0006	−0.0151	0.0119	0.0118
$(2, 2, 1, 1)$	−0.0002	0.0061	−0.0067	−0.0134	0.0109	0.0171
$(1, 4, 1, 1)$	0.0010	0.0076	0.0036	−0.015	0.0112	0.0065
$(2, 4, 1, 1)$	−0.0054	0.0069	0.0001	−0.0100	0.0007	0.0097
$(3, 4, 1, 1)$	−0.0019	−0.0097	−0.0033	−0.0151	0.0115	0.0097
$(4, 4, 1, 1)$	0.0040	0.0068	−0.0086	−0.0119	0.0173	0.0162
$(1, 8, 1, 1)$	0.0005	0.0070	**0.0060**	**-0.0090**	**0.0230**	0.0066
$(2, 8, 1, 1)$	**0.0004**	0.0080	**-0.0263**	−0.0157	0.0114	0.0066
$(3, 8, 1, 1)$	0.0002	0.0060	−0.023	−0.0103	−0.0028	**-0.0049**
$(4, 8, 1, 1)$	**-0.0084**	0.0143	−0.0013	−0.0093	0.0145	0.0080
$(5, 8, 1, 1)$	−0.0041	**0.0214**	−0.0036	**-0.0185**	0.0104	0.0077
$(6, 8, 1, 1)$	0.0010	**-0.0127**	−0.0121	−0.0139	**-0.0041**	−0.0009
$(7, 8, 1, 1)$	0.0002	0.0062	−0.023	−0.0101	−0.0024	−0.0049
$(8, 8, 1, 1)$	0.0017	−0.0004	−0.0085	−0.0135	0.0179	**0.0190**

Table 7.4: Relative deviations in radius obtained for each one of the 6 simulated stars, for $\ell = 0$, when considering subgrids of the original grid covering different lengths of the parameter space. Each row presents the obtained accuracies for the n^{th} subgrid of the full grid divided by N, and divided by T the number of profiles of each evolutionary track, starting with profile t. The values in bold of each column represent the maximum (positive and negative) deviations for each simulated star.

(n, N, t, T)	Brie	Cheddar	Feta	Manchego	Parmesan	Stilton
$(1, 1, 1, 1)$	**0.0011**	**-0.0024**	**0.0010**	0.0017	**-0.0122**	**-0.0000**
$(1, 2, 1, 1)$	0.0012	-0.0012	0.0015	0.0019	-0.0103	0.0011
$(2, 2, 1, 1)$	0.0011	-0.001	0.0027	0.0018	-0.0114	0.0003
$(1, 4, 1, 1)$	0.0012	0.0001	0.0014	0.0020	-0.0098	0.0025
$(2, 4, 1, 1)$	0.0029	0.0001	0.0036	**0.0016**	-0.0072	0.0026
$(3, 4, 1, 1)$	0.0014	0.0010	0.0026	0.0059	-0.0105	0.0025
$(4, 4, 1, 1)$	0.0012	-0.0000	0.0034	0.0019	-0.0103	0.0008
$(1, 8, 1, 1)$	0.0014	-0.0000	0.0012	**0.0148**	-0.0101	0.0042
$(2, 8, 1, 1)$	0.0031	-0.0000	0.0072	0.0025	-0.0094	0.0018
$(3, 8, 1, 1)$	0.0012	0.0005	**0.0088**	0.0018	-0.0063	0.0063
$(4, 8, 1, 1)$	0.0023	0.0015	0.0036	0.0051	-0.0084	0.0032
$(5, 8, 1, 1)$	0.0027	-0.0006	0.0031	0.0041	-0.0099	0.0029
$(6, 8, 1, 1)$	0.0012	**0.0037**	0.0046	0.0019	**-0.0052**	0.0045
$(7, 8, 1, 1)$	0.0013	0.0005	0.0088	0.0018	-0.0063	**0.0064**
$(8, 8, 1, 1)$	**0.0081**	-0.0001	0.0038	0.0086	-0.0106	0.0011

Table 7.5: Relative deviations in density obtained for each one of the 6 simulated stars, for $\ell = 0$, when considering subgrids of the original grid covering different lengths of the parameter space. Each row presents the obtained accuracies for the n^{th} subgrid of the full grid divided by N, and divided by T the number of profiles of each evolutionary track, starting with profile t. The values in bold of each column represent the maximum (positive and negative) deviations for each simulated star.

(n, N, t, T)	Brie	Cheddar	Feta	Manchego	Parmesan	Stilton
$(1, 1, 1, 1)$	-0.0119	-0.0156	0.0074	0.1592	-0.0529	0.0136
$(1, 2, 1, 1)$	-0.0191	-0.0277	0.0068	0.1621	-0.0614	0.0424
$(2, 2, 1, 1)$	-0.0055	-0.0103	0.0355	0.1471	-0.0552	0.0140
$(1, 4, 1, 1)$	-0.0180	-0.0172	-0.0112	0.1621	-0.0571	0.0775
$(2, 4, 1, 1)$	0.0332	-0.0154	-0.0037	0.1171	-0.0041	0.0550
$(3, 4, 1, 1)$	0.0025	0.0758	0.0186	0.1336	-0.0558	0.0568
$(4, 4, 1, 1)$	-0.0295	-0.0114	0.0460	0.1347	-0.0792	0.0189
$(1, 8, 1, 1)$	-0.0028	-0.0138	**-0.0238**	**0.0404**	**-0.1024**	0.0803
$(2, 8, 1, 1)$	-0.0301	-0.0195	**0.1495**	0.1614	-0.0564	0.0758
$(3, 8, 1, 1)$	-0.0044	-0.0093	0.1440	0.1179	0.0139	**0.1451**
$(4, 8, 1, 1)$	**0.0434**	-0.0446	0.0052	0.1032	-0.0660	0.0678
$(5, 8, 1, 1)$	0.0066	**-0.0794**	0.0266	**0.1841**	-0.0497	0.0718
$(6, 8, 1, 1)$	-0.0161	**0.0956**	0.0611	0.1532	**0.0164**	0.1178
$(7, 8, 1, 1)$	-0.0040	-0.0098	0.1434	0.1171	0.0116	0.1445
$(8, 8, 1, 1)$	**-0.046**	0.025	0.0452	0.1225	-0.0813	**0.0071**

Table 7.6: Relative deviations in stellar age obtained for each one of the 6 simulated stars, for $\ell = 0$, when considering subgrids of the original grid covering different lengths of the parameter space. Each row presents the obtained accuracies for the n^{th} subgrid of the full grid divided by N, and divided by T the number of profiles of each evolutionary track, starting with profile t. The values in bold of each column represent the maximum (positive and negative) deviations for each simulated star.

7.4 Results for Subgrids with Reduced Models Along Evolution

(n, N, t, T)	Brie	Cheddar	Feta	Manchego	Parmesan	Stilton
$(1, 4, 1, 1)$	0.0025	0.0047	0.0139	−0.0015	0.0054	−0.0286
$(1, 4, 1, 2)$	0.0023	0.0047	0.0129	−0.0013	0.0057	−0.0281
$(1, 4, 1, 4)$	−0.0030	−0.0073	0.0133	−0.0104	0.0059	−0.0279
$(1, 4, 1, 8)$	−0.0031	0.0062	0.0143	−0.0104	0.0054	−0.0279
$(1, 4, 1, 16)$	0.0025	−0.0078	0.0124	−0.0190	0.0066	−0.0278
$(1, 4, 1, 32)$	0.0025	−0.0056	0.0162	−0.0186	−0.0121	−0.0704
$(1, 4, 1, 64)$	0.0358	−0.0079	**-0.0729**	−0.0192	−0.0170	−0.0704
$(1, 4, 1, 100)$	−0.0509	−0.0087	−0.0320	0.0218	−0.0390	−0.0682
$(2, 4, 1, 1)$	−0.0149	0.0024	0.0055	0.0135	−0.0231	−0.0192
$(2, 4, 1, 2)$	−0.0137	0.0025	0.0057	0.0135	−0.0236	−0.0188
$(2, 4, 1, 4)$	−0.0148	0.0032	0.0056	0.0136	−0.0233	−0.0172
$(2, 4, 1, 8)$	−0.0150	0.0026	0.0055	−0.0321	−0.0233	−0.0445
$(2, 4, 1, 16)$	−0.0141	0.0251	0.0054	0.0221	−0.0233	−0.0181
$(2, 4, 1, 32)$	**-0.0627**	0.0254	0.0066	0.0221	−0.0479	0.0186
$(2, 4, 1, 64)$	−0.0323	0.0246	0.0023	**-0.0761**	−0.0504	−0.0416
$(2, 4, 1, 100)$	−0.0604	−0.0223	0.0378	0.0230	**0.0297**	−0.0738
$(3, 4, 1, 1)$	−0.0061	−0.0453	−0.0057	0.0021	0.0057	−0.0192
$(3, 4, 1, 2)$	−0.0065	−0.0455	−0.0060	0.0018	0.0067	−0.0193
$(3, 4, 1, 4)$	0.0069	−0.0464	−0.0057	0.0024	0.0064	0.0176
$(3, 4, 1, 8)$	−0.0063	**0.0431**	−0.0453	−0.0082	0.0059	0.0181
$(3, 4, 1, 16)$	0.0069	−0.0442	−0.0067	−0.0081	0.0068	−0.0528
$(3, 4, 1, 32)$	0.0072	0.0444	−0.0447	−0.0288	0.0069	−0.0706
$(3, 4, 1, 100)$	−0.0492	**-0.0593**	−0.0503	**0.0246**	**-0.0837**	**-0.1024**
$(4, 4, 1, 1)$	0.0114	0.0022	−0.0207	0.0079	0.0233	−0.0018
$(4, 4, 1, 2)$	0.0110	0.0025	−0.0208	0.0078	−0.0121	−0.0014
$(4, 4, 1, 4)$	0.0113	0.0028	−0.0210	0.0081	−0.0120	−0.0025
$(4, 4, 1, 8)$	0.0111	0.0023	−0.0210	0.0077	−0.0113	−0.0006
$(4, 4, 1, 16)$	−0.0117	0.0028	−0.0206	0.0080	−0.0115	−0.0014
$(4, 4, 1, 32)$	−0.0277	−0.0179	−0.0216	0.0080	−0.0106	**0.0339**
$(4, 4, 1, 64)$	−0.0250	0.0124	**0.0649**	−0.0740	0.0215	0.0168
$(4, 4, 1, 100)$	**0.1330**	0.0166	−0.0578	0.0117	−0.0094	−0.0359

Table 7.7: Relative deviations in mass obtained for each one of the 6 simulated stars, for $\ell = 0$, when considering the 4 different subgrids build from the original grid and reduced by T the number of profiles of each track, considering as the first starting point t_1. Each row presents the obtained accuracies for the n^{th} subgrid of the full grid divided by N, and divided by T the number of profiles of each evolutionary track, starting with profile t. The values in bold of each column represent the maximum (positive and negative) deviations for each simulated star.

(n, N, t, T)	Brie	Cheddar	Feta	Manchego	Parmesan	Stilton
$(1, 4, 1, 1)$	0.0008	0.0007	0.0045	−0.0006	0.0010	−0.0105
$(1, 4, 1, 2)$	0.0008	0.0008	0.0042	−0.0005	0.0011	−0.0103
$(1, 4, 1, 4)$	−0.0010	−0.0032	0.0043	−0.0036	0.0011	−0.0103
$(1, 4, 1, 8)$	−0.0021	−0.0009	0.0036	−0.0050	−0.0015	−0.0126
$(1, 4, 1, 16)$	0.0008	−0.0034	0.0038	−0.0066	0.0016	−0.0103
$(1, 4, 1, 32)$	0.0008	−0.0028	0.0047	−0.0064	−0.0056	−0.0253
$(1, 4, 1, 64)$	0.0106	−0.0039	**-0.0274**	−0.0067	−0.0073	−0.0255
$(1, 4, 1, 100)$	−0.0179	−0.0048	−0.0147	0.0067	−0.0160	−0.0246
$(2, 4, 1, 1)$	−0.0056	0.0000	0.0010	0.0045	−0.0094	−0.0073
$(2, 4, 1, 2)$	−0.0054	0.0001	0.0011	0.0045	−0.0095	−0.0072
$(2, 4, 1, 4)$	−0.0057	0.0002	0.0011	0.0046	−0.0095	−0.0066
$(2, 4, 1, 8)$	−0.0057	−0.0001	0.0008	−0.0114	−0.0094	−0.0167
$(2, 4, 1, 16)$	−0.0056	0.0076	0.0008	0.0075	−0.0095	−0.0069
$(2, 4, 1, 32)$	**-0.0220**	0.0075	0.0011	0.0075	−0.0179	0.0055
$(2, 4, 1, 64)$	−0.0113	0.0064	−0.0011	**-0.0269**	−0.0187	−0.0157
$(2, 4, 1, 100)$	−0.0212	−0.0101	0.0100	0.0074	**0.0083**	−0.0263
$(3, 4, 1, 1)$	−0.0021	−0.0164	−0.0024	−0.0007	0.0013	−0.0073
$(3, 4, 1, 2)$	−0.0023	−0.0165	−0.0025	−0.0007	0.0017	−0.0073
$(3, 4, 1, 4)$	0.0000	−0.0168	−0.0023	−0.0006	0.0017	0.0056
$(3, 4, 1, 8)$	−0.0033	0.0119	−0.0201	−0.0043	−0.0007	0.0037
$(3, 4, 1, 16)$	0.0000	−0.0158	−0.0028	−0.0028	0.0017	−0.0196
$(3, 4, 1, 32)$	0.0001	**0.0141**	−0.0171	−0.0104	0.0017	−0.0262
$(3, 4, 1, 64)$	−0.0083	0.0119	−0.0218	**0.0109**	0.0013	−0.0003
$(3, 4, 1, 100)$	−0.0175	**-0.0220**	−0.0236	0.0078	**-0.0309**	**-0.0372**
$(4, 4, 1, 1)$	0.0038	−0.0001	−0.0077	0.0026	0.0071	−0.0009
$(4, 4, 1, 2)$	0.0036	0.0001	−0.0077	0.0025	−0.0042	−0.0007
$(4, 4, 1, 4)$	0.0037	0.0002	−0.0079	0.0026	−0.0042	−0.0010
$(4, 4, 1, 8)$	0.0037	0.0000	−0.0078	0.0025	−0.0040	−0.0004
$(4, 4, 1, 16)$	−0.0041	0.0001	−0.0078	0.0026	−0.0041	−0.0007
$(4, 4, 1, 32)$	−0.0094	−0.0076	−0.0086	0.0026	−0.0041	**0.0111**
$(4, 4, 1, 64)$	−0.0085	0.0029	**0.0112**	−0.0267	0.0057	0.0050
$(4, 4, 1, 100)$	**0.3308**	0.0040	−0.0237	0.0032	−0.0044	−0.0148

Table 7.8: Relative deviations in radius obtained for each one of the 6 simulated stars, for $\ell = 0$, when considering the 4 different subgrids build from the original grid and reduced by T the number of profiles of each track, considering as the first starting point t_1. Each row presents the obtained accuracies for the n^{th} subgrid of the full grid divided by N, and divided by T the number of profiles of each evolutionary track, starting with profile t. The values in bold of each column represent the maximum (positive and negative) deviations for each simulated star.

(n, N, t, T)	Brie	Cheddar	Feta	Manchego	Parmesan	Stilton
$(1, 4, 1, 1)$	0.0000	0.0025	0.0004	0.0002	0.0025	0.0025
$(1, 4, 1, 2)$	0.0000	0.0025	**0.0003**	0.0002	0.0024	0.0026
$(1, 4, 1, 4)$	0.0000	0.0024	0.0003	0.0003	0.0025	0.0027
$(1, 4, 1, 8)$	0.0032	**0.0089**	0.0034	**0.0047**	**0.0099**	**0.0099**
$(1, 4, 1, 16)$	0.0000	0.0026	0.0010	0.0006	0.0020	0.0028
$(1, 4, 1, 32)$	0.0001	0.0028	0.0021	0.0006	0.0047	0.0039
$(1, 4, 1, 64)$	0.0037	0.0039	0.0078	0.0007	0.0048	0.0046
$(1, 4, 1, 100)$	0.0020	0.0057	0.0119	0.0015	0.0087	0.0041
$(2, 4, 1, 1)$	0.0018	0.0024	0.0026	−0.0001	0.0051	0.0026
$(2, 4, 1, 2)$	0.0026	0.0023	0.0026	−0.0001	0.0048	0.0027
$(2, 4, 1, 4)$	0.0023	0.0027	0.0024	−0.0001	0.0051	0.0025
$(2, 4, 1, 8)$	0.0021	0.0029	0.0030	0.0019	0.0049	0.0052
$(2, 4, 1, 16)$	0.0025	0.0022	0.0030	**-0.0007**	0.0051	0.0026
$(2, 4, 1, 32)$	0.0021	0.0027	0.0034	−0.0006	0.0050	0.0018
$(2, 4, 1, 64)$	0.0014	0.0053	0.0057	0.0027	0.0048	0.0050
$(2, 4, 1, 100)$	0.0020	0.0080	0.0073	0.0005	0.0044	0.0035
$(3, 4, 1, 1)$	0.0003	0.0034	0.0016	0.0041	0.0017	0.0025
$(3, 4, 1, 2)$	0.0003	0.0033	0.0014	0.0039	0.0015	0.0025
$(3, 4, 1, 4)$	0.0069	0.0032	0.0013	0.0042	0.0012	0.0005
$(3, 4, 1, 8)$	0.0036	0.0067	0.0146	0.0046	0.0082	0.0069
$(3, 4, 1, 16)$	0.0068	0.0027	0.0018	0.0004	0.0018	0.0052
$(3, 4, 1, 32)$	**0.0070**	**0.0014**	0.0059	0.0021	0.0019	0.0065
$(3, 4, 1, 64)$	0.0014	0.0038	0.0118	0.0001	0.0036	0.0018
$(3, 4, 1, 100)$	0.0026	0.0055	0.0204	0.0011	0.0065	0.0058
$(4, 4, 1, 1)$	0.0001	0.0023	0.0023	0.0002	0.0019	0.0009
$(4, 4, 1, 2)$	0.0001	0.0023	0.0022	0.0001	**0.0006**	0.0007
$(4, 4, 1, 4)$	0.0001	0.0023	0.0025	0.0002	0.0006	0.0006
$(4, 4, 1, 8)$	0.0001	0.0023	0.0025	0.0002	0.0006	0.0007
$(4, 4, 1, 16)$	0.0005	0.0025	0.0027	0.0002	0.0008	0.0007
$(4, 4, 1, 32)$	0.0003	0.0048	0.0041	0.0002	0.0015	**0.0002**
$(4, 4, 1, 64)$	0.0004	0.0036	**0.0298**	0.0043	0.0040	0.0016
$(4, 4, 1, 100)$	**-0.5193**	0.0047	0.0123	0.0022	0.0037	0.0081

Table 7.9: Relative deviations in density obtained for each one of the 6 simulated stars, for $\ell = 0$, when considering the 4 different subgrids build from the original grid and reduced by T the number of profiles of each track, considering as the first starting point t_1. Each row presents the obtained accuracies for the n^{th} subgrid of the full grid divided by N, and divided by T the number of profiles of each evolutionary track, starting with profile t. The values in bold of each column represent the maximum (positive and negative) deviations for each simulated star.

(n, N, t, T)	Brie	Cheddar	Feta	Manchego	Parmesan	Stilton
$(1, 4, 1, 1)$	-0.0061	-0.0017	-0.0184	0.0025	-0.0044	0.0630
$(1, 4, 1, 2)$	-0.0051	-0.0018	-0.0169	0.0020	-0.0047	0.0616
$(1, 4, 1, 4)$	0.0140	0.0194	-0.0174	0.0340	-0.0054	0.0615
$(1, 4, 1, 8)$	0.0133	-0.0039	-0.0185	0.0324	-0.0029	0.0626
$(1, 4, 1, 16)$	-0.0065	0.0203	-0.0162	0.0582	-0.0056	0.0618
$(1, 4, 1, 32)$	-0.0066	0.0149	-0.0237	0.0578	0.0262	0.1508
$(1, 4, 1, 64)$	-0.0829	0.0166	**0.1531**	0.0593	0.0327	0.1499
$(1, 4, 1, 100)$	0.1146	0.0179	0.0709	-0.0502	0.0762	0.1425
$(2, 4, 1, 1)$	0.0457	0.0002	-0.0110	-0.0364	0.0515	0.0408
$(2, 4, 1, 2)$	0.0380	0.0006	-0.0114	-0.0372	0.0524	0.0399
$(2, 4, 1, 4)$	0.0449	-0.0004	-0.0113	-0.0372	0.0517	0.0367
$(2, 4, 1, 8)$	0.0466	0.0000	-0.0108	0.0748	0.0516	0.0997
$(2, 4, 1, 16)$	0.0403	-0.0337	-0.0113	-0.0243	0.0507	0.0388
$(2, 4, 1, 32)$	**0.1531**	-0.0354	-0.0136	-0.0247	0.0925	-0.0273
$(2, 4, 1, 64)$	0.0472	-0.0375	-0.0037	**0.1893**	0.0920	0.0947
$(2, 4, 1, 100)$	0.1506	0.0445	**-0.0621**	**-0.0861**	**-0.0467**	0.1603
$(3, 4, 1, 1)$	0.0146	0.0929	0.0112	-0.0221	-0.0031	0.0426
$(3, 4, 1, 2)$	0.0156	0.0940	0.0117	-0.0205	-0.0047	0.0427
$(3, 4, 1, 4)$	-0.0431	0.0951	0.0108	-0.0227	-0.0042	-0.0247
$(3, 4, 1, 8)$	0.0150	-0.0592	0.0991	0.0280	-0.0026	-0.0247
$(3, 4, 1, 16)$	-0.0431	0.0910	0.0126	0.0282	-0.0055	0.1154
$(3, 4, 1, 32)$	-0.0439	**-0.0646**	0.0913	0.0787	-0.0072	0.1576
$(3, 4, 1, 64)$	-0.0235	0.0401	-0.0529	0.0331	0.0076	0.0007
$(3, 4, 1, 100)$	0.1035	**0.1193**	0.1274	-0.0737	**0.1692**	**0.2299**
$(4, 4, 1, 1)$	-0.0178	0.0043	0.0383	-0.0211	-0.0277	0.0052
$(4, 4, 1, 2)$	-0.0171	0.0035	0.0386	-0.0204	0.0192	0.0040
$(4, 4, 1, 4)$	-0.0169	0.0029	0.0388	-0.0218	0.0192	0.0069
$(4, 4, 1, 8)$	-0.0171	0.0041	0.0379	-0.0203	0.0179	0.0025
$(4, 4, 1, 16)$	0.0269	0.0028	0.0367	-0.0210	0.0179	0.0038
$(4, 4, 1, 32)$	0.0862	0.0399	0.0359	-0.0214	0.0164	**-0.0491**
$(4, 4, 1, 64)$	0.0737	-0.0191	-0.0580	0.1625	-0.0307	-0.0231
$(4, 4, 1, 100)$	**-0.5447**	-0.0318	0.1387	-0.0454	0.0107	0.0766

Table 7.10: Relative deviations in stellar age obtained for each one of the 6 simulated stars, for $\ell = 0$, when considering the 4 different subgrids build from the original grid and reduced by T the number of profiles of each track, considering as the first starting point t_1. Each row presents the obtained accuracies for the n^{th} subgrid of the full grid divided by N, and divided by T the number of profiles of each evolutionary track, starting with profile t. The values in bold of each column represent the maximum (positive and negative) deviations for each simulated star.

7.5 Results for the Subgrids with 1/4 of the Number of Models

(n, N, t, T)	Brie	Cheddar	Feta	Manchego	Parmesan	Stilton
$(1, 4, 1, 4)$	-0.0024	0.0101	0.0111	-0.0520	0.0261	0.0225
$(1, 4, 2, 4)$	0.0031	0.0239	0.0112	-0.0434	0.0267	0.0218
$(1, 4, 3, 4)$	0.0029	0.0224	**0.0113**	-0.0434	0.0271	0.0221
$(1, 4, 4, 4)$	-0.0024	0.0234	0.0111	-0.0523	0.0248	0.0227
$(2, 4, 1, 4)$	-0.0142	0.0207	0.0034	-0.0290	-0.0037	0.0338
$(2, 4, 2, 4)$	**-0.0228**	0.0173	0.0031	-0.0284	**-0.0045**	0.0334
$(2, 4, 3, 4)$	-0.0227	0.0202	0.0033	-0.0283	-0.0035	0.0319
$(2, 4, 4, 4)$	-0.0137	0.0204	0.0029	-0.0322	-0.0043	0.0350
$(3, 4, 1, 4)$	0.0076	**-0.0298**	-0.0078	-0.0397	0.0266	0.0704
$(3, 4, 2, 4)$	-0.0056	**0.0633**	-0.0076	**-0.0174**	0.0260	0.0317
$(3, 4, 3, 4)$	-0.0058	0.0622	-0.0465	-0.0498	0.0257	**0.0083**
$(3, 4, 4, 4)$	-0.0056	0.0600	**-0.0473**	-0.0498	0.0267	**0.0710**
$(4, 4, 1, 4)$	0.012	0.0203	-0.0231	-0.0343	0.0079	0.0490
$(4, 4, 2, 4)$	0.0107	0.0200	-0.0225	-0.0347	0.0079	0.0509
$(4, 4, 3, 4)$	0.0108	-0.0002	-0.0230	**-0.0606**	0.0424	0.0510
$(4, 4, 4, 4)$	**0.0122**	0.0185	-0.0227	-0.0347	**0.0446**	0.0508

Table 7.11: Relative deviations in mass obtained for each one of the 6 simulated stars, for $\ell = 0$, for the 4 final different subgrids with the number of profiles divided by 4, and considering all of the 4 possible starting points. Each row of the table presents the obtained accuracies for the n^{th} subgrid of the full grid divided by N, and divided by T the number of profiles of each evolutionary track, starting with profile t. The values in bold of each column represent the maximum (positive and negative) deviations for each simulated star.

(n, N, t, T)	Brie	Cheddar	Feta	Manchego	Parmesan	Stilton
$(1, 4, 1, 4)$	-0.0008	0.0036	**0.0034**	-0.0180	0.0114	0.0067
$(1, 4, 2, 4)$	0.0007	0.0074	0.0031	-0.0154	0.0108	0.0057
$(1, 4, 3, 4)$	0.0003	0.0062	0.0028	-0.0159	0.0104	0.0051
$(1, 4, 4, 4)$	-0.0018	0.0058	0.0024	-0.0195	0.0084	0.0043
$(2, 4, 1, 4)$	-0.0055	0.0070	0.0002	-0.0099	0.0006	0.0104
$(2, 4, 2, 4)$	**-0.0085**	0.0051	-0.0003	-0.0102	-0.0006	0.0095
$(2, 4, 3, 4)$	-0.0084	0.0054	-0.0006	-0.0106	-0.0011	0.0083
$(2, 4, 4, 4)$	-0.0063	0.0046	-0.0011	-0.0125	**-0.0022**	0.0085
$(3, 4, 1, 4)$	0.0002	**-0.0100**	-0.0032	-0.0150	0.0120	**0.0229**
$(3, 4, 2, 4)$	-0.0023	**0.0209**	-0.0036	**-0.0068**	0.0107	0.0088
$(3, 4, 3, 4)$	-0.0027	0.0198	-0.0197	-0.0182	0.0100	**-0.0003**
$(3, 4, 4, 4)$	-0.0030	0.0184	**-0.0209**	-0.0186	0.0097	0.0209
$(4, 4, 1, 4)$	**0.0040**	0.0070	-0.0087	-0.0118	0.0059	0.0161
$(4, 4, 2, 4)$	0.0032	0.0062	-0.0091	-0.0124	0.0052	0.0159
$(4, 4, 3, 4)$	0.0029	-0.0021	-0.0098	**-0.0221**	0.0152	0.0151
$(4, 4, 4, 4)$	0.0030	0.0038	-0.0104	-0.0134	**0.0154**	0.0144

Table 7.12: Relative deviations in radius obtained for each one of the 6 simulated stars, for $\ell = 0$, for the 4 final different subgrids with the number of profiles divided by 4, and considering all of the 4 possible starting points. Each row of the table presents the obtained accuracies for the n^{th} subgrid of the full grid divided by N, and divided by T the number of profiles of each evolutionary track, starting with profile t. The values in bold of each column represent the maximum (positive and negative) deviations for each simulated star.

(n, N, t, T)	Brie	Cheddar	Feta	Manchego	Parmesan	Stilton
$(1, 4, 1, 4)$	**-0.0010**	-0.0015	**0.0004**	0.0001	-0.0089	0.0012
$(1, 4, 2, 4)$	0.0001	0.0007	0.0014	0.0014	-0.0069	0.0035
$(1, 4, 3, 4)$	0.0012	0.0029	0.0025	0.0028	-0.0050	0.0056
$(1, 4, 4, 4)$	0.0022	0.0050	0.0034	**0.0044**	-0.0015	**0.0084**
$(2, 4, 1, 4)$	0.0013	-0.0012	0.0024	**-0.0004**	-0.0064	0.0011
$(2, 4, 2, 4)$	0.0015	0.0012	0.0035	0.0009	-0.0037	0.0034
$(2, 4, 3, 4)$	0.0014	0.0032	0.0046	0.0023	-0.0010	0.0055
$(2, 4, 4, 4)$	0.0043	0.0056	0.0057	0.0040	**0.0013**	0.0079
$(3, 4, 1, 4)$	**0.0059**	-0.0008	0.0013	0.0039	-0.0102	**-0.0009**
$(3, 4, 2, 4)$	0.0005	-0.0013	0.0029	0.0019	-0.0073	0.0039
$(3, 4, 3, 4)$	0.0015	0.0007	0.0116	0.0030	-0.0053	0.0079
$(3, 4, 4, 4)$	0.0026	0.0027	**0.0145**	**0.0044**	-0.0033	0.0056
$(4, 4, 1, 4)$	-0.0009	$-$**0.0016**	0.0025	-0.0001	**-0.0108**	**-0.0009**
$(4, 4, 2, 4)$	0.0002	0.0007	0.0042	0.0013	-0.0086	0.0014
$(4, 4, 3, 4)$	0.0012	0.0053	0.0058	0.0036	-0.0047	0.0036
$(4, 4, 4, 4)$	0.0024	**0.0061**	0.0079	0.0041	-0.0030	0.0057

Table 7.13: Relative deviations in density obtained for each one of the 6 simulated stars, for $\ell = 0$, for the 4 final different subgrids with the number of profiles divided by 4, and considering all of the 4 possible starting points. Each row of the table presents the obtained accuracies for the n^{th} subgrid of the full grid divided by N, and divided by T the number of profiles of each evolutionary track, starting with profile t. The values in bold of each column represent the maximum (positive and negative) deviations for each simulated star.

(n, N, t, T)	Brie	Cheddar	Feta	Manchego	Parmesan	Stilton
$(1, 4, 1, 4)$	0.0018	0.0035	−0.0102	0.1987	−0.0581	0.0760
$(1, 4, 2, 4)$	−0.0166	−0.0206	−0.0100	0.1611	−0.0582	0.0779
$(1, 4, 3, 4)$	−0.0173	−0.0165	**-0.0104**	0.1617	−0.0590	0.0779
$(1, 4, 4, 4)$	0.0008	−0.0180	−0.0095	0.1978	−0.0541	0.0764
$(2, 4, 1, 4)$	0.0325	−0.0160	−0.0040	0.1162	−0.0040	0.0508
$(2, 4, 2, 4)$	0.0413	−0.0094	−0.0026	0.1180	−0.0022	0.0533
$(2, 4, 3, 4)$	**0.0805**	−0.0145	−0.0030	0.1185	−0.0040	0.0559
$(2, 4, 4, 4)$	0.0299	−0.0148	−0.0017	0.1191	**-0.0015**	0.0497
$(3, 4, 1, 4)$	**-0.0545**	**0.0781**	0.0183	0.1329	−0.0570	**-0.0114**
$(3, 4, 2, 4)$	0.0025	**−0.0777**	0.0185	**0.0762**	−0.0554	0.0581
$(3, 4, 3, 4)$	0.0034	−0.0756	0.1038	0.1923	−0.0548	**0.1065**
$(3, 4, 4, 4)$	0.0030	−0.0715	**0.1068**	0.1917	−0.0561	**-0.0114**
$(4, 4, 1, 4)$	−0.0287	−0.0128	0.0464	0.1339	−0.0348	0.0206
$(4, 4, 2, 4)$	−0.0325	−0.0119	0.0462	0.1363	−0.0343	0.0171
$(4, 4, 3, 4)$	−0.0330	0.0254	0.0474	**0.2128**	−0.0771	0.0178
$(4, 4, 4, 4)$	−0.0290	−0.0084	0.0478	0.1361	**-0.0795**	0.0183

Table 7.14: Relative deviations in stellar age obtained for each one of the 6 simulated stars, for $\ell = 0$, for the 4 final different subgrids with the number of profiles divided by 4, and considering all of the 4 possible starting points. Each row of the table presents the obtained accuracies for the n^{th} subgrid of the full grid divided by N, and divided by T the number of profiles of each evolutionary track, starting with profile t. The values in bold of each column represent the maximum (positive and negative) deviations for each simulated star.

7.6 Results for the Subgrids with 1/8 of the Number of Models

(n, N, t, T)	Brie	Cheddar	Feta	Manchego	Parmesan	Stilton
$(1, 4, 0, 8)$	-0.0025	0.0097	0.0113	-0.0600	0.0269	0.0226
$(1, 4, 1, 8)$	-0.0025	0.0234	0.0112	-0.0149	0.0269	0.0220
$(1, 4, 2, 8)$	-0.0135	0.0227	0.0110	-0.0521	0.0266	0.0224
$(1, 4, 3, 8)$	-0.0131	0.0232	0.0118	-0.0521	0.0253	0.0221
$(1, 4, 4, 8)$	0.0033	0.0237	0.0117	-0.0524	0.0266	0.0663
$(1, 4, 5, 8)$	0.0030	0.0098	0.0103	-0.0437	0.0265	0.0268
$(1, 4, 6, 8)$	0.0029	0.0090	0.0118	-0.0433	0.0275	0.0273
$(1, 4, 7, 8)$	-0.0024	0.0100	**0.0121**	-0.0599	0.0275	0.0270
$(2, 4, 0, 8)$	-0.0136	0.0200	0.0029	**-0.0724**	-0.0038	0.0046
$(2, 4, 1, 8)$	-0.0225	0.0175	0.0037	**0.0053**	-0.0044	0.0045
$(2, 4, 2, 8)$	**-0.0228**	0.0203	0.0037	0.0051	-0.0043	0.0334
$(2, 4, 3, 8)$	0.0065	0.0200	0.0038	-0.0289	**-0.0045**	0.0336
$(2, 4, 4, 8)$	0.0066	0.0017	0.0032	-0.0292	-0.0033	0.0333
$(2, 4, 5, 8)$	**0.0172**	0.0008	0.0026	-0.0283	-0.0028	0.0319
$(2, 4, 6, 8)$	-0.0132	0.0414	0.0026	-0.0283	-0.0023	0.0332
$(2, 4, 7, 8)$	-0.0139	0.0224	0.0027	-0.0322	-0.0022	0.0056
$(3, 4, 0, 8)$	0.0076	-0.0285	-0.0083	-0.0176	0.0262	0.0508
$(3, 4, 1, 8)$	-0.005	**-0.0305**	-0.0086	-0.0177	0.0263	**-0.0027**
$(3, 4, 2, 8)$	-0.0053	-0.0293	-0.0078	-0.0181	0.0261	**0.0716**
$(3, 4, 3, 8)$	-0.0053	0.0637	-0.0068	-0.0394	0.0263	0.0705
$(3, 4, 4, 8)$	-0.0158	**0.0642**	-0.0469	-0.0403	0.0274	0.0695
$(3, 4, 5, 8)$	-0.0151	0.0641	-0.0464	-0.0586	0.0282	0.0075
$(3, 4, 6, 8)$	-0.0155	0.0612	-0.0462	-0.0497	0.0272	0.0090
$(3, 4, 7, 8)$	-0.0159	0.0601	**-0.0472**	-0.0497	0.0276	0.0070
$(4, 4, 0, 8)$	0.0123	0.0193	-0.0234	-0.0348	0.0077	0.0510
$(4, 4, 1, 8)$	0.0120	0.0196	-0.0224	-0.0344	0.0078	0.0513
$(4, 4, 2, 8)$	-0.0110	0.0014	-0.0228	-0.0602	0.0421	0.0510
$(4, 4, 3, 8)$	-0.0037	-0.0010	-0.0209	-0.0599	0.0440	0.0508
$(4, 4, 4, 8)$	-0.0032	-0.0005	-0.0215	-0.0603	0.0448	0.0500
$(4, 4, 5, 8)$	0.0110	-0.0014	-0.0219	-0.0691	**0.0451**	0.0504
$(4, 4, 6, 8)$	0.0108	0.0224	-0.0218	-0.0346	0.0091	0.0445
$(4, 4, 7, 8)$	0.0120	0.0217	-0.0218	-0.0345	0.0087	0.0459

Table 7.15: Relative deviations in mass obtained for each one of the 6 simulated stars, for $\ell = 0$, for the 4 final different subgrids with the number of profiles divided by 8, and considering all of the 8 possible starting points. Each row of the table presents the obtained accuracies for the n^{th} subgrid of the full grid divided by N, and divided by T the number of profiles of each evolutionary track, starting with profile t. The values in bold of each column represent the maximum (positive and negative) deviations for each simulated star.

(n, N, t, T)	Brie	Cheddar	Feta	Manchego	Parmesan	Stilton
$(1, 4, 0, 8)$	-0.0008	0.0035	**0.0035**	-0.0208	0.0117	0.0068
$(1, 4, 1, 8)$	-0.0011	0.0072	0.0031	-0.0064	0.0108	0.0058
$(1, 4, 2, 8)$	-0.0057	0.0062	0.0026	-0.0190	0.0099	0.0052
$(1, 4, 3, 8)$	-0.0059	0.0058	0.0026	-0.0194	0.0086	0.0042
$(1, 4, 4, 8)$	-0.0003	0.0052	0.0022	-0.0200	0.0086	0.0186
$(1, 4, 5, 8)$	-0.0008	-0.0007	0.0013	-0.0174	0.0079	0.0043
$(1, 4, 6, 8)$	-0.0011	-0.0017	0.0015	-0.0177	0.0076	0.0037
$(1, 4, 7, 8)$	-0.0032	-0.0020	0.0013	-0.0241	0.0069	0.0029
$(2, 4, 0, 8)$	-0.0053	0.0067	-0.0002	**-0.0256**	0.0007	-0.0001
$(2, 4, 1, 8)$	-0.0083	0.0052	-0.0003	**-0.0005**	-0.0005	-0.0009
$(2, 4, 2, 8)$	**-0.0084**	0.0055	-0.0005	-0.0010	-0.0014	0.0086
$(2, 4, 3, 8)$	-0.0013	0.0046	-0.0008	-0.0112	-0.0023	0.0079
$(2, 4, 4, 8)$	-0.0015	-0.0027	-0.0014	-0.0118	-0.0029	0.0071
$(2, 4, 5, 8)$	0.0040	-0.0039	-0.0020	-0.0119	-0.0036	0.0059
$(2, 4, 6, 8)$	-0.0074	0.0097	-0.0024	-0.0124	-0.004	0.0055
$(2, 4, 7, 8)$	-0.0079	0.0021	-0.0027	-0.0143	**-0.0048**	**-0.0059**
$(3, 4, 0, 8)$	0.0002	-0.0096	-0.0035	-0.0062	0.0116	0.0164
$(3, 4, 1, 8)$	-0.0021	-0.0112	-0.0040	-0.0070	0.0108	-0.0034
$(3, 4, 2, 8)$	-0.0026	**-0.0116**	-0.0041	-0.0077	0.0101	**0.0218**
$(3, 4, 3, 8)$	-0.0029	**0.0197**	-0.0042	-0.0163	0.0095	0.0207
$(3, 4, 4, 8)$	-0.0071	0.0192	-0.0217	-0.0168	0.0093	0.0197
$(3, 4, 5, 8)$	-0.0072	0.0184	-0.0225	-0.0228	0.0088	-0.0033
$(3, 4, 6, 8)$	-0.0077	0.0167	-0.0231	-0.0200	0.0078	-0.0034
$(3, 4, 7, 8)$	-0.0082	0.0157	**-0.0247**	-0.0205	0.0069	-0.0051
$(4, 4, 0, 8)$	**0.0041**	0.0066	-0.0088	-0.0120	0.0059	0.0166
$(4, 4, 1, 8)$	0.0036	0.0061	-0.0090	-0.0123	0.0051	0.0159
$(4, 4, 2, 8)$	-0.0046	-0.0015	-0.0098	-0.0220	**0.0152**	0.0151
$(4, 4, 3, 8)$	-0.0025	-0.0032	-0.0097	-0.0223	0.0152	0.0144
$(4, 4, 4, 8)$	-0.0026	-0.0037	-0.0105	-0.0230	0.0148	0.0134
$(4, 4, 5, 8)$	0.0019	-0.0049	-0.0113	-0.0265	0.0142	0.0128
$(4, 4, 6, 8)$	0.0015	0.0029	-0.0116	-0.0147	0.0015	0.0099
$(4, 4, 7, 8)$	0.0015	0.0019	-0.0123	-0.0151	0.0007	0.0096

Table 7.16: Relative deviations in radius obtained for each one of the 6 simulated stars, for $\ell = 0$, for the 4 final different subgrids with the number of profiles divided by 8, and considering all of the 8 possible starting points. Each row of the table presents the obtained accuracies for the n^{th} subgrid of the full grid divided by N, and divided by T the number of profiles of each evolutionary track, starting with profile t. The values in bold of each column represent the maximum (positive and negative) deviations for each simulated star.

(n, N, t, T)	Brie	Cheddar	Feta	Manchego	Parmesan	Stilton
$(1, 4, 0, 8)$	**0.0011**	**0.0001**	**0.0014**	0.0023	−0.0100	0.0025
$(1, 4, 1, 8)$	0.0022	0.0024	0.0026	0.0052	−0.0073	0.0048
$(1, 4, 2, 8)$	0.0047	0.0047	0.0037	0.0050	−0.0049	0.0071
$(1, 4, 3, 8)$	0.0056	0.0065	0.0044	0.0064	−0.0025	0.0096
$(1, 4, 4, 8)$	0.0054	0.0088	0.0057	0.0079	−0.0013	0.0092
$(1, 4, 5, 8)$	0.0064	0.0127	0.0069	0.0091	0.0008	0.0142
$(1, 4, 6, 8)$	0.0074	0.0149	0.0078	0.0104	0.0028	0.0164
$(1, 4, 7, 8)$	0.0085	**0.0171**	0.0087	**0.0126**	0.0051	0.0186
$(2, 4, 0, 8)$	0.0035	0.0005	0.0039	0.0036	−0.0075	0.0051
$(2, 4, 1, 8)$	0.0035	0.0027	0.005	0.0078	−0.0045	0.0078
$(2, 4, 2, 8)$	0.0035	0.0047	0.0058	0.0093	−0.0019	0.0075
$(2, 4, 3, 8)$	0.0117	0.0069	0.0068	0.0057	0.0007	0.0098
$(2, 4, 4, 8)$	**0.0125**	0.0108	0.0079	0.0071	0.0038	0.0120
$(2, 4, 5, 8)$	0.0064	0.0135	0.0093	0.0084	0.0064	0.0144
$(2, 4, 6, 8)$	0.0103	0.0124	0.0103	0.0097	0.0082	0.0167
$(2, 4, 7, 8)$	0.0109	0.0169	0.0114	0.0114	**0.0106**	**0.0241**
$(3, 4, 0, 8)$	0.0081	0.0009	0.0027	0.0020	−0.0103	0.0012
$(3, 4, 1, 8)$	0.0026	0.0036	0.0041	0.0042	−0.0079	0.0079
$(3, 4, 2, 8)$	0.0036	0.0061	0.0052	0.0059	−0.0061	0.0049
$(3, 4, 3, 8)$	0.0047	0.0041	0.0065	0.0103	−0.0040	0.007
$(3, 4, 4, 8)$	0.0065	0.0061	0.0186	0.0110	−0.0023	0.0092
$(3, 4, 5, 8)$	0.0076	0.0084	0.0215	0.0099	−0.0001	0.0177
$(3, 4, 6, 8)$	0.0087	0.0105	0.0237	0.0108	0.0020	0.0198
$(3, 4, 7, 8)$	0.0099	0.0124	**0.0277**	0.0122	0.0050	0.0228
$(4, 4, 0, 8)$	0.0012	0.0002	0.0035	**0.0019**	**-0.0114**	**0.0008**
$(4, 4, 1, 8)$	0.0023	0.0022	0.0051	0.0033	−0.0092	0.003
$(4, 4, 2, 8)$	0.0038	0.0066	0.0071	0.0056	−0.0057	0.0051
$(4, 4, 3, 8)$	0.0049	0.0094	0.0087	0.007	−0.0039	0.0072
$(4, 4, 4, 8)$	0.0059	0.0117	0.0106	0.0085	−0.0020	0.0092
$(4, 4, 5, 8)$	0.0065	0.0143	0.0125	0.0100	0.0001	0.0116
$(4, 4, 6, 8)$	0.0075	0.0144	0.0136	0.0103	0.0030	0.0145
$(4, 4, 7, 8)$	0.0086	0.0167	0.0157	0.0117	0.0050	0.0167

Table 7.17: Relative deviations in density obtained for each one of the 6 simulated stars, for $\ell = 0$, for the 4 final different subgrids with the number of profiles divided by 8, and considering all of the 8 possible starting points. Each row of the table presents the obtained accuracies for the n^{th} subgrid of the full grid divided by N, and divided by T the number of profiles of each evolutionary track, starting with profile t. The values in bold of each column represent the maximum (positive and negative) deviations for each simulated star.

(n, N, t, T)	Brie	Cheddar	Feta	Manchego	Parmesan	Stilton
$(1, 4, 1, 8)$	0.0029	0.0042	−0.0105	0.2269	−0.0588	0.0755
$(1, 4, 2, 8)$	0.0021	−0.0190	−0.0100	0.0857	−0.0590	0.0777
$(1, 4, 3, 8)$	0.0406	−0.0170	−0.0092	0.1983	−0.0578	0.0771
$(1, 4, 4, 8)$	0.0395	−0.0181	**-0.0110**	0.1977	−0.0551	0.0780
$(1, 4, 5, 8)$	−0.0191	−0.0183	−0.0106	0.1983	−0.0566	−0.0040
$(1, 4, 6, 8)$	−0.0171	0.0065	−0.0081	0.1620	−0.0564	0.0698
$(1, 4, 7, 8)$	−0.0167	0.0084	−0.0103	0.1623	−0.0578	0.0695
$(1, 4, 0, 8)$	0.0014	0.0074	−0.0106	0.2243	−0.0579	0.0701
$(2, 4, 1, 8)$	0.0297	−0.0146	−0.0027	0.2460	−0.0044	0.1165
$(2, 4, 2, 8)$	0.0427	−0.0099	−0.0043	**0.0289**	−0.0034	0.1162
$(2, 4, 3, 8)$	**0.0802**	−0.0150	−0.0041	0.0300	−0.0023	0.0522
$(2, 4, 4, 8)$	−0.0437	−0.0137	−0.0039	0.1168	**-0.0012**	0.0528
$(2, 4, 5, 8)$	−0.0429	0.0202	−0.0019	0.1169	−0.0024	0.0540
$(2, 4, 6, 8)$	−0.0475	0.0225	−0.0002	0.1178	−0.0029	0.0565
$(2, 4, 7, 8)$	0.0263	−0.0433	0.0002	0.1180	−0.0042	0.0560
$(2, 4, 0, 8)$	0.0302	−0.0164	0.0008	0.1196	−0.0039	0.1154
$(3, 4, 1, 8)$	**-0.0551**	0.0762	0.0195	0.0731	−0.0559	0.0192
$(3, 4, 2, 8)$	0.0018	**0.0798**	0.0203	0.0768	−0.0561	**0.1301**
$(3, 4, 3, 8)$	0.0023	0.0784	0.0191	0.0772	−0.0555	**-0.0127**
$(3, 4, 4, 8)$	0.0018	−0.0774	0.0177	0.1313	−0.0555	−0.0102
$(3, 4, 5, 8)$	0.0194	**-0.0775**	0.1062	0.1352	−0.0570	−0.0088
$(3, 4, 6, 8)$	0.0167	−0.0773	0.1064	0.2049	−0.0579	0.1090
$(3, 4, 7, 8)$	0.0180	−0.0727	0.1053	0.1922	−0.0558	0.1060
$(3, 4, 0, 8)$	0.0198	−0.0706	**0.1103**	0.1916	−0.0561	0.1100
$(4, 4, 1, 8)$	−0.0296	−0.0114	0.0465	0.1363	−0.0351	0.0166
$(4, 4, 2, 8)$	−0.0287	−0.0114	0.0457	0.1359	−0.0344	0.0165
$(4, 4, 3, 8)$	0.0145	0.0223	0.0468	0.2116	−0.0768	0.0176
$(4, 4, 4, 8)$	0.0028	0.027	0.0443	0.2113	−0.0790	0.0184
$(4, 4, 5, 8)$	0.0017	0.0264	0.0464	0.2117	**-0.0796**	0.0208
$(4, 4, 6, 8)$	−0.0341	0.0286	0.0479	**0.2503**	−0.0791	0.0203
$(4, 4, 7, 8)$	−0.0338	−0.0147	0.0464	0.1359	−0.0343	0.0320
$(4, 4, 0, 8)$	−0.0291	−0.0123	0.0476	0.1356	−0.0334	0.0288

Table 7.18: Relative deviations in stellar age obtained for each one of the 6 simulated stars, for $\ell = 0$, for the 4 final different subgrids with the number of profiles divided by 8, and considering all of the 8 possible starting points. Each row of the table presents the obtained accuracies for the n^{th} subgrid of the full grid divided by N, and divided by T the number of profiles of each evolutionary track, starting with profile t. The values in bold of each column represent the maximum (positive and negative) deviations for each simulated star.

7.7 Results for the Subgrids with 1/16 of the Number of Models

(n, N, t, T)	Brie	Cheddar	Feta	Manchego	Parmesan	Stilton
$(3, 4, 1, 16)$	0.0076	−0.0275	−0.0088	−0.0498	0.0271	−0.0037
$(3, 4, 2, 16)$	0.0058	**−0.0286**	−0.0085	−0.0497	0.0254	**-0.0045**
$(3, 4, 3, 16)$	0.0065	−0.0279	−0.0086	−0.0497	**0.0251**	**0.0728**
$(3, 4, 4, 16)$	0.0069	−0.0278	−0.0078	−0.0499	0.0257	0.0715
$(3, 4, 5, 16)$	−0.0156	0.0706	−0.0072	**-0.0967**	0.0269	0.0692
$(3, 4, 6, 16)$	−0.0155	0.0714	0.0485	−0.0963	0.0270	0.0074
$(3, 4, 7, 16)$	−0.0158	**0.0732**	**0.0488**	−0.0183	0.0272	0.0074
$(3, 4, 8, 16)$	**-0.0160**	−0.0043	0.0482	−0.0179	0.0276	0.0069
$(3, 4, 9, 16)$	−0.0048	−0.0048	0.0482	−0.0175	**0.0455**	0.0524
$(3, 4, 10, 16)$	−0.0050	−0.0049	**0.0488**	**-0.0174**	0.0444	0.0513
$(3, 4, 11, 16)$	−0.0055	−0.0035	**0.0488**	−0.0178	0.0441	0.0528
$(3, 4, 12, 16)$	−0.0053	−0.0031	0.0471	−0.0395	0.0443	0.0532
$(3, 4, 13, 16)$	−0.0051	0.0632	−0.0477	−0.0402	0.0446	0.0711
$(3, 4, 14, 16)$	−0.0059	0.0634	−0.0460	−0.0582	0.0452	−0.0037
$(3, 4, 15, 16)$	**0.0081**	0.0616	**-0.0481**	−0.0497	0.0278	−0.0037

Table 7.19: Relative deviations in mass obtained for each one of the 6 simulated stars, for $\ell = 0$, for the 3^{rd} quarter with the number of profiles divided by 16, and considering all of the 16 possible starting points. Each row of the table presents the obtained accuracies for the n^{th} subgrid of the full grid divided by N, and divided by T the number of profiles of each evolutionary track, starting with profile t. The values in bold of each column represent the maximum (positive and negative) deviations for each simulated star.

(n, N, t, T)	Brie	Cheddar	Feta	Manchego	Parmesan	Stilton
$(3, 4, 1, 16)$	**0.0003**	-0.0091	-0.0037	-0.0172	0.0119	-0.0028
$(3, 4, 2, 16)$	-0.0000	-0.0104	-0.0040	-0.0177	0.0105	-0.0039
$(3, 4, 3, 16)$	-0.0004	**-0.0111**	-0.0045	-0.0181	0.0097	**0.0222**
$(3, 4, 4, 16)$	-0.0004	**-0.0111**	-0.0042	-0.0182	0.0100	0.0218
$(3, 4, 5, 16)$	-0.0070	**0.0211**	-0.0050	**-0.0367**	0.0089	0.0195
$(3, 4, 6, 16)$	-0.0073	0.0207	**0.0128**	-0.0371	0.0083	-0.0033
$(3, 4, 7, 16)$	-0.0078	0.0207	0.0127	**-0.0091**	0.0077	-0.0040
$(3, 4, 8, 16)$	**-0.0082**	-0.0072	0.0123	-0.0094	0.0071	-0.0051
$(3, 4, 9, 16)$	-0.0046	-0.0081	0.0117	-0.0096	**0.0125**	0.0109
$(3, 4, 10, 16)$	-0.0049	-0.0091	0.0114	-0.0102	0.0114	0.0098
$(3, 4, 11, 16)$	-0.0055	-0.0095	0.0117	-0.0108	0.0107	0.0096
$(3, 4, 12, 16)$	-0.0058	-0.0101	0.0102	-0.0198	0.0102	0.0090
$(3, 4, 13, 16)$	-0.0060	0.0134	-0.0291	-0.0203	0.0097	0.0146
$(3, 4, 14, 16)$	-0.0067	0.0127	-0.0292	-0.0264	0.0092	-0.0141
$(3, 4, 15, 16)$	-0.0043	0.0115	**-0.0312**	-0.0237	**0.0019**	**-0.0149**

Table 7.20: Relative deviations in radius obtained for each one of the 6 simulated stars, for $\ell = 0$, for the 3^{rd} quarter with the number of profiles divided by 16, and considering all of the 16 possible starting points. Each row of the table presents the obtained accuracies for the n^{th} subgrid of the full grid divided by N, and divided by T the number of profiles of each evolutionary track, starting with profile t. The values in bold of each column represent the maximum (positive and negative) deviations for each simulated star.

(n, N, t, T)	Brie	Cheddar	Feta	Manchego	Parmesan	Stilton
$(3, 4, 1, 16)$	0.0058	**-0.0012**	**0.0018**	**0.0001**	**-0.0096**	0.0038
$(3, 4, 2, 16)$	0.0050	0.0016	0.0031	0.0015	−0.0071	0.0063
$(3, 4, 3, 16)$	0.0067	0.0046	0.0046	0.0029	−0.0051	**0.0034**
$(3, 4, 4, 16)$	0.0071	0.0045	0.0044	0.0029	−0.0054	**0.0034**
$(3, 4, 5, 16)$	**0.0044**	0.0049	0.0074	0.0095	−0.0011	0.0079
$(3, 4, 6, 16)$	0.0055	0.0068	0.0088	0.0111	0.0010	0.0162
$(3, 4, 7, 16)$	0.0066	0.0086	0.0096	0.0081	0.0030	0.0183
$(3, 4, 8, 16)$	0.0077	0.0169	0.0101	0.0093	0.0052	0.0212
$(3, 4, 9, 16)$	0.0079	0.0191	0.0116	0.0103	0.0065	0.0178
$(3, 4, 10, 16)$	0.0090	0.0220	0.0132	0.0124	0.0086	0.0199
$(3, 4, 11, 16)$	0.0101	0.0247	0.0124	0.0137	0.0103	0.0219
$(3, 4, 12, 16)$	0.0111	**0.0270**	0.0153	0.0189	0.0122	0.0242
$(3, 4, 13, 16)$	0.0122	0.0209	0.0400	0.0196	0.0140	0.0243
$(3, 4, 14, 16)$	0.0133	0.0230	0.0424	0.0195	0.0159	0.0386
$(3, 4, 15, 16)$	**0.0201**	0.0252	**0.0465**	**0.0201**	**0.0210**	**0.0410**

Table 7.21: Relative deviations in density obtained for each one of the 6 simulated stars, for $\ell = 0$, for the 3$^{\text{rd}}$ quarter with the number of profiles divided by 16, and considering all of the 16 possible starting points. Each row of the table presents the obtained accuracies for the n^{th} subgrid of the full grid divided by N, and divided by T the number of profiles of each evolutionary track, starting with profile t. The values in bold of each column represent the maximum (positive and negative) deviations for each simulated star.

(n, N, t, T)	Brie	Cheddar	Feta	Manchego	Parmesan	Stilton
$(3, 4, 1, 16)$	-0.0545	0.0739	0.0201	0.1920	**-0.0582**	0.1306
$(3, 4, 2, 16)$	-0.0475	**0.0769**	0.0196	0.1916	-0.0547	0.1330
$(3, 4, 3, 16)$	-0.0511	0.0762	0.0205	0.1919	-0.0537	-0.0147
$(3, 4, 4, 16)$	-0.0526	0.0751	0.0188	0.1928	-0.0551	-0.0137
$(3, 4, 5, 16)$	0.0188	-0.0876	0.0193	**0.2902**	-0.0569	-0.0080
$(3, 4, 6, 16)$	0.0182	-0.0889	-0.0741	0.2893	-0.0566	0.1088
$(3, 4, 7, 16)$	0.0192	**-0.0905**	-0.0745	0.0743	-0.0568	0.1096
$(3, 4, 8, 16)$	**0.0197**	0.0356	-0.0735	0.0740	-0.0569	0.1104
$(3, 4, 9, 16)$	0.0015	0.0365	-0.0734	**0.0730**	**-0.0775**	0.0194
$(3, 4, 10, 16)$	0.0016	0.0370	**-0.0747**	0.0763	-0.0755	0.0215
$(3, 4, 11, 16)$	0.0022	0.0350	-0.0733	0.0773	-0.0751	0.0194
$(3, 4, 12, 16)$	0.0023	0.0351	-0.0708	0.1319	-0.0751	0.0188
$(3, 4, 13, 16)$	0.0019	-0.0733	0.1122	0.1346	-0.0751	**-0.0048**
$(3, 4, 14, 16)$	0.0034	-0.0733	0.1094	0.2029	-0.0752	0.1346
$(3, 4, 15, 16)$	**-0.0584**	-0.0702	**0.1153**	0.1918	-0.0546	**0.1354**

Table 7.22: Relative deviations in stellar age obtained for each one of the 6 simulated stars, for $\ell = 0$, for the 3$^{\text{rd}}$ quarter with the number of profiles divided by 16, and considering all of the 16 possible starting points. Each row of the table presents the obtained accuracies for the n^{th} subgrid of the full grid divided by N, and divided by T the number of profiles of each evolutionary track, starting with profile t. The values in bold of each column represent the maximum (positive and negative) deviations for each simulated star.